Localization of ultrasonic waves in an open three- dimensional system

by

Hefei Hu

A Thesis submitted to the Faculty of Graduate Studies of

The University of Manitoba

in partial fulfilment of the requirements of the degree of

MASTER OF SCIENCE

Department of Physics and Astronomy

University of Manitoba

Winnipeg, Manitoba

THE UNIVERSITY OF MANITOBA

FACULTY OF GRADUATE STUDIES

*****

COPYRIGHT PERMISSION

Localization of Ultrasonic Waves in an Open Three Dimensional System

BY

Hefei Hu

A Thesis/Practicum submitted to the Faculty of Graduate Studies of The University of Manitoba in partial fulfillment of the requirement of the degree

Of

Master of Science

To Mom and Dad.

Acknowledgments

My deepest respect and appreciation to my advisor, Dr. John Page, whose profound insight, patient guidance and financial support made it possible for me to begin my graduate projects and finish this thesis.

I wish to express my deep gratitude to Gilles Roy and other technicians, whose technical supports allowed the experiments to be carried out efficiently.

I am grateful for the helpful discussion with my colleagues in the Ultrasonics Research Laboratory.

I want to thank the Department of Physics and Astronomy at the University of Manitoba for their general support during my graduate studies.

I would also thank Dr. Canming Hu and Dr. Derek Oliver for taking time out from their busy schedules to serve as my oral examiners.

I would like to thank all my friends in Winnipeg. Without them my life would have been much less colourful.

Finally, I am forever indebted to my parents for their *love*.

Hefei Hu

Winnipeg, Manitoba

September 1, 2006

Abstract

The transport of ultrasound through a strongly scattering medium, with either a random or ordered mesostructure, was studied in the intermediate frequency regime, where the wavelength in the sample is comparable to the size of the scatterers. The samples were made by braising aluminum beads to form a solid network, held together by weak bonds between the beads. In the random samples, wave transport was found to be diffusive in the lower part of the intermediate frequency regime (~ 0.25 MHz). At higher frequencies (~2 MHz), the diffusion approximation was found to break down, and the localization of ultrasound was observed. This demonstration of ultrasonic wave localization, believed to be the first experimental realization of this effect in three dimensions, was based on two approaches: the observation of time dependence in the diffusion coefficient, and evidence for non-Rayleigh statistics and anomalously large variance of the normalized transmitted intensity. Band gaps were observed in both the random and crystalline aluminum bead samples, and in the crystals, the group velocity was found to be negative in the lowest frequency gap.

Table of Contents

List of figures

List of tables

Chapter 1 Introduction

1.1 History and background

The phenomenon of Anderson localization, explaining metal-insulator transitions in terms of the possibility of electron localization in disordered systems, was first predicted by Anderson in 1958. Electron localization was later realized to be a general wave phenomenon [Ioffe and Regel, 1960; John, 1984], suggesting that classical waves could also be localized in a random medium. The analogy with electron localization and the advantage of classical waves, which do not suffer from complications arising from interactions like the Coulomb interaction between electrons, have attracted great interest in searching for experimental evidence that classical waves can indeed be localized in three dimensional systems.

Classical wave localization in random media has been investigated, theoretically and experimentally, for the past several decades [Sheng, 1995]. Many theoretical principles and methods, such as Ioffe-Regel criterion [Ioffe and Regel, 1960], the Thouless criterion [Thouless, 1974], scaling theory [Abrahams *et al.*, 1979], self-consistent theory [Vollhardt and Wölfle, 1992; Götze, 1979; Vollhardt and Wölfle, 1980, 1982], random matrix theory [Kogan and Kalveh, 1995], etc., have been developed, and greatly enhanced basic understanding of the phenomenon. In parallel, many samples and experiments have been designed and made, but it has been extremely difficult to achieve

sufficiently strong scattering to realize localization in practice. Even in very favourable circumstances, it was found that absorption in the samples suppressed the localization, so that it was difficult to tell whether the observation of signatures of localization in the transmission [Weirsma *et al.*, 1997] were in fact due to localization or just absorption [Scheffold *et al.*, 1999; Weirsma *et al.*, 1999].

For the past 10 years, a statistical approach to photon localization has been developed [Nieuwenhuizen and van Rossum, 1994; Kogan and Kalveh, 1995; Markoš and Soukoulis, 2005]. Due to the breakdown of diffusion in disordered media, the intensity of the transmitted waves fluctuates greatly from one position to another on the surface of the sample, leading to a large variance of the transmitted intensity. These fluctuations may greatly exceed the more usual variations of intensity in random media associated with speckles, which in the diffusive regime obey an exponential distribution of intensities known as the Rayleigh distribution [Goodman, 1985]. As the localized regime is approached, the probability of find very intense speckles is enhanced, leading to a non-Rayleigh distribution described by a stretched exponential at large intensities [Nieuwenhuizen and van Rossum, 1994; Kogan and Kalveh, 1995]. These predictions have been extensively studied in quasi-one-dimensional systems using microwaves, and good agreement between theory and experiment has been found [Stoytchev and Genack, 1997; Chabanov *et al.*, 2000].

However, up now, most of the successful experiments exhibiting signatures of localization of classical waves have been limited to quasi-one-dimensional systems, and all have focused on photons at optical or microwave frequencies. However, despite some very promising reports [Wiersma *et al.*, 1997; Störzer *et al.*, 2006], there is no consensus that photon localization has been achieved in three dimensions. Furthermore, no experimental observations of the localization of sound have been reported yet, making the observation of ultrasound localization in three dimensional disordered media a big and exciting challenge. The main goal of this thesis is to address this challenge.

While the transport of classical waves in random media continues to attract much attention, the behaviour of classical waves in periodic systems is also a great current interest. These periodically structured media are called photonic or phononic crystals, depending on whether they are designed to diffract light or sound. Photonic band gaps, where the propagation of photons is prohibited, were first predicted and realized experimentally in 1987 [John, 1987; Yablonovitch, 1987]. Phononic band gaps, analogous to photonic band gaps, were then reported theoretically [Economou and Sigalas, 1994; Kushwaha *et al.*, 1994; Sigalas and Economou, 1996; Sanchez-Perez *et al.*, 1998; Montero de Espinosa *et al.*, 1998; Liu *et al*, 2000] and finally realized experimentally in three dimensions only quite recently [Liu, *et al*, 2000; Yang, *et al.*, 2002]. Moreover, an interesting experimental demonstration of ultrasound tunneling through the band gap of a three-dimensional (3D) phononic crystal was reported [Yang *et*

al., 2002]. These phononic crystals were made by periodically arranging monodisperse spherical scatterers in a close-packed lattice. What will happen if these scatterers are connected by weak bonds, instead of just touching each other, so that instead of playing the role of scatterers in a continuous matrix, the spheres form a periodic network through which the waves propagate? Does this tunneling effect still exist? Or will some new striking behaviour appear? A second goal of this thesis is to seek answers to these questions.

1.2 Outline of the thesis

The main purpose of this thesis is to present new experimental results on the observation of sound localization in a three-dimensional disordered material. The thesis is organized into six chapters: Introduction (chapter 1), Theory (chapter 2), Sample preparation (chapter 3), Experiments (chapter 4), Results (chapter 5) and Conclusions (chapter 6).

The main part of thesis begins with a review of theory in chapter 2. Section 2.1 provides an introduction, and a summary of diffusion theory that can be used to describe the propagation of multiply scattered ultrasound is then presented in section 2.2. A description of the relevant localization theories, including time dependence in the diffusion coefficient and the statistical approaches, follows in section 2.3.

Chapter 3 describes the preparation of the samples. Section 3.1 introduces the

principles of braising aluminum beads. The details of making disordered sintered aluminum bead samples are described in section 3.2. Then, the procedure for making sintered aluminum bead crystals is presented in section 3.3.

Next a description of the apparatus and procedure used to perform the experiments is given in chapter 4 (Experiments). Section 4.1 introduces the general ideas of the ultrasound experiments. Then the experimental setup is presented in section 4.2, followed by the apparatus in section 4.3. Section 4.4 discusses the measurement techniques and geometries used in ultrasonic measurements of both ballistic and diffusive propagation. The former describes the coherent propagation of a pulse through a disordered medium, while the latter describes the transport of the ensemble averaged multiply scattered ultrasonic energy density.

The main results are reported in the chapter 5. Section 5.1 outlines the organization of this chapter and describes some parameters of our samples. Section 5.2 discusses the results in the diffusive regime. The ballistic results are first presented, and then the analysis and results of the diffusive data are described. Section 5.3 presents the results in the localized regime. Two main approaches to observe signatures of localization are introduced first. Then the analysis and results showing the time-dependent diffusion coefficient and the intensity statistics are presented successively. Section 5.4 shows the experimental results for the crystal samples, and a comparison between our crystals and

more traditional phononic crystals is made.

The conclusions that may be drawn from this research are presented chapter 6, where the main findings are summarized. Additional experimental results that further reinforce the main conclusions of the thesis are presented in the two appendices.

Chapter 2 Theory

2.1 Introduction

The theory needed to interpret the experimental results is outlined in this chapter. The next section deals with the diffusive regime, where phase information in the multiply scattered waves is ignored and the transport of the ultrasonic energy density through a strongly scattering medium is approximated as a random walk. The basic assumptions of the model are introduced, and the solutions of the diffusion equation for pulse propagation through a random medium with reflecting boundaries are summarized. One of the important results of the diffusion approximation is that the transmitted intensity is predicted to decay exponentially at long propagation times.

In the localized regime, the diffusion approximation breaks down because wave interference effects become important due to the enhanced probability of the scattered waves returning to the same point. Recent theoretical predictions, that the transmitted intensity at long times obeys a power law, and that the diffusion coefficient decreases as $1/t$, are presented. Finally, the main theoretical results for the statistics of the transmitted intensity in the localization regime are summarized. These predictions of non-Rayleigh statistics and very large variance of the normalized transmitted intensity provide another approach to demonstrate the localization of classical waves.

2.2 Diffusive propagation

The propagation of waves through a multiply scattering medium may be approximated as a random walk, and thus can be described as a diffusive process. The multiply scattered energy density U satisfies the diffusion equation,

$$\frac{\partial U(\vec{r},t)}{\partial t} - D\nabla^2 U(\vec{r},t) = \delta(\vec{r}-\vec{r_o})\delta(t) \qquad (2\text{-}1)$$

where $\delta(\vec{r}-\vec{r_o})$ is a point source located at $\vec{r_o}$, and D is the diffusion coefficient, which is normally given by the Boltzman diffusion coefficient $D_B = \frac{1}{3} v_e l^*$. Here, v_e, the energy velocity, is the velocity at which acoustic energy is transported through the medium, and l^*, the transport mean free path, is distance at which the direction of propagation becomes randomized. It is also assumed that diffusion begins from a depth $z_o = l^*$ inside the sample [Page *et al.*, 1995, Schriemer *et al.*, 1997].

The solutions to equation (2-1) depend on boundary conditions, and are discussed in detail by Carslaw and Jaeger [Carslaw and Jaeger, 1959]. When a short pulse is incident on a slab-shaped sample, the diffuse energy density on the opposite side of the sample is described by [Page *et al.*, 1995]

$$U(x,y,z) = \frac{e^{-r^2/4Dt} e^{-t/\tau_a}}{2\pi DLt} \sum_{n=1}^{\infty} C_n(z) e^{-D\beta_n^2 t/L^2}, \qquad (2\text{-}2)$$

with $r^2 = (x-x_0)^2 + (y-y_0)^2$ being the transverse distance from the source position, and L the sample thickness. The coefficient $C_n(z)$ are given by

$$C_n(z) = \frac{[\beta_n K \cos(\beta_n z/L) + \sin(\beta_n z/L)][\beta_n K \cos(\beta_n z_0/L) + \sin(\beta_n z_0/L)]}{\beta_n^2 K^2 + 1 + 2K}$$

The values of β_n are given by the positive zeros of the transcendental equation

$$\tan\beta = \frac{2\beta K}{\beta^2 K^2 - 1} \tag{2-3}$$

and the dimensionless constant K is given by

$$K = h/L \tag{2-4}$$

Here h is the extrapolation length and is defined as

$$h \equiv \frac{2l^*}{3}\frac{1+R}{1-R} \tag{2-5}$$

R is the angle-averaged reflection coefficient, defined by the ratio of the incoming flux to the outgoing flux at the boundaries [Zhu *et al.*, 1991].

The experiment measures the transmitted flux normal to the slab, which is related to the energy density by Fick's law:

$$J(t) = -D_B \frac{\partial U}{\partial z} \tag{2-6}$$

Hence, the transmitted flux for a point source is described by

$$J(t) = \frac{e^{-r^2/4D_B t} e^{-t/\tau_a}}{2L^2 t} \sum_{n=1}^{\infty} A_n e^{-D_B \beta_n^2 t/L^2} \tag{2-7}$$

with

$$A_n = \frac{\beta_n \left[\beta_n K \sin\beta_n - \cos\beta_n\right][\beta_n K \cos(\beta_n z_0/L) + \sin(\beta_n z_0/L)]}{\beta_n^2 K^2 + 1 + 2K} \tag{2-8}$$

where τ_a is the absorption time.

The transmitted flux for a plane wave source is calculated by integrating over all source points (x_0, y_0) in the plane $z = z_0$ and is given by

$$J(t) = \frac{2D_B e^{-t/\tau_a}}{L^2} \sum_{n=1}^{\infty} A_n e^{-D_B \beta_n^2 t / L^2} \tag{2-9}$$

In the experiments, the real source is not a delta function in time, but a function with finite width. Hence, it is also important to convolve the transmitted flux with the finite width of the input pulse $J_{in}(t)$:

$$J_{trans}(t) = \int_{t_1}^{t_2} J_{in}(t')\, J_{delta}(t - t')\, dt' \tag{2-10}$$

where t_2-t_1 is the width of the incident pulse.

2.3 Localization

2.3.1 Introduction

Anderson localization of electrons, due to the breakdown of diffusion in a disordered material, was first predicted by Anderson in 1958 [Anderson, 1958]. The central idea was that electrons become localized when the disorder in the electron energy from lattice site to site exceeds the coupling between sites, so that the wave functions fall exponentially in space and transport ceases in an infinitely large sample. In a finite sample, current can still flow, but the transport of electrons decays exponentially with sample thickness, and the diffusion coefficient tends to zero as the thickness increases.

In the past two decades, the analogy with electron localization has greatly raised interest in the possibility of observing the localization of classical waves in random media. One of the conditions that has been proposed for wave localization to occur is the Ioffe-Regel criterion [Ioffe and Regel, 1960], which states that wave propagation ceases when $kl < 1$, where k is the wave vector and l is the mean free path. However, it is still not entirely clear whether the mean free path in this expression should be the transport mean free path l^*, as is often assumed, or the scattering mean free path l_s [van Tiggelen, 1999]. Also, it has been pointed out that the Ioffe-Regel criterion is not very useful for predicting the localization of acoustic or elastic waves, since kl is expected to decrease very gradually as the localization regime is approached, without any sharp transition [Sheng *et al.*, 1994] and it has been found experimentally that $kl_s < 1$ does not necessarily imply localization for ultrasonic waves [Page *et al.*, 2004]. A better way to observe the localization of classical waves is to measure the transmission coefficient as a function of of sample thickness L. In contrast to the diffusive regime, where the transmission coefficient $T(L)$ decreases linearly with sample thickness, $T(L)$ is predicted to pass through a transition region of $1/L^2$ behaviour to an exponential decay in the localized regime [Anderson, 1958; Abrahams *et al.*, 1979]. Such behaviour has been seen experimentally by Weirsma *et al.* (1997) in infrared transmission through a wedge of GaAs particles. However, if absorption is present, it becomes difficult to distinguish between exponential decay due to absorption and exponential decay due to localization [Scheffold *et al.*, 1999; Weirsma *et al.*, 1999].

Recently, two new approaches have been proposed to observe the localization of classical waves that largely circumvent the complications due to absorption. One is the observation of time-dependence in the diffusion coefficient [Chabanov *et al.*, 2003; Skipetrov and van Tiggelen, 2004, Cheung *et al.*, 2004, Skipetrov and van Tiggelen, 2006, Störzer *et al.*, 2006], and the other one is the statistical approach [Stoytchev and Genack, 1997; Chabanov *et al.*, 2000]. In the localization regime, the diffusion coefficient decays as $1/t$ instead of being a constant. Furthermore, the variance of the normalized transmitted intensity becomes much bigger, and the intensity distribution obeys a stretched exponential decay instead of the Rayleigh distribution. A description of these two approaches will be presented in the following two sections.

2.3.2 Time-dependent diffusion coefficient

If the diffusion coefficient is time-dependent, the product $D_B t$ should be replaced by integral $\int_0^t D(t')dt'$ in equation (2-9) [Crank, 1956]. Hence, the transmission would decay as

$$I(t) \sim \sum_{n=1}^{\infty} A_n e^{-\frac{\beta_n^2}{L^2}\int_0^t D(t')dt'} e^{-t/\tau_a} \tag{2-11}$$

When l^*/L and R are small, the equation (2-11) can be approximated at long times by

$$I(t) \sim e^{-\frac{\pi^2}{(L+2z_e)}\int_0^t D(t')dt'} e^{-t/\tau_a} \tag{2-12}$$

Hence, the expression for $D(t)$ is

$$D(t) \equiv -\left[(L+2z_0)^2/\pi^2\right]\left[\frac{d}{dt}(\ln I(t)) + \frac{1}{\tau_a}\right] \qquad (2\text{-}13)$$

The dynamics of Anderson localization in open three dimensional (3D) media was investigated recently [Skipetrov and van Tiggelen, 2006] using the self-consistent theory of localization. It is assumed that a 3D disordered slab is confined between the planes $z = 0$ and $z = L >> l$. While Skipetrov and van Tiggelen did not explicitly take absorption into account, this can be achieved by multiplying the transmitted intensity by $\exp(-t/\tau_a)$.

In the diffuse regime, $kl >> 1$, and if $t >> t_D$ is assumed, where $t_D = (L+2z_0)^2/\pi^2 D_B$, which is the typical time needed to cross the disordered sample by diffusion, Skipetrov and van Tiggelen showed that the diffusion coefficient can be expressed as

$$\frac{D(t)}{D_B} \cong 1 - \frac{1}{(kl)^2}\left[1 + \frac{3}{2}\frac{l}{L}(7.25) - 4\ln\frac{L}{l}\right] - \frac{1}{(kl)^2}\frac{3}{2}\frac{l}{L}\left[\ln\frac{t}{t_D} - \frac{2.25}{t/t_D}\right] \qquad (2\text{-}12)$$

We see that the reduction in $D(t)$ below D_B contains two terms: a static term, which is of order $(1/kl)^2$, and a dynamic term, which is reduced by an additional factor of l/L smaller. This implies that non-exponential transmission is very difficult to observe in this diffuse regime.

In the localization regime, $kl < 1$, the transmitted intensity after time t_D is predicted to obey a power law: $I(t) \sim t^{-(1+s)}$ with $s \sim 0.85$, which is very different to exponential decay

in the diffusion regime. For very long times $t > 1/\alpha^*$, where $\alpha^* = (D_B / \xi^2)\exp(-L/\xi)$ with $\xi = 6l_s(kl_s)^2/[1-(kl_s)^4]$ being the localization length, $I(t) \sim \exp(-\alpha^* t)/t^{p+1}$ $(p \sim 0.5)$. Hence, the time-dependent diffusion coefficient is predicted to have the following behavior:

$$\frac{D(t)}{D_B} \approx (s+1)t_D/t, \qquad t_D << t < 1/\alpha^*$$

$$\approx \alpha^* t_D + (p+1)t_D/t, \qquad t > 1/\alpha^* \tag{2-13}$$

We can see that there is a window of time over which the time-dependent diffusion coefficient decays as $1/t$ in localization regime.

2.3.3 Statistical approach to localization

Because of the random structure of the samples, it is virtually impossible to predict exactly the intensity variations in the near-field pattern. Therefore, it is both necessary and more useful to discuss the statistical properties of speckle patterns. The intensity distribution properly reflects the macroscopic properties, although the microscopic properties are not possible to determine. When the intensity is normalized to its average value, its distribution is universal, independent of the dimensionality of the system.

In the diffuse regime, the intensity distribution obeys the Rayleigh distribution [Goodman, 1985], which is a negative exponential:

$$P(s_{ab} = I_{ab} / < I_{ab} >) = \exp(-s_{ab}) \tag{2-14}$$

where $<I_{ab}>$ is the average intensity. I_{ab} means the intensity from an incoming mode a and outgoing mode b. Hence, the total intensity for incoming mode a is $I_a = \Sigma_b I_{ab}$ and the corresponding normalized quantity is $s_a = I_a/<I_a>$. In contrast to the diffuse regime, in the localized regime, the intensity distribution is non-exponential, and is predicted to have the form of a stretched exponential for large s_{ab} [Nieuwenhuizen and van Rossum, 1995; Kogan and Kalveh, 1995; van Rossum and Nieuwenhuizen, 1999]:

$$P(s_{ab}) \sim \exp(-2\sqrt{g' s_{ab}}) . \tag{2-15}$$

The parameter g' was defined by Genack as a localization parameter [Chabanov *et al.*, 2000], which is also related to variance of s_a:

$$g' \equiv 2/[3\,\mathrm{var}(s_a)] \tag{2-16}$$

In the absence of absorption g' is equal to the dimensionless conductance, g, making a connection with theory of localization of electrons. Genack conjectures that localization is achieved for $g' \leq 1$ whether absorption is present or not. Kogan *et al.* (1995), used the isotropic approximation, which assumes the perfect mode mixing that is only valid for quasi-one dimensional systems, to relate distribution of s_a to that of s_{ab}:

$$2\mathrm{var}(s_a) = \mathrm{var}(s_{ab})\text{-}1 \tag{2-17}$$

Corresponding to the localization criterion $g' \leq 1$, localization is obtained in quasi-one dimensional systems when

$$\mathrm{var}(s_{ab}) \geq 7/3 \tag{2-18}$$

Chapter 3 Sample preparation

3.1 Random sintered aluminum sample preparation

3.1.1 Introduction

To search for the localization of sound in a random three dimensional structure, sintered aluminum-bead samples were fabricated. The aluminum beads, coated with silicon and Nocolok power, were brazed at around 650 degrees Celsius in a furnace. The general instructions for making such samples can be found in two references (Baldantoni *et al.*, 2000; Bobowski, 2001) listed in the reference section. In this section, the detailed procedure that I followed is summarized.

The type of aluminum beads we used was Aluminum M362-1100-ALO-TEMP from ABBOTTBALL Company. The diameter of aluminum beads was 0.162 inch (4.11 mm). Before starting the preparation, the following ingredients and tools were assembled:

- NOCOLOK powder, Silicon particle
- Stainless steel molds
- Various beakers and mixing tools like Teflon rods
- NaOH
- Hair dryer
- Reverse Osmosis water

3.1.2 Principle

The basic principle for fabricating the samples is as follows. Aluminum beads are first coated with a mixture of NOCOLOK powder and silicon particles. Above $562^{\circ}C$, NOCOLOK powder starts melting, which dissolves the oxide on both aluminum beads and silicon particles. Aluminum beads are now in contact with silicon particles, and the absence of oxide layers allows solid state interdiffusion of aluminum and silicon. Very quickly the composition near a silicon particle reaches that of the Al-Si eutectic (12% Si); as the temperature increases beyond the eutectic reaction temperature ($577^{\circ}C$), a liquid near eutectic composition is formed. Formation of the liquid leads to rapid dissolution of the remaining silicon through liquid diffusion. The pool of liquid continues to grow, consuming aluminum, until all of the silicon is consumed in the melt. The liquid layer solidifies on cooling to room temperature and the joints of eutectic Al/Si alloy are formed, connecting individual aluminum beads.

3.1.3 Procedure

(1) My recipe

For every **100g** Aluminum beads, **0.4g** Silicon and **2g** NOCOLOK powder were used. The final weight of samples may be several times heavier than 100g, but it is recommended to coat only 100g of aluminum beads at once due to the limited size of the container. If too many beads were coated at one time, say 200g, the fluctuation in the coating layer thickness of each bead would be much bigger.

Note that the strength and size of the joints between the aluminum beads is only proportional to the amount of silicon powder deposited onto the surface of the Aluminum beads, so that my recipe can be modified as needed to prepare samples with different elastic properties.

(2) Removal of the oxide layer of the aluminum beads

The first step of the procedure was removing the oxide layer of the aluminum beads. Although melting NOCOLOK will consume the oxide layer of aluminum beads, if the oxide layer is too thick, it will not be totally consumed by the limited amount of NOCOLOK deposited on the surface of the beads. To remove the oxide layer, I put aluminum beads into NaOH solution and waited until I saw that hydrogen was produced, which meant the NaOH had started to react with aluminum. Then the aluminum beads were washed by reverse osmosis water.

(3) Coating

0.4g Silicon particle and **2g** NOCOLOK powder were mixed with Reverse Osmosis water into a beaker. The amount of Reverse Osmosis water can vary dramatically, since it will be dried eventually anyway. Then I poured the Aluminum beads into the slurry and stirred them with a Teflon rod. A hair dryer was used to dry the beads when I stirred the beads in the slurry. About half an hour later, after the water had evaporated

completely, there should be a uniform coating formed on the surface of the Aluminum beads. Sometime the coating was not quite uniform. At this point, I usually added some Reverse Osmosis water into the beaker and repeated the drying procedure. Some of the coated beads that I made are presented in figure 3.1.1.

To make a random sample, I just simply poured the coated Aluminum beads into a stainless steel mold with diameter of 120 mm until the beads at the top were 1 or 2 mm higher than the height of the mold. I then carefully pressed the top plate of the mold until it tightly touched the mold, in order to ensure a more uniform packing of the beads and parallelism of the top and bottom surfaces of the samples.

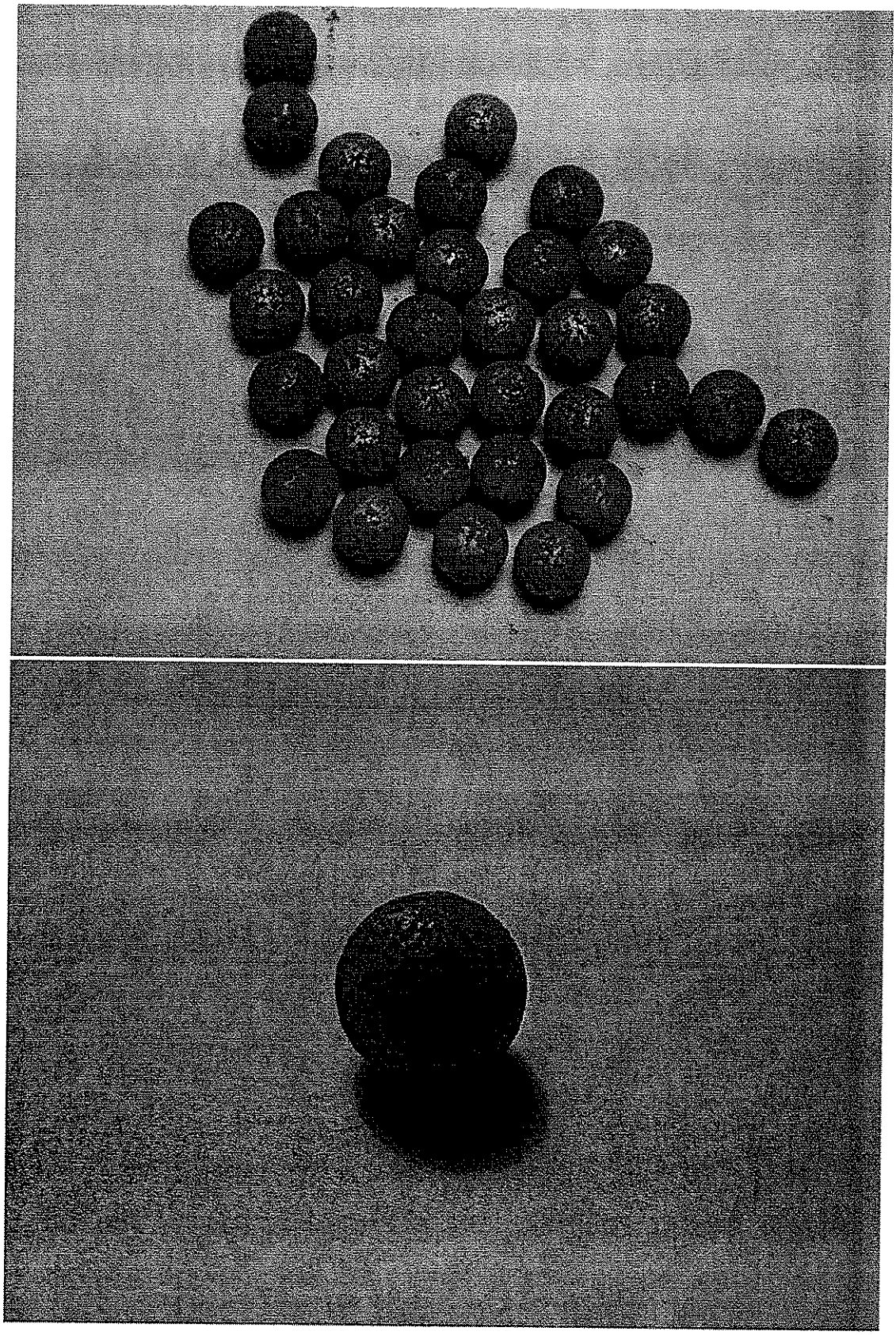

Figure 3. 1. 1 Coated Aluminum beads

(4) Heating

After the Aluminum beads were coated, it was time to heat them up, which was done at $645^{\circ}C$ in a nitrogen atmosphere. The heating apparatus was located in the basement of the Allen Building.

a) Apparatus

We needed a furnace, a pump, Nitrogen gas, a sample box, a few plastic tubes and stainless steel pipes. The apparatus and set-up are shown in figure 3.1.2.

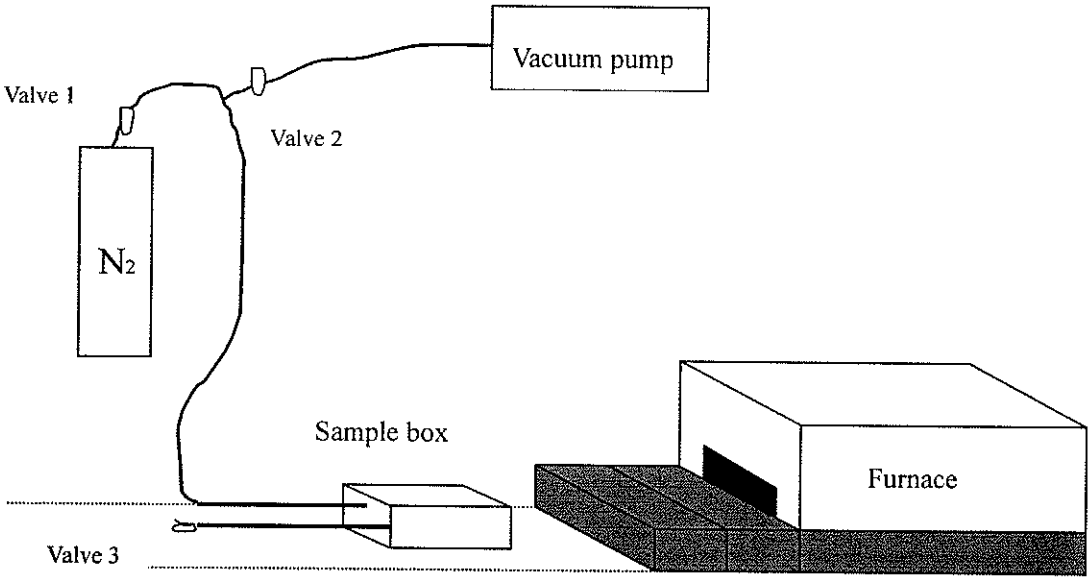

Figure 3. 1. 2 Heating system

b) Heating procedure

- The mold with coated aluminum beads was placed into the sample box which would be placed in the furnace later. The bolts on the cover of the sample box were tightened as much as possible to get good a vacuum seal, having made sure that the copper gasket sat in the proper position on the cover.

- ***Evacuating the sample box***

  After I closed valves 1, 2 and opened valve 3 (figure 3.1.2), the vacuum pump was switched on. If the seal was good enough, the vacuum gauge reached a reading of -29 or lower. To further check the seal of the sample box, I closed valve 2, and waited 5 minutes. For a good seal, the gauge reading should not drop significantly during 5 minutes (gauge reading should be no higher than -28).

- ***Feeding nitrogen gas***

  After the sample box was sealed well, I fed nitrogen gas into the sample box. To do this, I closed valve 2 and opened valve 1. Once the vacuum gauge read 10, I opened exhaust valve 3 and the nitrogen gas flowed out. The nitrogen gas should be run at a pressure of 10 psi and a flow rate of 1.2 on the flow meter. When nitrogen gas was flowing, if the seal of the sample box was not good, the sound of gas leaking was clearly heard. This was another way, which I though was a better way, to test the seal.

➢ ***Recording temperature***

Three thermocouples (K-type) were used to measure the temperature. One was for the temperature in furnace, and the other two were for the front and the back of the sample box, respectively. The three voltages were measured using Hewlett-Packard Digital Voltage Meters (HP DVM) and recorded on a computer using a data acquisition program called Rebecca.

Based on standard thermocouple tables, the relation between temperature in degrees Celsius and voltage in millivolts for temperatures between 0 and 800 degrees Celsius is that:

$$T = 25.8 \times V^{0.98} + RoomTemperature$$

➢ ***Heating***

Before brazing the Aluminum beads, I made sure that the temperature monitored by the thermocouple in the furnace reached 750 degrees and the room temperature was recorded. The temperature of the sample was raised to around 650 °C by gradually inserting the sample box into the furnace. The detailed procedure was as follows:

I located the cover of the sample box a distance equal to the length of 2 bricks (7.3 inch) outside the furnace. When the temperature of the front thermocouple reached 2.9 mV (100 °C), I started to record the time. Then I waited until the front thermocouple reached 9.0 mV (250 °C) and the time was recorded again. The time

interval was about 20 minutes. Then I pushed the sample box 4 inches into the furnace. At this point, the opening of the furnace was covered by ceramic plates. It would take about 5 minutes for the front thermocouple to reached 17 mV ($440^{\circ}C$). Then I placed the sample box another 4 inches deeper and waited approximate 5 minutes until the front thermocouple reached around 21mV ($535^{\circ}C$). Finally, I pushed the sample box as far as it could go and waited for the front thermocouple to read 25.8 mV ($650^{\circ}C$). Meanwhile the back thermocouple should reach at least 23 mV ($585^{\circ}C$), otherwise the back of sample might not braze due to the temperature gradient in the sample box. At this point, I usually kept the reading of the temperature of the front thermocouple around 25.8 mV for 5 minutes by pushing and pulling the sample box to adjust its position inside the furnace.

- ***Cooling***

I pulled the sample box back by a couple of inches and waited 2 minutes. I repeated this procedure until the sample box was totally out of the furnace and then covered the opening of the furnace. I kept recording readings until the front thermocouple read 9.0 mV. At this point, I turned off the nitrogen gas and also stopped Rebecca. An example of the heating profile for a random sample is shown in figure 3.1.3.

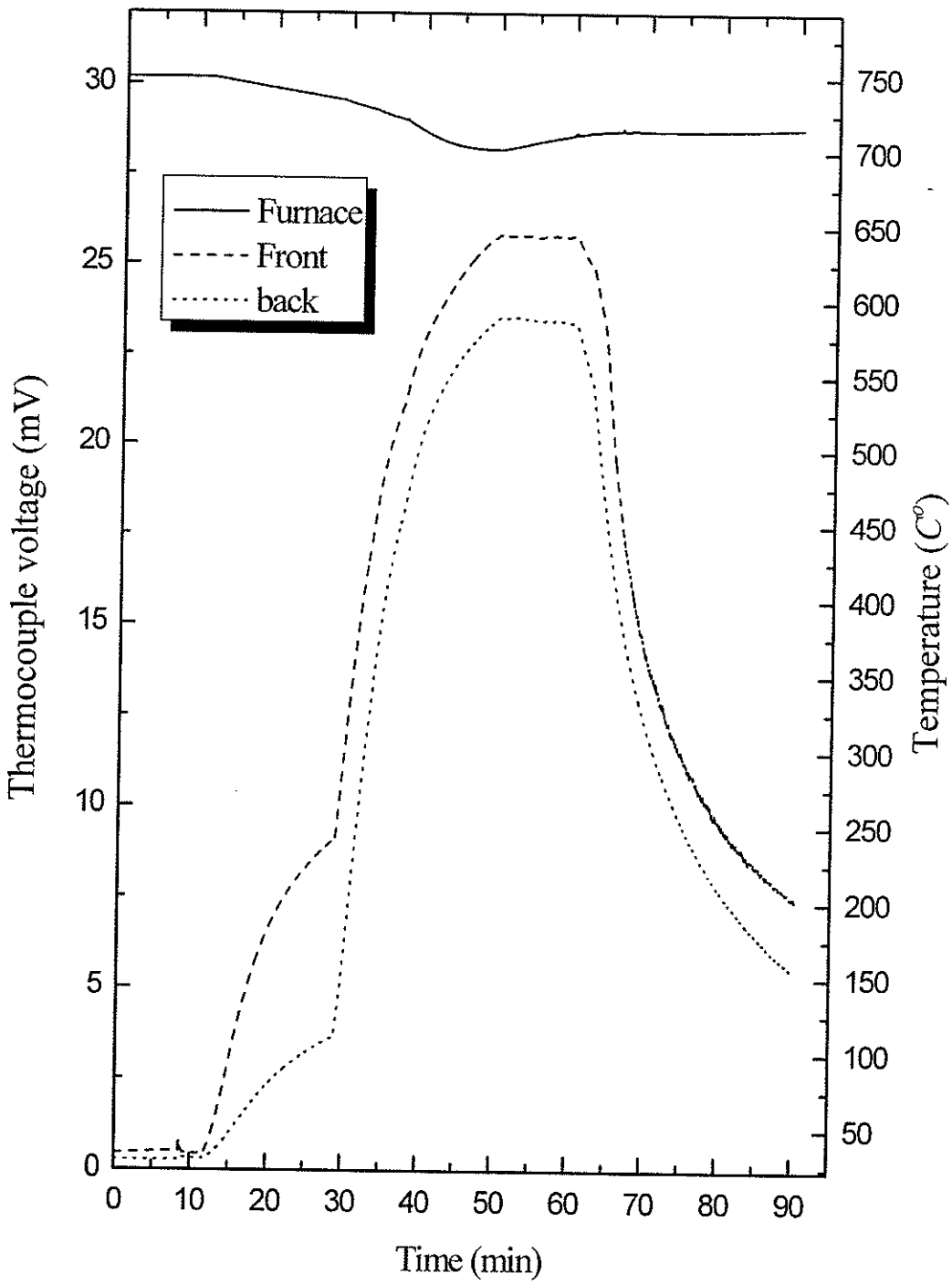

Figure 3. 1. 3 Typical temperature cycle for braising the random samples.

(5) Polishing, cleaning and mounting

The sample was often very dirty after it was taken out of the sample box. One example is shown in figure. 3.1.4 (upper picture). To make a good coupling for waves getting into the sample, I polished the both surfaces of the samples a little bit to make them flat and parallel. After polishing, the samples were immersed in NaOH solution for 10 minutes or so, which made the samples shiny. One example of a cleaned sample is showed in Fig.3.1.3 (lower picture). To mount the samples, I used clear transparencies as two walls and Stycast 1266 epoxy to make permanent coupling between the sample and transparencies, with which the sample was fixed in a plastic holder. Since the experiment was performed in the water tank, the sample had to be sealed well by silicon rubber.

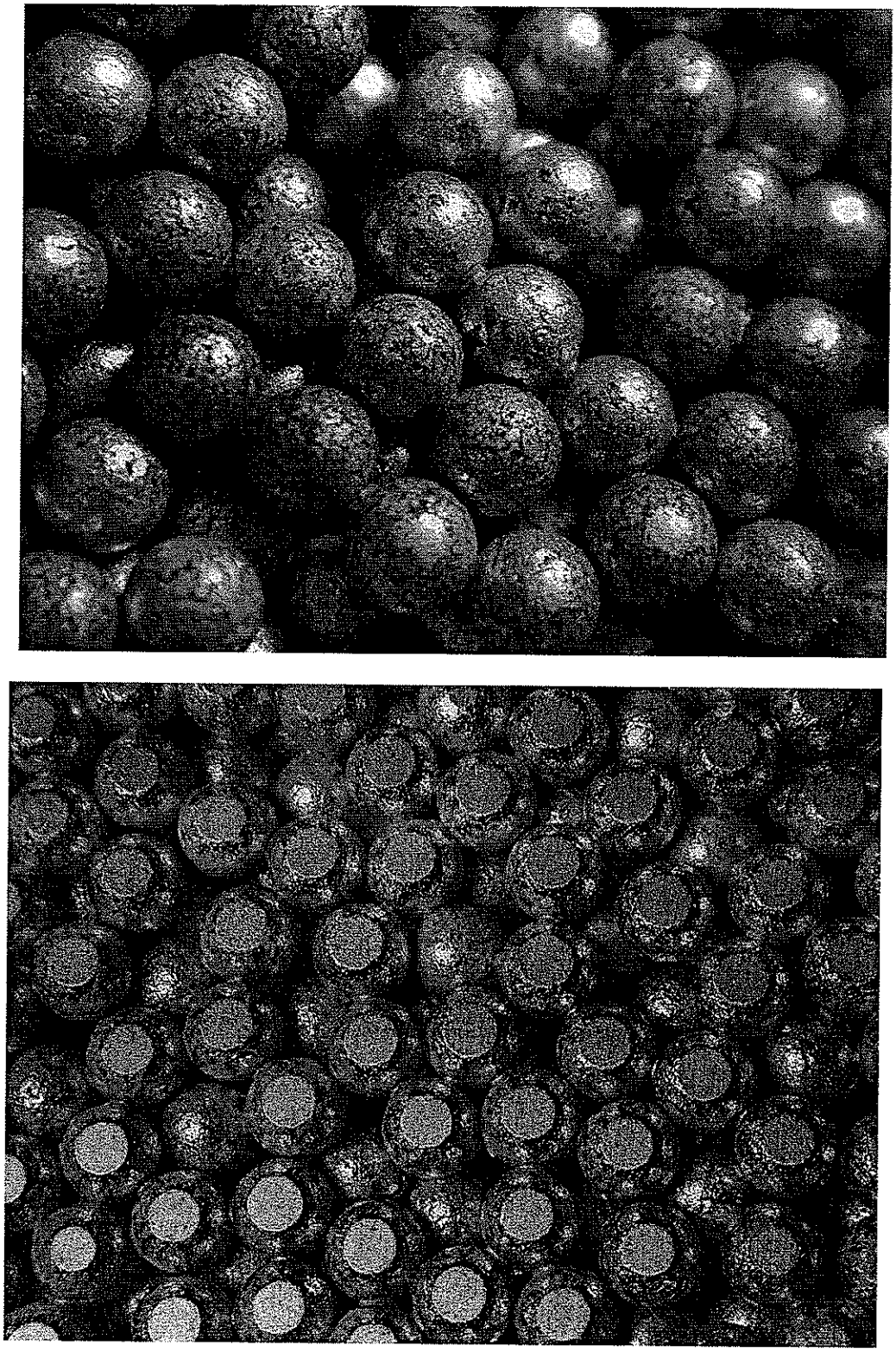

Figure 3. 1. 4 Sintered aluminum samples (upper picture: before being cleaned, lower picture: after being polished and cleaned).

3.2 Sintered aluminum crystal preparation

3.2.1 Crystal template

The aluminum beads were assembled in a face centered cubic (fcc) crystal structure, with the beads packed in triangular layers along the [111] direction. The top view of the stainless steel template, which was used to ensure that the beads could be arranged in this structure, is shown in figure 3.2.1. For a sample with a perfect hexagonal bottom layer having n beads (diameter d) along each side, the formulae for the dimensions of the side length L_A and L_B and the angles of inclination of the side, α and β, are [Yang, 2003]

$$\begin{aligned} L_A &= (n-1+tg\frac{\alpha}{2})d \\ L_B &= (n-1+tg\frac{\beta}{2}ctg75^o)d \\ \tan(\alpha) &= \sqrt{2} \\ \tan(\beta) &= 2\sqrt{2} \end{aligned} \tag{3-1}$$

Our samples were designed with 12 beads on each side of the bottom layer. From equation (3-1), it was calculated that $L_A = 1.8659"$, $L_B = 1.8127"$.

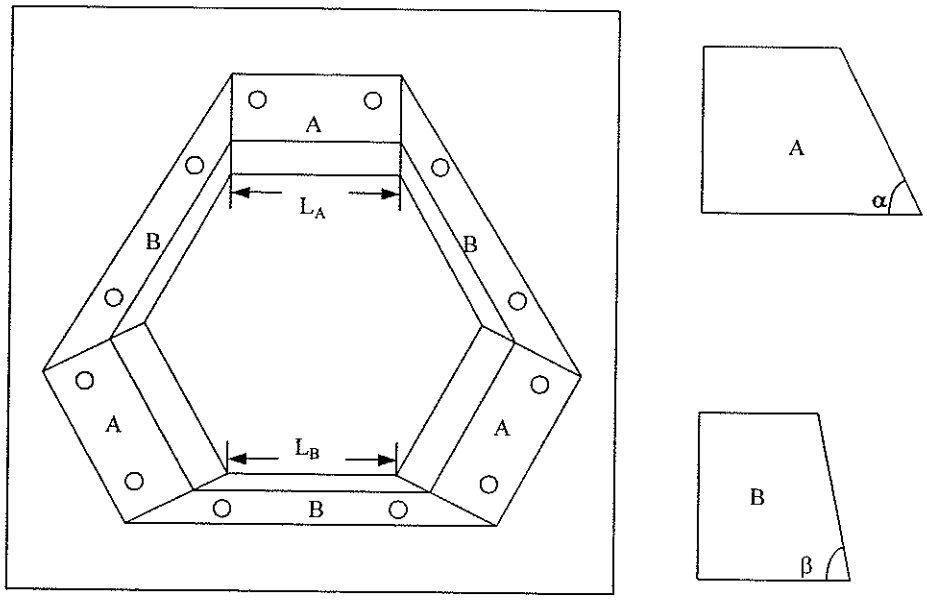

Figure 3. 2. 1 Top view of one of the sample templates and the side view of the blocks A and B [Yang, 2002].

3.2.2 Crystal preparation

There only two differences in the procedure between random and crystal sample preparation. One is that after the aluminum beads were coated, we needed to arrange the coated beads in an fcc structure in the template rather than just pouring the coated beads in the mold. The other difference is that the highest reading of the front thermocouple in the sample box should reach around 26.2 mV. This reading is higher than that for random sample making, since the geometry of the template resulted in an extra distance between the sample and the front of the sample box. One typical heating profile for crystal preparation is showed in figure 3.2.2

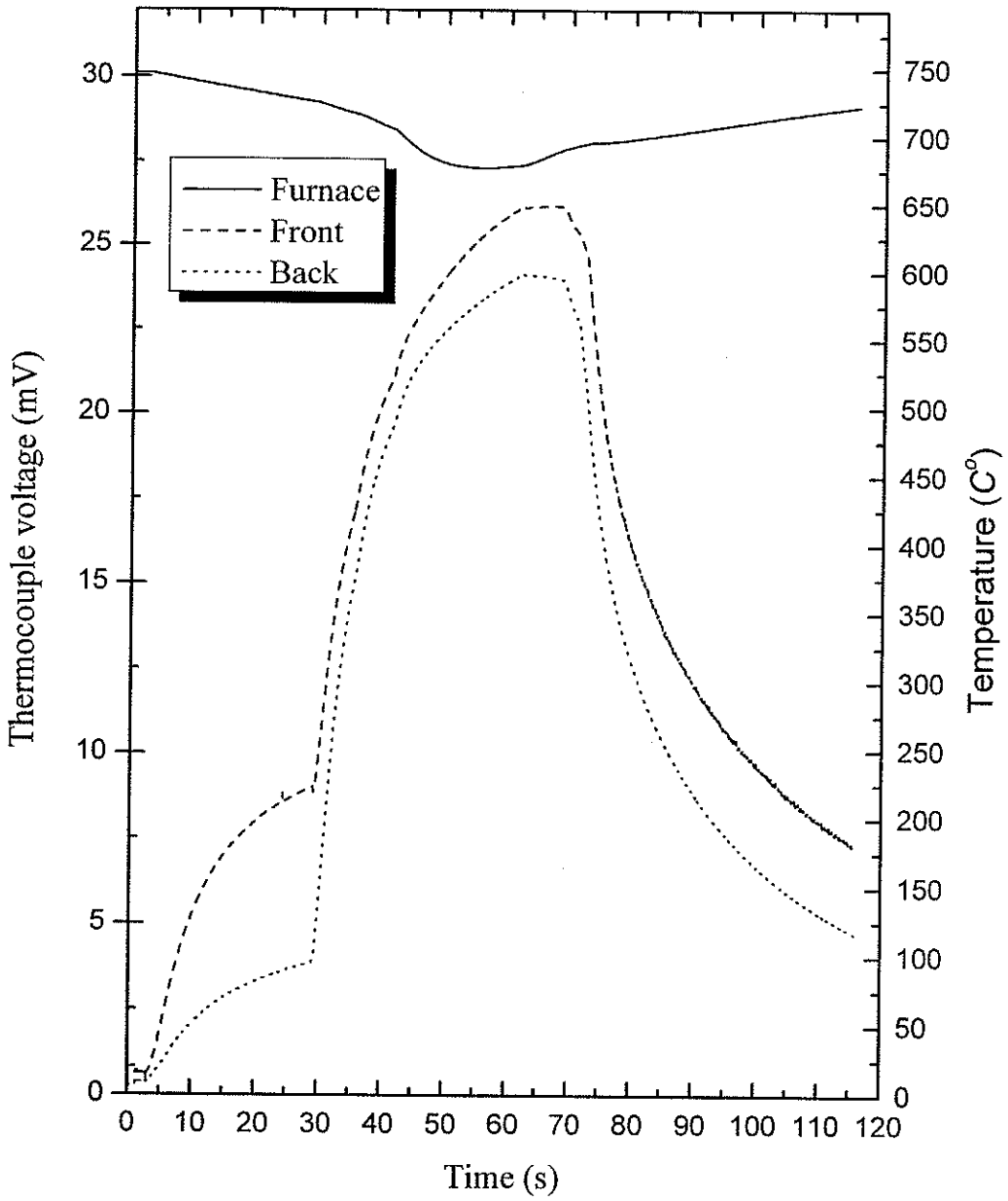

Figure 3. 2. 2 Heating profile for sintered aluminum crystal sample preparation.

Unfortunately, despite the excellent precision with which the beads were positioned on their lattice sites using this technique, I could not make these crystal samples perfectly. Some bonds between beads were missing. Thus, the crystals had near perfect translational order, but non-negligible bond disorder. Some pictures from different view angles of sintered aluminum crystal samples are showed in figure 3.2.3.

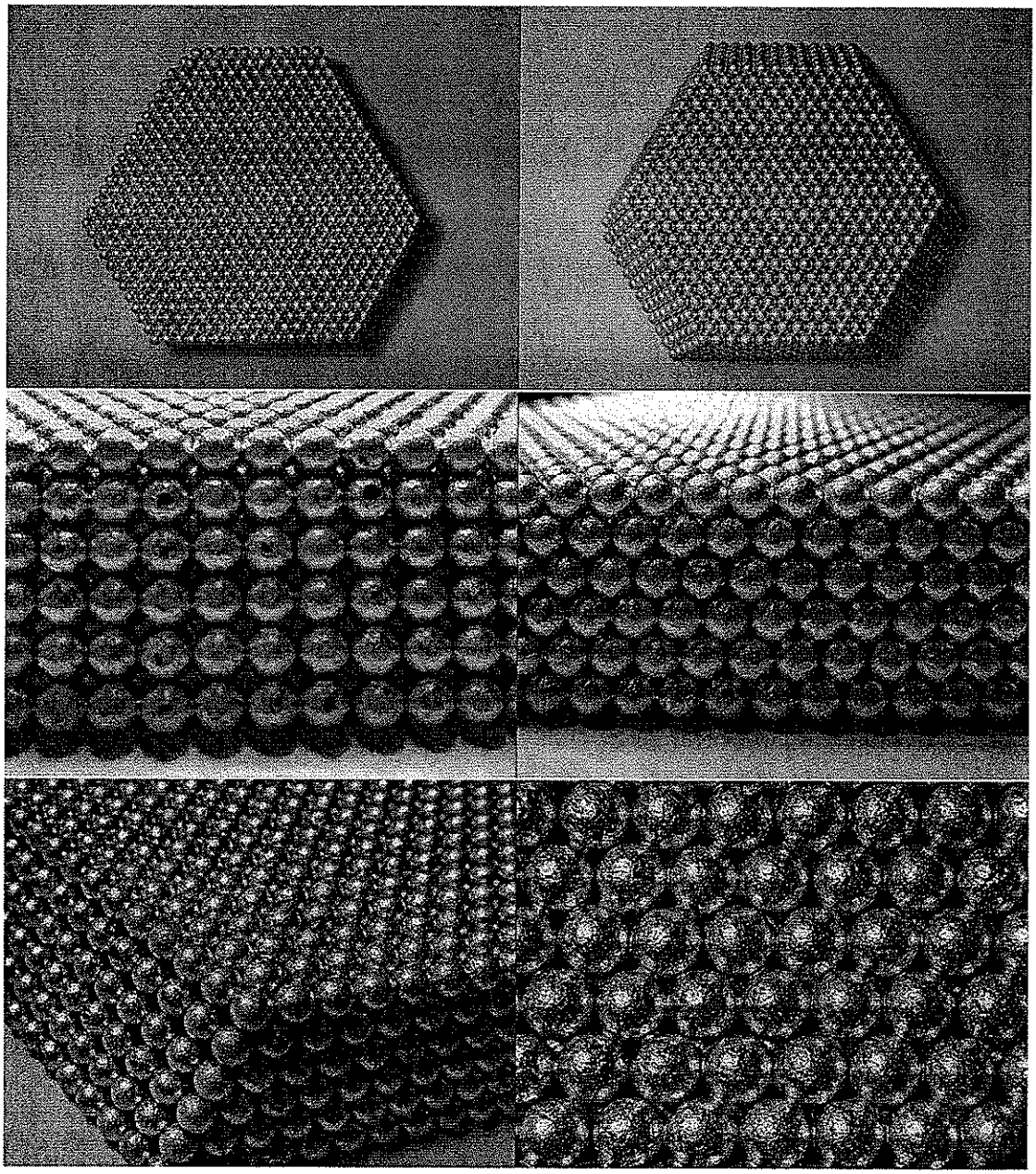

Figure 3. 2. 3 Sintered aluminum crystals.

Chapter 4 Experiment

4.1 Introduction

The description of ultrasound propagation in the strongly scattering sintered aluminum-bead samples requires the measurement of both ballistic and diffusive waves [Page *et al.*, 1995; Page *et al.*, 1996; Schriemer, 1997]. The experiments were performed in a water tank that was big enough to eliminate the interference between the straight signal through the samples and the reflected signals from the walls of the tank or from the sample surfaces. Water provided a good signal coupling between the transducers and the sample cell and made it easy to change the relative position between the sample and the transducer or miniature hydrophone.

Measurements of ballistic waves were accomplished with two large planar wave transducers, which were fixed on the manual translation stages in the water, while the samples could be translated by stepper-motor translation stages in the water and were usually placed in the far fields of both generating and receiving transducers.

Measurements of diffusive waves were accomplished with planar wave or focusing transducers and the miniature hydrophone. The face of the miniature hydrophone was small enough (400 μm diameter) to detect the sound in a single coherence area, and thus to avoid the phase cancellation effects that would occur if the average field over more

than one coherence area was detected.

The experiments were performed with both planar wave sources and point sources. For the measurement of the time intensity profile of multiply scattered sound, the plane wave geometry was used. The samples were placed deep in the far field of the plane wave transducer to achieve a good approximation to a plane wave source. Another reason to choose the plane wave geometry was that the scattering in the samples was so strong that it would last longer than 500 μs, but the available focusing transducers did not have long enough focal lengths to allow all the scattered signals through the samples to be separated from the reflected signals between the focusing transducer and the samples. For the plane wave geometry, the plane wave transducer and the sample remained fixed, while a miniature hydrophone was placed close to the opposite face of the sample to scan the central portion of the sample face to collect transmitted signals in many uncorrelated speckles.

For additional measurements of the time-dependent diffusion coefficient $D(t)$, the point source transducer was required for the *displaced point source technique*. For the point source geometry, the focusing transducer and miniature hydrophone remained fixed, while the samples were translated to collect data from many speckles.

4.2 Experimental setup

The main idea common to all experiments was generating an ultrasound pulse which would propagate through the sample, and detecting the transmitted sound by a receiving transducer or miniature hydrophone, depending on the type of measurement to be performed. The experimental setup is presented in figure 4.2.1.

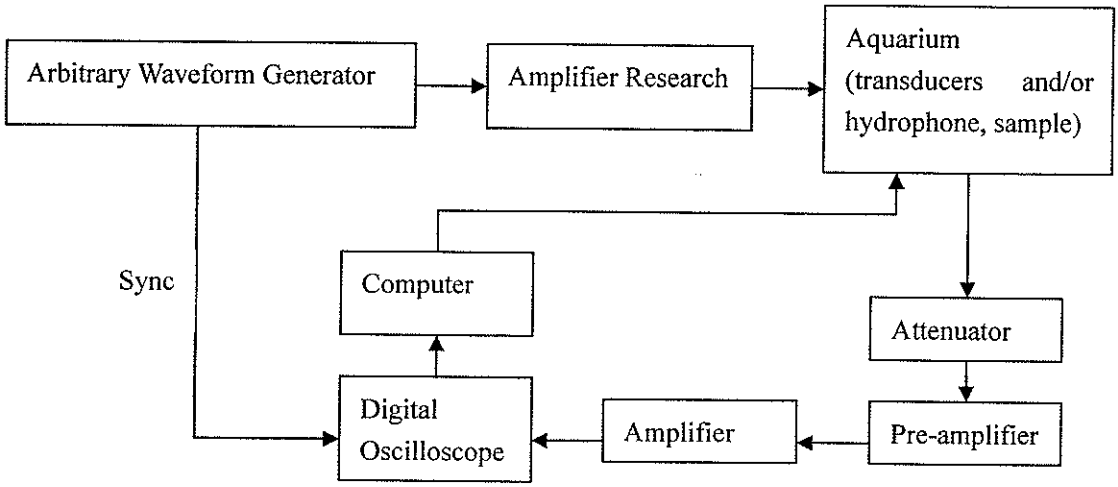

Figure 4. 2. 1 Block diagram of the experimental setup.

An electrical pulse was generated by an arbitrary waveform generator which could pre-store a specifically designed waveform, such as a Gaussian wavepacket. The pulse was then amplified by an Amplifier Research power amplifier and connected to the generating transducers, which converted the electrical energy of an electromagnetic excitation into the mechanical energy of an ultrasonic vibration. The transmitted sound through the sample was detected by a receiver which converted the ultrasonic vibration

back to an electrical signal. After the electrical signals were amplified, they were displayed on the digital oscilloscope and recorded in a personal computer.

4.3 Apparatus

4.3.1 Arbitrary waveform generator (AWG)

I used an Agilent 33220A Arbitrary Waveform Generator to generate an electrical pulse. The Agilent Technologies 33220A is a 20MHz synthesized function generator with built-in arbitrary waveform and pulse capabilities. The advantage of an AWG was that we could store up to four user-defined waveforms in non-volatile memory in addition to one in volatile memory. The waveform that I usually used for the experiments was a Gaussian wavepacket that could be designed as required. I usually used a Gaussian wave form that contained two oscillations, the so called Gauss 2 waveform. The more oscillations that the Gaussian wave form contains, the narrower the bandwidth is in the frequency domain. To create a Gaussian waveform, the AWG, which had its own IP address, was connected into the Lan first. A command "set AWG_address = SICL; lan[IP address of AWG]: GPIB0,10" was used to locate the AWG in the Lan. A program "awgsend" written by Matthew Hasselfield was used to create and store the required Gaussian waveform in the non-volatile memory of the AWG.

It was recommended that the output voltage of the AWG was around 100mV (peak to peak), which was the maximum voltage allowed to avoid saturation in the Amplifier

Research power amplifier. To generate a pulse in the AWG, the burst mode was required. To make sure that the transmitted sound through the sample vanished before the next pulse was generated, the period should be set long enough, which was 30ms for my experiments.

4.3.2 Amplifier Research (AR) power amplifier

The function of the AR power amplifier is to amplify the electronic signal generated by AWG so that the signal is big enough to excite the generating transducer and create a large enough ultrasonic pulse to enable it to be detected by the detecting transducer or hydrophone after propagating through the samples. The working frequency range of the Amplifier Research power amplifier is from 0.01 to 220 MHz, which can satisfy the needs of all of our experiments.

4.3.3 Plane wave immersion transducers

A transducer uses the piezoelectric effect to convert electrical energy into ultrasonic energy. This piezoelectric effect is reversible for transducers. The sound field of a transducer is divided into two zones: the near field and the far field. The near field is the region directly in front of the transducer where the echo amplitude goes through a series of maxima and minima, which end at the last maximum at a distance N from the transducer. The far field is the region beyond N where the sound field pressure gradually spreads out in a smoothly diverging beam. Hence, samples are always placed

in the far field of a transducer to avoid the amplitude fluctuation region. The theoretical formula for the distance N is expressed by [Panametrics, 1993]

$$N = \frac{D^2}{4\lambda}\left[1-(\frac{\lambda}{D})^2\right] \tag{4-1}$$

where D is the diameter of the surface of a transducer and λ is wavelength in water.

All transducers have beam spread. Figure 4.2.2 gives a simplistic view of a sound beam for a plane wave transducer.

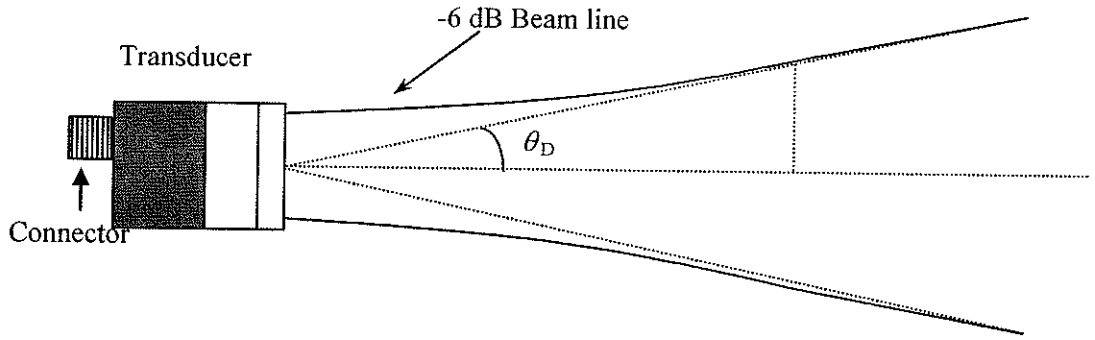

Figure 4. 2. 2 Transducer beam spread [from Yang, 2002].

The pulse-echo beam spread angle is give by equation (4-2) [Panametrics, 1993]

$$\sin(\theta_D) = 0.514c / fD \tag{4-2}$$

where θ_D is half angle spread between the -6dB points, c is velocity of the wave, f is sound frequency and D is the diameter of the transducer.

4.3.4 Focusing transducer

A focusing transducer can focus the sound beam so that it can be applied as a good

approximation to a point source. A schematic diagram of a focusing transducer is shown in figure 4.2.3. The main parameters shown in figure 4.2.3 are diameter D, the focal length F, and the length F_z and diameter B_F of the focal zone. F_z and B_F can be expressed as [Panametrics, 1993]

$$F_z = \frac{F^2}{z_F}\left[\frac{2}{1+\frac{F}{z_F}}\right] \tag{4-3}$$

$$B_F = \frac{1.028F\lambda}{D} \tag{2-4}$$

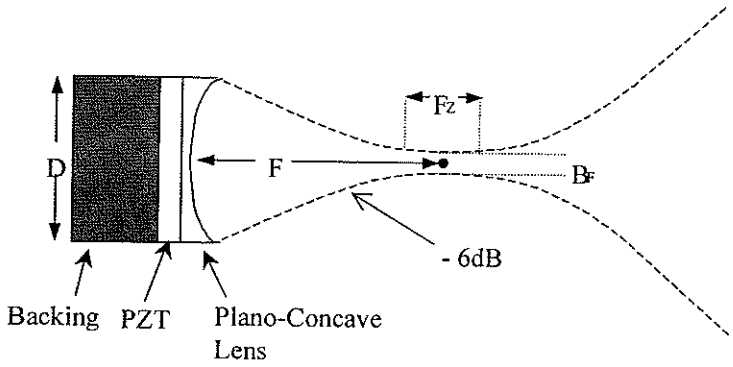

Figure 4. 2. 3 Focusing transducer [from Yang, 2002].

4.3.5 Hydrophone

A hydrophone works as a very small detecting transducer. The hydrophone I used has diameter of 0.4 mm and was used to scan the near field of the scattered waves from the samples over many single coherent speckles, which arise from interference of the scattered waves (refer to Sec. 5.2.3.1).

4.3.6 Oscilloscope

The signals were eventually monitored by a Tektronics Digital Oscilloscope (Model 544A). The oscilloscope has a GPIB interface, which makes it possible to download data to a computer directly, and to use a computer to control the data acquisition.

4.3.7 Cables

We used 58 A/U RF coaxial cable, which has an impedance of 50 Ohms to match most of our electronic equipment.

4.4 Measurement techniques and geometries

4.4.1 Ballistic measurements

Two large-element-diameter planar transducers were used to measure the phase and group velocities, and the scattering mean free path. The two transducers were aligned in the aquarium with their faces parallel, and the sample was placed between them in the far field of the two transducers. The transducers were fixed on manual stages, while the sample was translated by a motorized stage in a plane parallel to the faces of the transducers. Figure 4.2.4 shows the ballistic measurement setup. The large-element-diameter transducer measured the total pressure on its surface; it helped eliminate the background contribution due to scattered sound from the ballistic pulse. For even better performance of the cancellation of the scattered sound, the sample was translated and the transmitted fields from new ensembles of the scatters were averaged.

Only the unscattered pulse survived. From the unscattered pulse, phase and group velocities, and scattering mean free path were determined (Section 5.2.1).

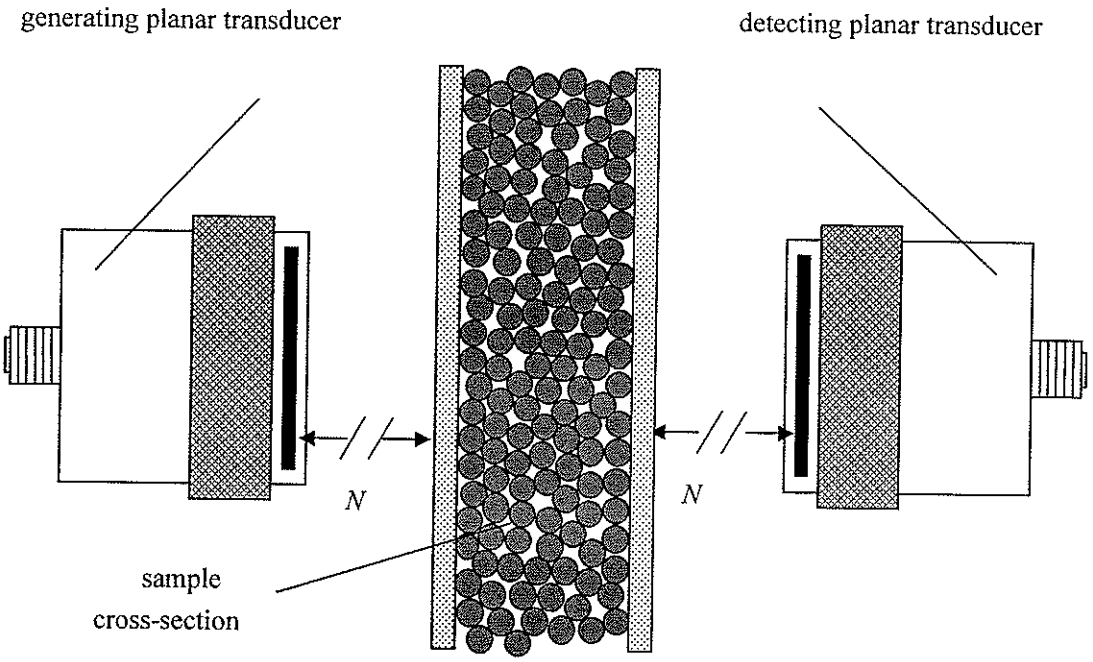

Figure 4. 4. 1 Experimental setup of ballistic measurement [from Schriemer, 1997].

4.4.2 Diffusion measurement

4.4.2.1 Plane wave source geometry

Diffusion experiments in the plane wave source geometry were performed to measure the diffusion coefficient D and the absorption time τ_a. The sample was located deep in the far field of a planar transducer. Thus, the wave front incident on the sample surface was a good approximation to a plane wave. The distance between the planar transducer and

the sample should not be too long either and was set so that the amplitude of the incident beam at the edge of the sample was at least 3dB smaller than at the centre of the sample; this reduced interference from edge effects. Since the attenuation in the sample was very huge, the reflected signal from the walls of the water tank would become comparable with the transmitted signal through the sample. To eliminate this effect, a big Styrofoam sheet, which just fitted tightly in the water tank, with a window in the center to let signal through, was made to block these stray reflected signals. The generating transducer and the sample remained fixed, while the detecting hydrophone was placed close to the opposite face of the sample, scanning the near field speckles. Figure 4.2.5 presents the diagram of the plane wave source experimental setup. The scanning spacing was determined by the wavelength of sound in water, since this distance corresponds to the near-field speckle size. Then the pulse shape of the average multiply scattered intensity of sound, which was determined by an ensemble average of the scattered wave intensity over a large number of speckles, was fitted by the time-of-flight profile predicted by the diffusion equation.

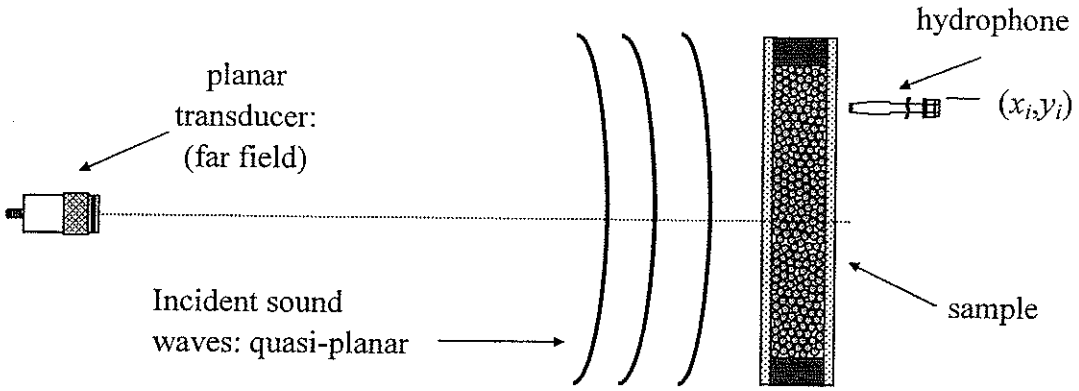

Figure 4. 4. 2 Planar wave source geometry [from Schriemer, 1997].

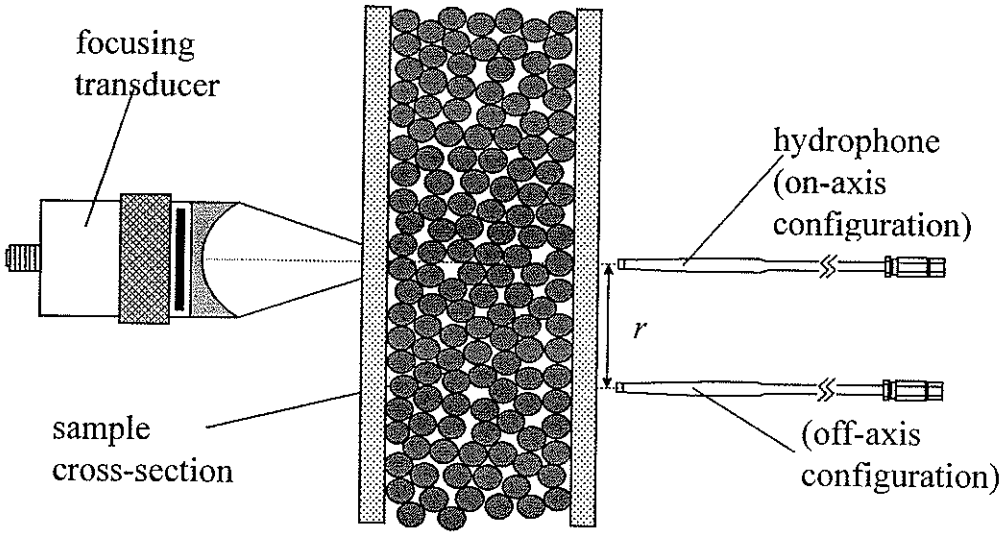

Figure 4. 4. 3 Point source geometry [from Schriemer, 1997].

4.4.2.2 Point source geometry

Measurements of the diffusion coefficient in a point source geometry led to the same result as the plane wave source geometry. In this point source measurements, the sample was placed at the focal point of a focusing transducer. The hydrophone was positioned on-axis, directly opposite the focusing transducer, and was placed close to the opposite face of the sample. The focusing transducer and the hydrophone remained fixed, while the sample was moved. A large number of uncorrelated speckles were recorded by translating the sample. The geometry of point source is illustrated in figure 4.2.6 (on-axis configuration). However, since the transmitted sound through the samples always lasted longer than 500μs for my samples, and the time for the round trip of sound between the focusing transducer and sample surface was much less than 500μs, the point source geometry was not recommended for time-of-flight intensity profile experiment.

One advantage of using point source was that the method could be extended to precisely determine the numerical value of the diffusion coefficient $D(t)$ independent of boundary condition and absorption. This extension of the method was called *displaced point source technique*. This technique is also shown in figure 4.2.6. Both on- and off-axis configurations were used in this technique. The sample was translated for both on- and off-axis configurations, respectively, to collect uncorrelated ultrasound speckles. The displacement of hydrophone in these two configurations was r. As mentioned before

(section 2.1), the transmitted flux for a point source with boundary conditions for a slab sample is

$$J(t) = \frac{e^{-r^2/4Dt} e^{-t/\tau_a}}{2\pi L^2 t} \sum_{n=1}^{\infty} A_n e^{-D\beta_n^2 t/L^2} \tag{4-5}$$

where r is the transverse distance from the point source. In our displaced point source geometry:

$$r^2 = (x_{off} - x_{on})^2 + (y_{off} - y_{on})^2 \tag{4-6}$$

The ratio of the ensemble-averaged diffuse intensity for on- and off-axis configurations is given by

$$I_{ratio} = \frac{\exp[(x_{off} - x_{on})^2 + (y_{off} - y_{on})^2]}{4Dt} \tag{4-7}$$

Hence,

$$D = \frac{-[(x_{off} - x_{on})^2 + (y_{off} - y_{on})^2]}{4t \ln I_{ratio}} \tag{4-8}$$

Note that other parameters, such as those governing the boundary conditions, the mean free path, the absorption time and the velocities, cancel out in equation (4-8).

The diffusion coefficient D in equation (2-8) was assumed to be constant. If the diffusion coefficient is not constant but is a function of time, the product Dt in equation (4-7) would be replaced by $\int_0^t D(t)dt$ [Crank, 1975]. Then $D(t)$ is given by

$$D(t) = d\left(\frac{-[(x_{off} - x_{on})^2 + (y_{off} - y_{on})^2]}{4 \ln I_{ratio}} \right) \Big/ dt \tag{4-9}$$

Chapter 5 Results and discussion

5.1 Introduction

In this chapter, the experiment results and discussion are presented. I begin with ballistic experiments to show how to measure ballistic parameters. I then discuss the results in the diffusive regime (low frequency, ~ 0.25 MHz) and discuss how to determine diffusion coefficient D in section 5.2. In section 5.3, I present the results in the localized regime (high frequency, ~ 2.25 MHz) and discuss two approaches that indicate signatures of localization.

We made five samples of different thickness. Table 5.1 shows the thickness and density of each sample.

	Thickness (mm)	Density (g/cm^2)
Sample 03	14.5	1.57
Sample 04	23.05	1.55
Sample 05	14.5	1.55
Sample 06	23.5	1.57
Sample 07	8.27	1.475

Table 5.1. Thickness and density of the five samples.

5.2 Diffusive regime

5.2.1 Ballistic measurements

5.2.1.1 Extraction of the coherent pulse

Ultrasound propagating through a disordered medium has both coherent and incoherent components. The coherent component has a definite phase relation to the incident pulse, which propagates straight through a random medium, whereas the incoherent component scattered many times in the random medium has random phase contributions. Since the incoherent component undergoes a random walk, it always travels longer than the coherent component.

Two 1.5" diameter transducers at a central frequency of 0.25 MHz were used in this experiment. The large surface of the planar transducer averages the pressure of sound incident on it, and, because of the random phases of the incoherent component, it is averaged out. To improve the phase cancellation of the scattered sound, the sample was translated in grid with a 5-mm spacing, which corresponds to the incident beam width and all of the transmitted pulses were averaged again to eliminate the contribution of the scattered sound and extract the coherent component.

The upper panel of figure 5.2.1 shows three typical transmission waveforms obtained using a 0.25 MHz plane wave generating transducer and the low frequency hydrophone

detector. From the beginning of the waveforms until about 45μs, the three speckles appear very similar in phase and amplitude. After 45μs, the waveforms are no longer very similar, but there is still a little coherent trend shown after 45μs, which may be because there is some degree of short-range order in the random sample. The solid curve in the lower panel of figure 5.2.1 is the average waveform of 25 speckles.

As frequency goes up, the scattering of sound becomes dramatically stronger. Above 0.5 MHz, scattered sound was dominant and no clear coherent pulse could be extracted. Figure 5.2.2 shows some typical waveforms at 0.5 MHz, measured with 1" diameter transducers. Even though the first one or two oscillations appear coherent, there is no way to extract the entire coherent pulse.

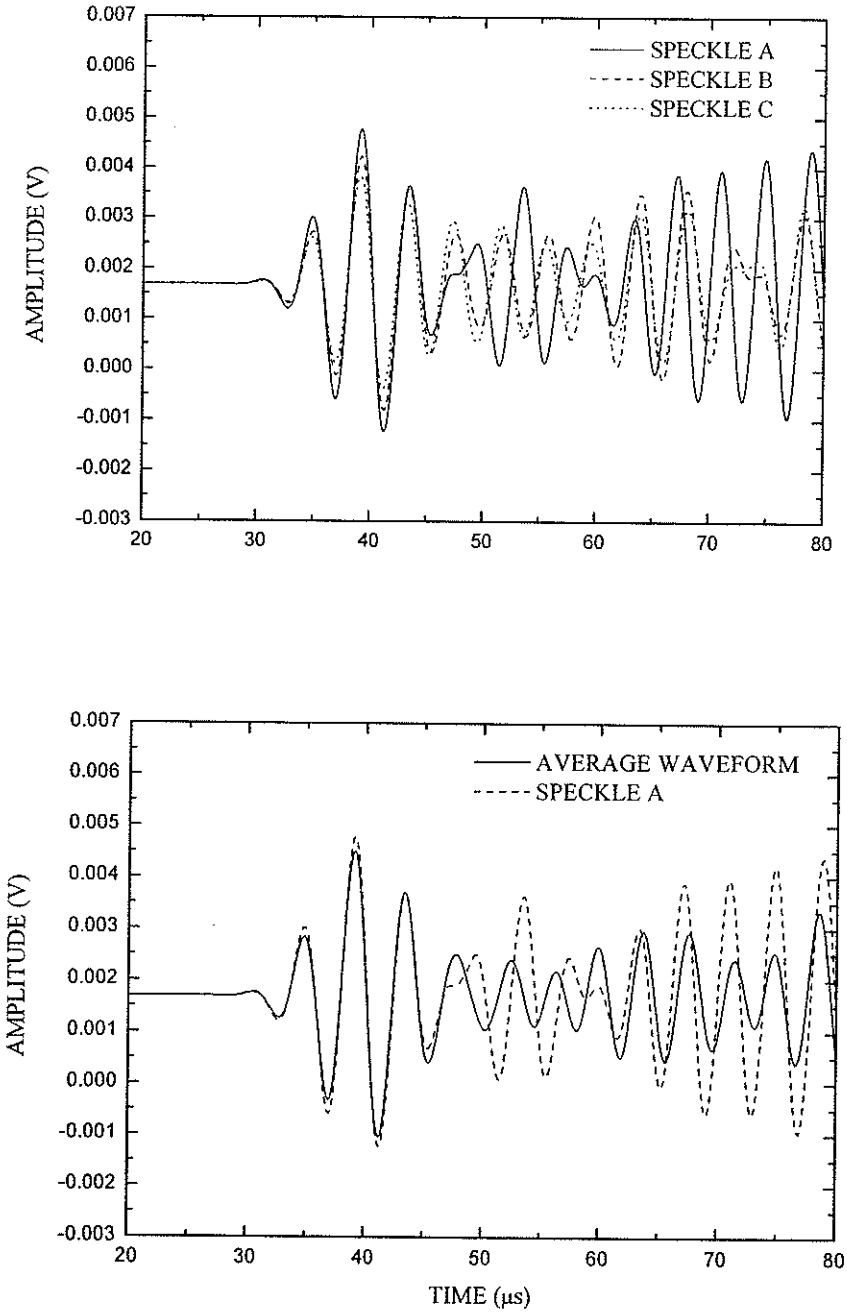

Figure 5. 2. 1 Upper figure: 3 typical transmitted speckles at 0.25 MHz for sample 05 (L = 14.5 mm), showing coherent and incoherent components. Lower figure: The solid pulse in the lower panel is the average of 25 transmitted pulses, compared to one typical transmitted speckle (dashed curve).

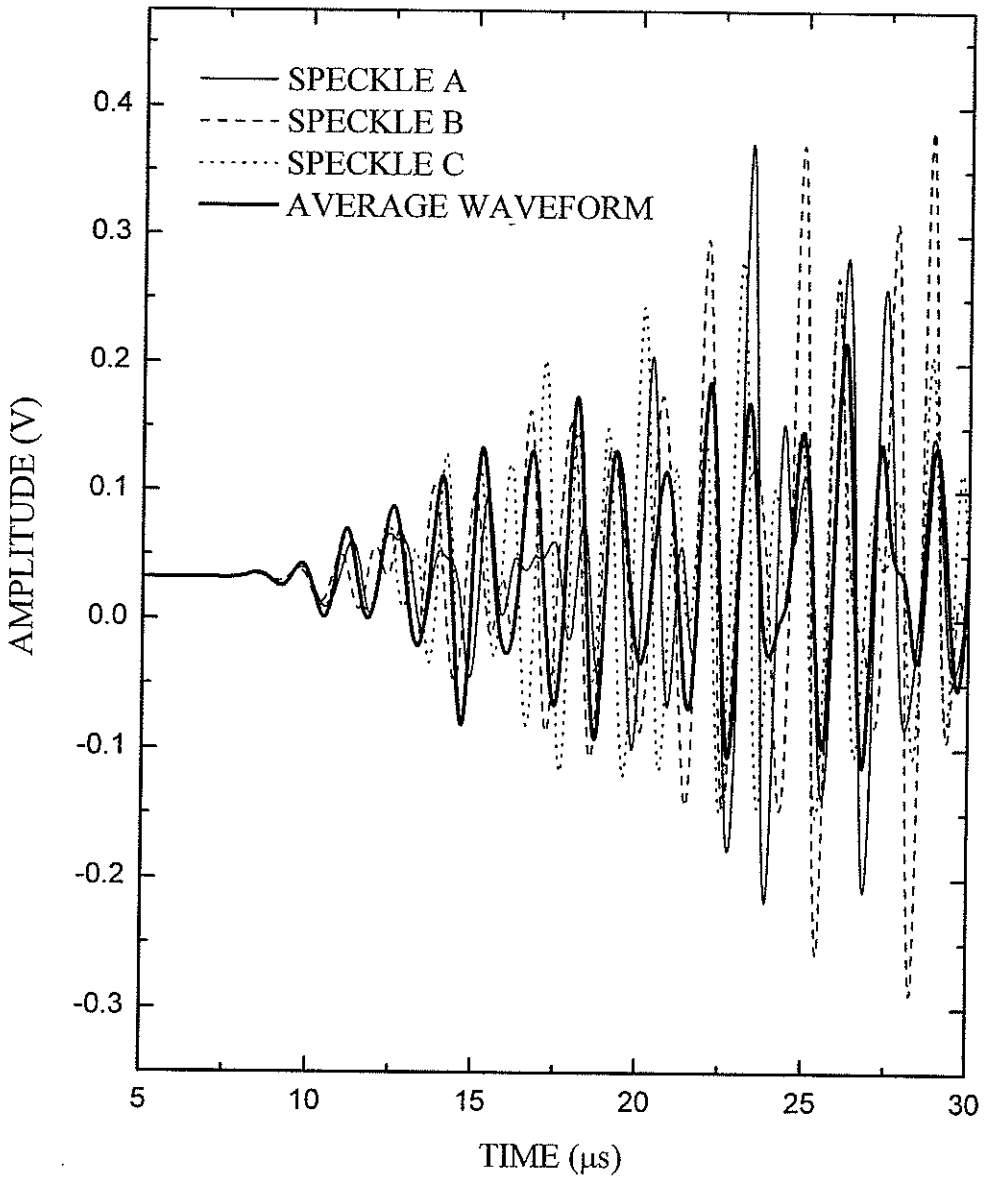

Figure 5. 2. 2 Transmission speckles at 0.5 MHz for sample 05 (L = 14.5 mm). The bold averaged pulse shows no apparent ballistic pulse.

5.2.1.2 The scattering mean free path

When a sound pulse propagates through a sample of thickness L, its original intensity I_0 is attenuated as it is scattered out of its original direction. The transmitted intensity I is expressed as

$$I = I_0 \exp(-L/l_s) \tag{5-1}$$

where l_s is defined as the scattering mean free path. The scattering mean free path then can be expressed as

$$l_s = \frac{-L}{\ln(I/I_0)} = \frac{-L}{2\ln(A/A_0)} \tag{5-2}$$

where A and A_0 are transmitted and incident amplitudes, respectively.

To determine the scattering mean free path, the ratio of the FFT of the transmitted and incident pulses was calculated. Since waves were reflected at the interfaces between water and the sample surfaces, part of energy was lost. Hence, the correction for reflection was needed. The corrected scattering mean free path in the low frequency range is illustrated in figure 5.2.3. The scattering mean free paths for sample 5, 6 and 7 decreased as frequency increased (expect for sample 7), and were smaller than the diameter of the aluminum beads (4.11 mm) in this frequency range, showing scattering was very strong in this regime. Since we could not extract good ballistic pulses from the total waveforms at higher frequencies, the scattering mean free path was difficult to measure, but it is almost certainly smaller than in the low frequency range.

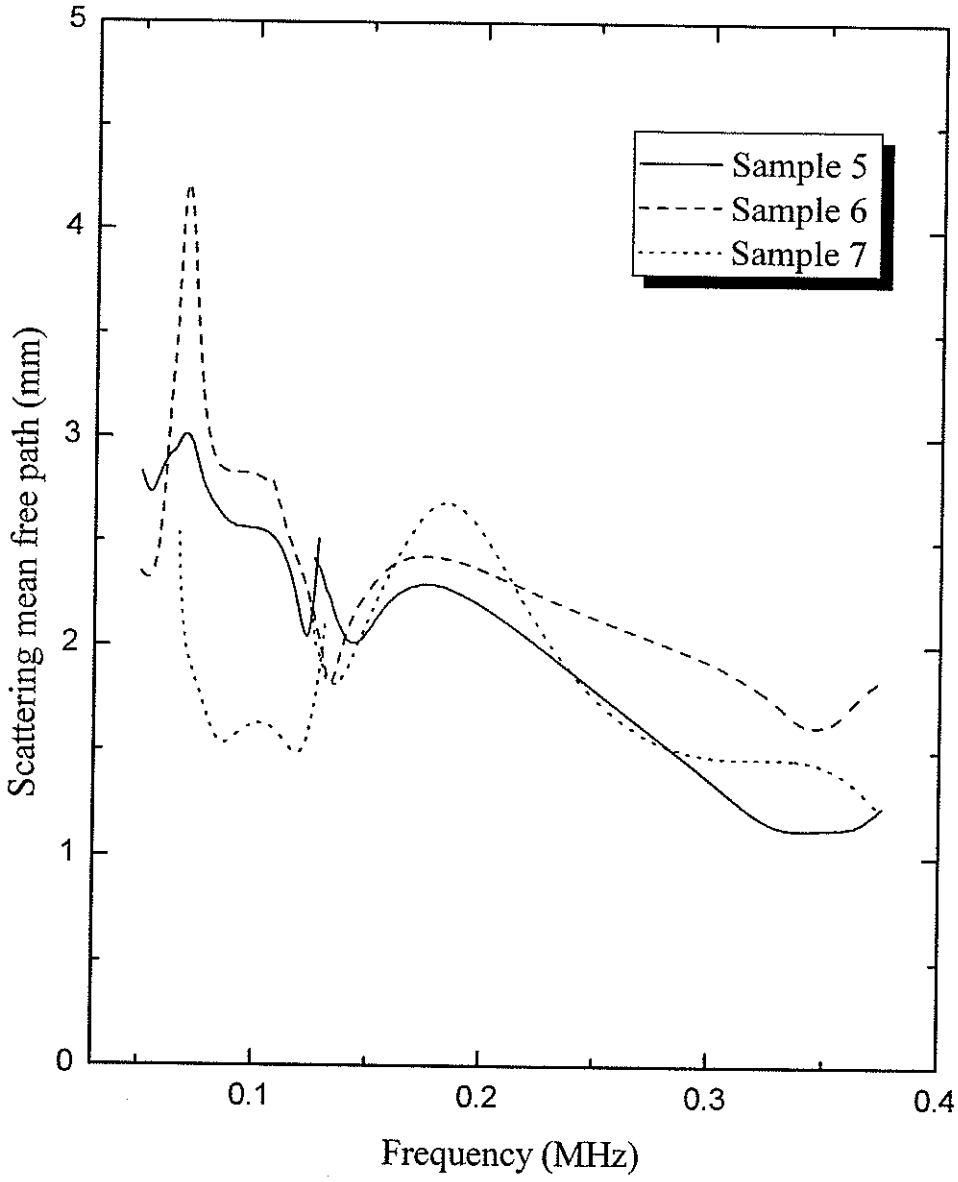

Figure 5. 2. 3 Scattering mean free path dependence on frequency.

5.2.1.3 Phase velocity

The phase velocity of a wave is the rate at which the phase oscillations of the wave propagate in space. This is the velocity at which the phase of any one frequency component of the wave will propagate. The phase velocity may be determined using the relation

$$v_{phase} = \frac{L_{sample}}{\Delta t_{phase}} \tag{5-3}$$

where L_{sample} is the thickness of the sample and Δt_{phase} is the transit time that a wave will take to propagate through the sample at one certain frequency.

To determine Δt_{phase} experimentally, we needed both the transmitted pulse, and the incident pulse which was determined from the reference pulse acquired by removing the sample from between the two transducers. Then the transit time Δt_{pulse} between the reference and transmitted pulses relative to water was only dependent on the effect of the sample and walls on the propagation time. The experimental configuration for acquiring transmitted and incident pulses is shown in figure 5.2.4.

The time correction that needs to be subtracted from the reference pulse through water in order to transform it into the incident pulse is

$$\Delta t_{correction} = \frac{L_{sample} + 2d_{wall}}{v_{water}} - \frac{2d_{wall}}{v_{wall}} \tag{5-4}$$

where d_{wall} is the thickness of the sample wall, v_{water} and v_{wall} are the phase velocities in

water and wall material, respectively. Meanwhile, the transmitted pulse was truncated around 50 μs to eliminate the effect of multiple scattering to obtain the ballistic pulse. One example of the time corrected reference and ballistic pulse are presented in figure 5.2.5.

The time difference Δt_{phase} was determined by the following expression.

$$\Delta t_{phase} = \frac{\Delta\phi}{\omega} = \frac{\Delta\phi}{2\pi f} \tag{5-5}$$

where $\Delta\phi$ is the phase difference between the ballistic and reference pulses, ω and f are angular frequency and frequency.

The phase difference $\Delta\phi$ was measured from the complete FFTs of the reference and transmitted waveforms by subtracting the reference phase from the transmitted phase. The typical results for the frequency dependence of the phase of the transmitted and reference pulses, and the phase difference are illustrated in figure 5.2.6. Since the phase difference $\Delta\phi$ from the FFT analysis contains an unknown phase shift of $n2\pi$, where n is an integer, a method to determine n is needed. The best method to achieve this is to measure $\Delta\phi$ down to sufficient low frequencies that the wavelength is greater than the sample thickness, so $n = 0$. Unfortunately, even though the frequencies are quite low in this case (down to 0.1 MHz), they were not low enough to determine n unambiguously. Instead we used a different criterion: the correct value of n was determined by comparing

the phase velocities for samples of different thicknesses. This criterion was successful, since only one set of values of n was found that gave consistent velocity results for all samples. Figure 5.2.7 shows the experimental phase velocities for sample 5, 6 and 7, determined using this method.

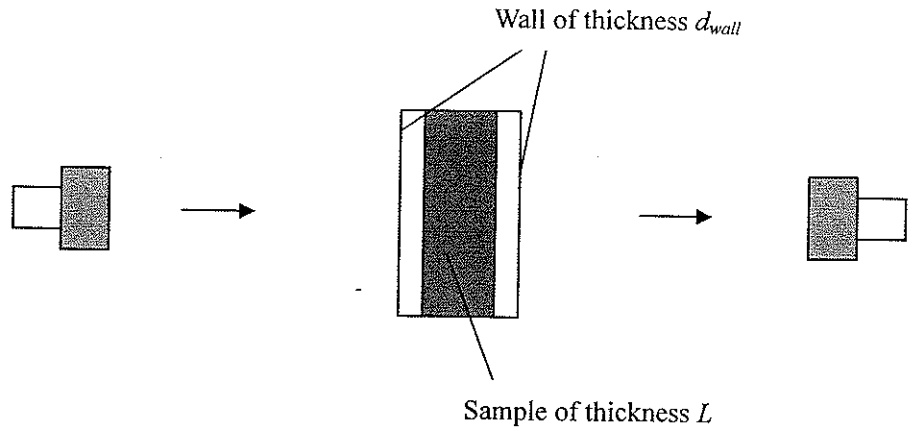

Transmitted pulse acquiring geometry

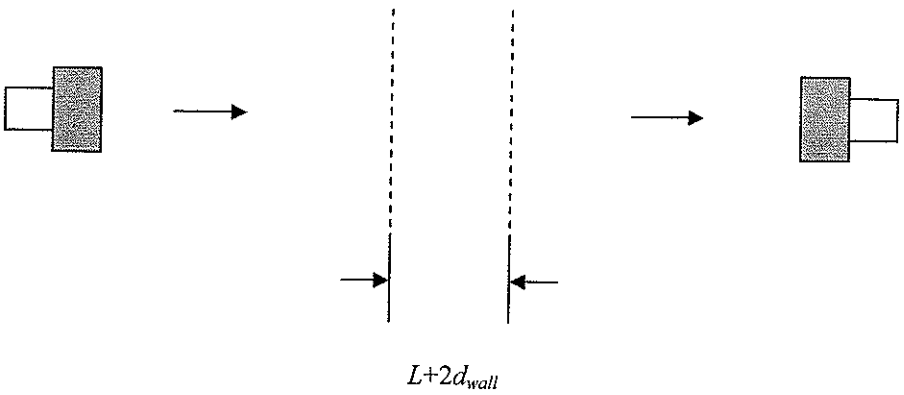

Reference pulse acquiring geometry

Figure 5. 2. 4 Experimental geometry for measuring the transmitted and reference pulses.

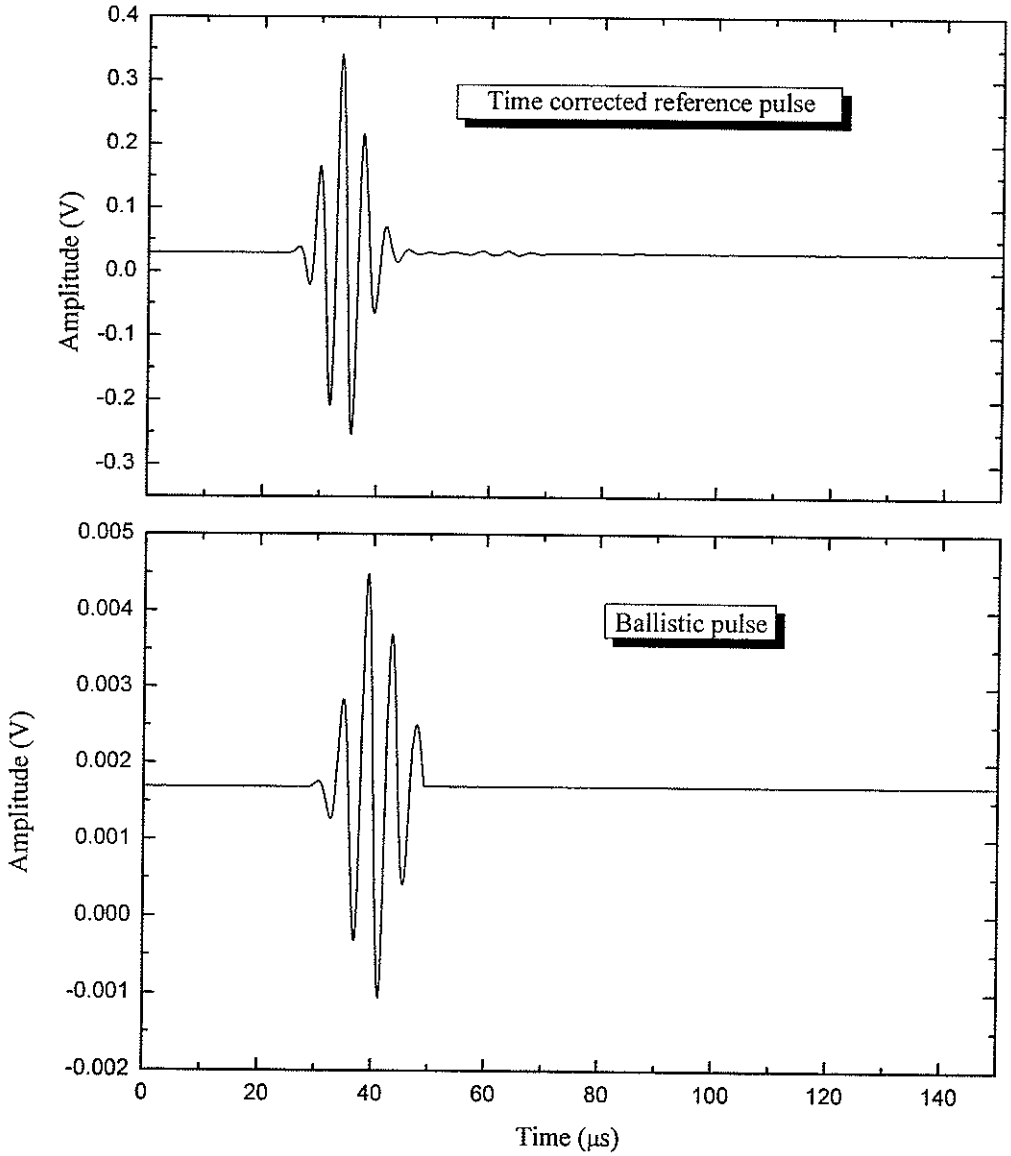

Figure 5. 2. 5 Reference and ballistic pulse at 0.25 MHz.

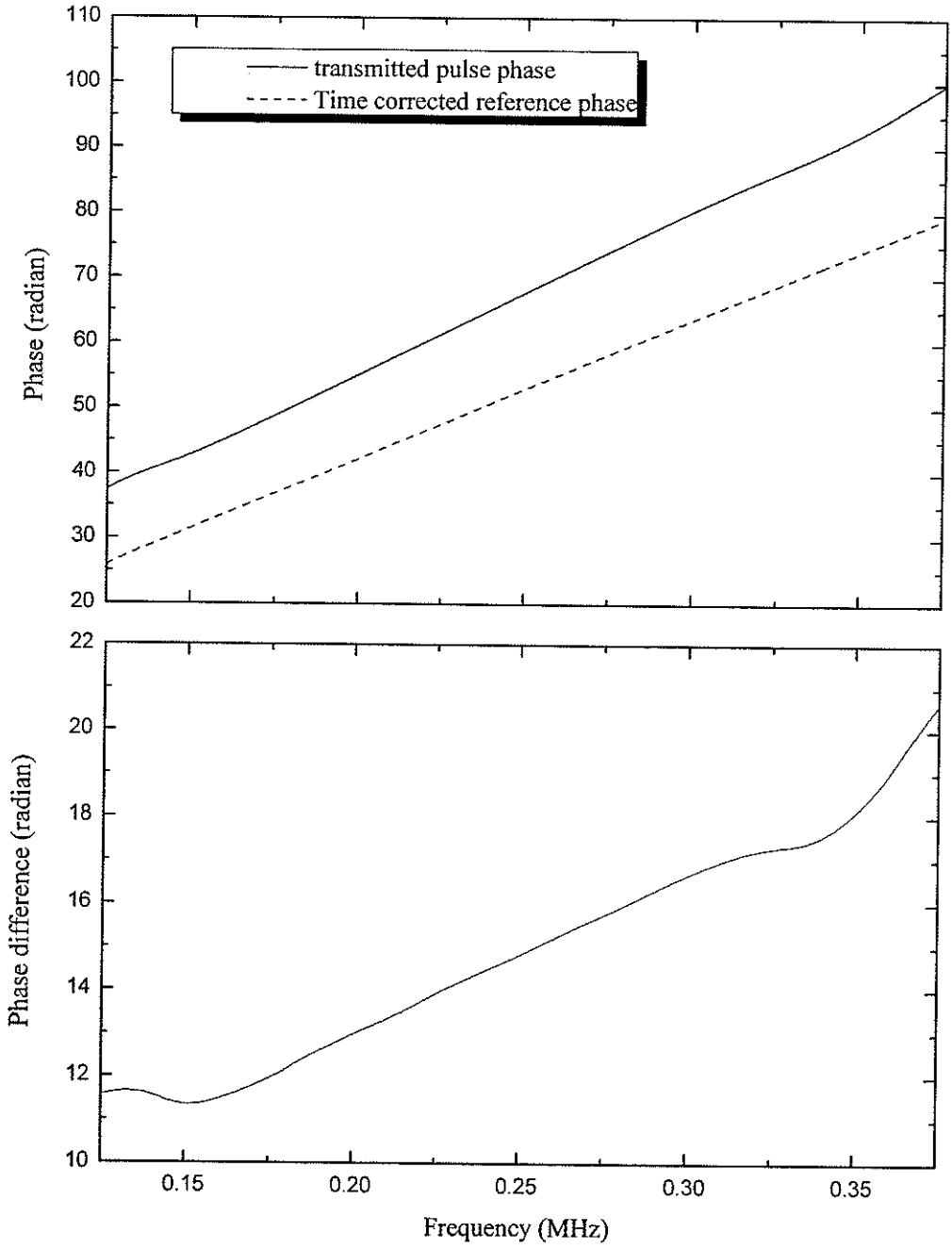

Figure 5. 2. 6 Upper panel: Phase of the ballistic and reference pulses; Lower panel: Phase difference between the ballistic and reference pulse.

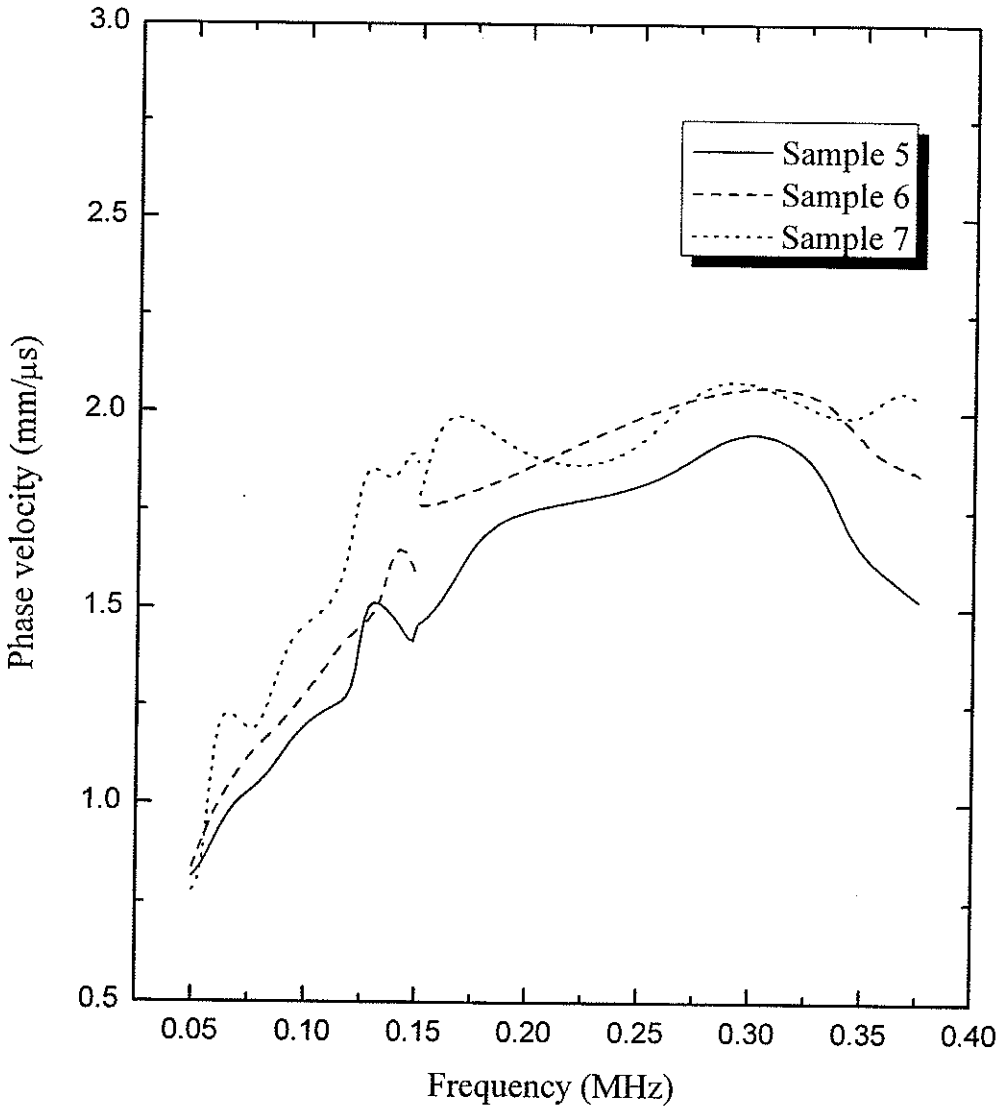

Figure 5. 2. 7 Phase velocity of different samples.

5.2.1.4 Group velocity

The group velocity of a wave is the velocity with which the wave's envelope propagates through space. As for the phase velocity, the group velocity is given by the ratio of sample thickness to propagation time. However, the transit time for group velocity is calculated in a different way from that of the phase velocity, and so we use Δt_{group} to denote it. Hence, the group velocity is expressed as

$$v_{group} = \frac{L_{sample}}{\Delta t_{group}} \tag{5-6}$$

The time correction due to the effect of sample thickness and wall thickness was also required for group velocity calculations. The formula to determine the group velocity, which corresponds to equation (5-3), is therefore given by

$$v_{group} = \frac{L_{sample}}{\Delta t_{pulse} - \Delta t_{correction}} = \frac{L_{sample}}{\Delta t_{pulse} - \dfrac{L_{sample} + 2d_{wall}}{v_{water}} - \dfrac{2d_{wall}}{v_{wall}}} \tag{5-7}$$

Here, Δt_{group} was experimentally determined from the time difference between the peaks of the envelopes of the ballistic and reference pulses. Since different frequency components of pulses may travel at different speeds, to determine the group velocity at different frequencies, both transmitted and reference pulses were digitally filtered to limit the signal to a Gaussian pulse with a relative narrow bandwidth before their envelopes were determined.

The results of filtering the 0.25 MHz data (figure 5.2.5), with a Gaussian band pass

function of central frequency $f = 0.25$ MHz and bandwidth of $w = 2\sigma = 0.02$ MHz are presented in figure 5.2.8. The dashed curves show typical envelopes of the corresponding pulses. Figure 5.2.9 shows the group velocity in the low frequency range (0.05 – 0.375 MHz). There are very large fluctuations in the group velocity. The most likely cause of these fluctuations is resonant-like modes of several coupled beads. (Note that the wavelength in aluminum λ_{Al} varies from about 30 to 4 bead diameters over this frequency range, and wavelength in the sintered network varies from about 3 to 1 bead diameters). The average group velocity in this frequency range is around 2.1 mm/us, which is a little larger than the phase velocity, but still less than the longitudinal velocity in aluminum (6.4 mm/μs).

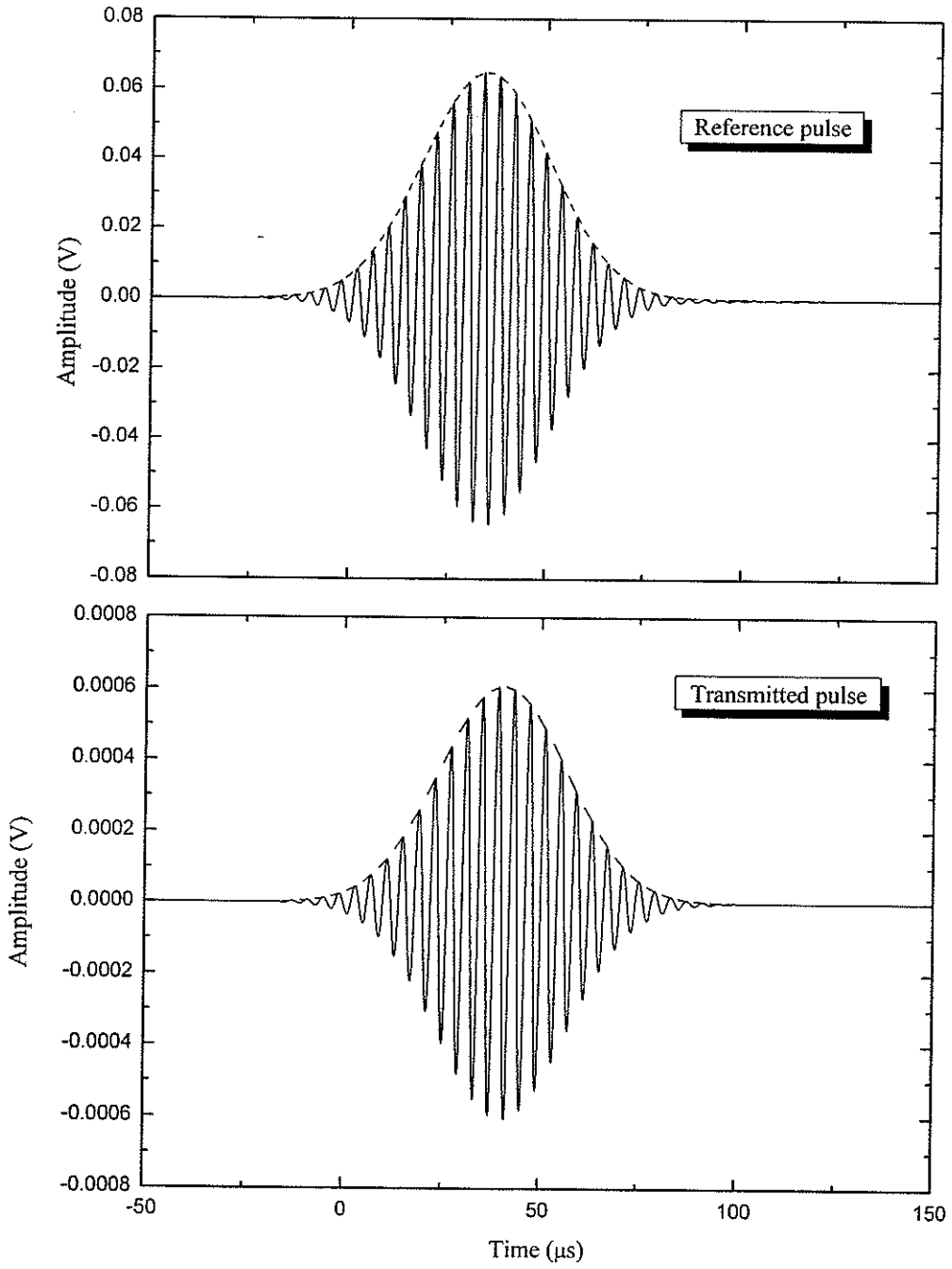

Figure 5. 2. 8 Filtered reference and ballistic pulses centered at 0.25 MHz with bandwidth 0.02 MHz. The dashed curves are envelopes.

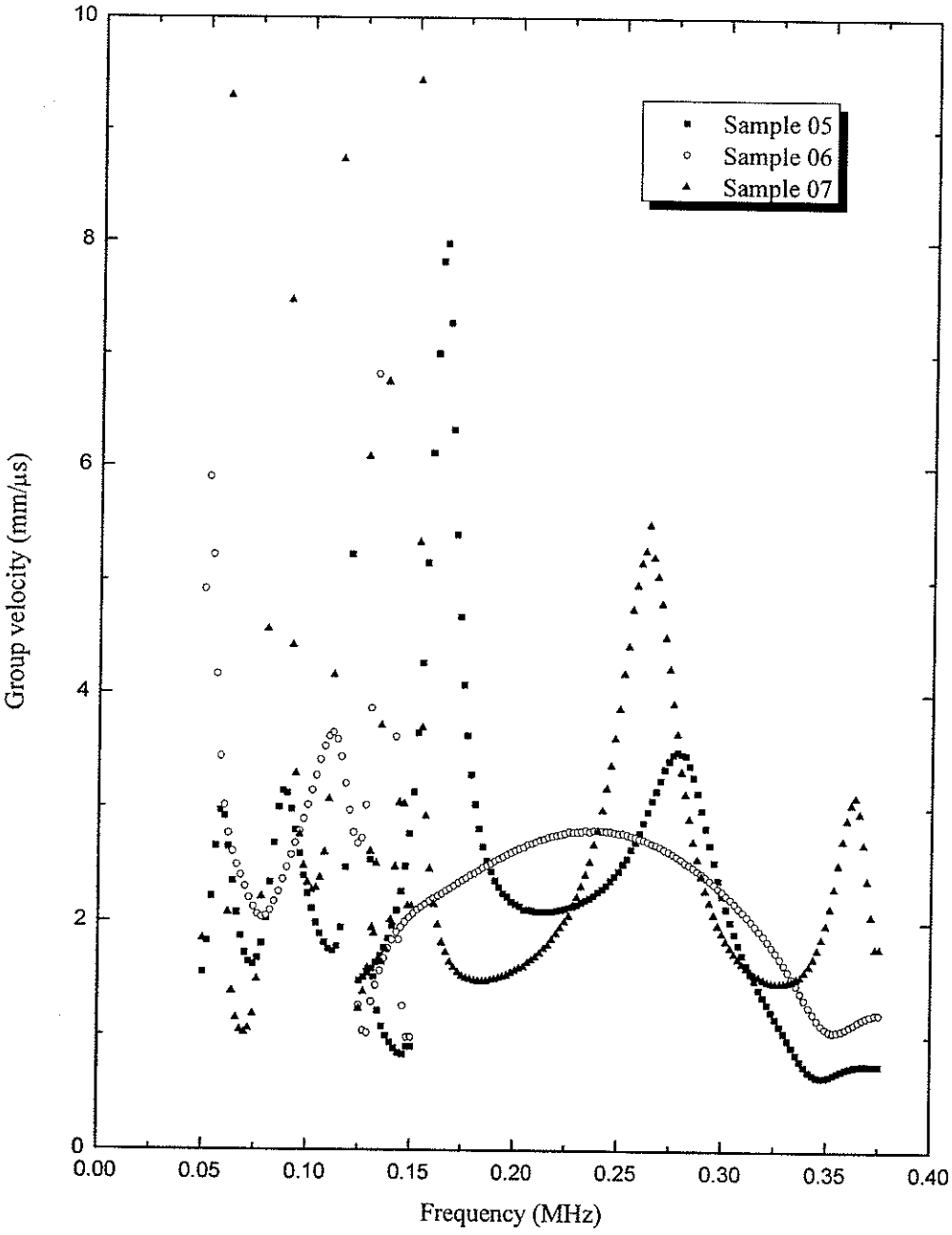

Figure 5. 2. 9 Group velocities of different samples.

5.2.3 Diffusive transmission

5.2.3.1 Ensemble averaging

The scattered waves in the near field of the samples interfere with each other to give rise to a random speckle pattern, which fluctuates in both phase and amplitude across the surface of the sample. Each speckle corresponds to a coherence area of the interference pattern. In the near field of the sample, the size of a speckle, or coherence area, is approximately equal to λ^2, where λ is wavelength in water [Page *et al.*, 1995, Schriemer, 1997]. The cross section of the speckle pattern of multiply scattered waves is illustrated in figure 5.2.10 for Schriemer's 20-mm-thick glass bead sample in water [Schriemer, 1997].

To detect the transmitted field, we used a hydrophone that is smaller than the coherence area of the speckles to avoid phase cancellation. The near field speckle pattern was scanned over many single coherence areas in a plane parallel to the surface of the sintered aluminum disordered samples, and then the intensity of all the speckles was averaged to determine the average transmitted intensity. Because the size of the speckles is λ^2, the spacing of the grid over which hydrophone was scanned was approximately equal to the ultrasonic wavelength in water.

As mentioned before, for the diffusive transmission experiments, it is better to use a plane wave source rather than a point source due to the long transmission times for scattering in

the sample. Since our "plane wave" was generated by a 1.5" diameter transducer, the source was not an ideal plane wave. The measured amplitude profile of the input beam form of the 0.25 MHz transducer is shown in the upper panel of figure 5.2.11. Ballistic pulses should have no contribution to the diffusive transmission; hence, we need to subtract the ballistic pulse from each individual transmitted speckle. To do so, we first need to correct the transmitted speckles in amplitude and phase to eliminate the deviations from ideal plane wave behavior of the source. The amplitude and phase difference of the reference pulses at all measured speckle positions were found relative to the central position in order to correct the amplitude and phase of corresponding transmitted speckles. A *C* program "correctgrid.c" was used for this purpose. The corrected field pattern for the 0.25 MHz transducer is shown in the lower panel of figure 5.2.11. The same correction was applied to transmitted speckles as well. We then averaged all the corrected transmitted speckles to determine the ballistic pulse, which is illustrated in figure 5.2.12, and finally subtracted the ballistic component from individual corrected transmitted speckles, leaving the purely diffusive component. Three typical corrected diffusive transmitted speckles at 0.25 MHz are presented in figure 5.2.13.

Diffusion properties may be dependent on frequency. To exhibit the frequency dependence, the diffusive transmitted speckles were digitally filtered by a Gaussian band pass filter with a narrow bandwidth which was usually 10% of the central frequency. The filtered pulses of the typical diffusive transmitted speckles in figure 5.2.13 are shown

in figure 5.2.14.

To construct the mean diffuse intensity, the phase information contained in the individual speckles was ignored and the waveform envelopes were determined. The envelopes of the three filtered transmitted speckles in figure 5.2.14 are showed in figure 5.2.15. Then the envelopes were squared to achieve intensities, which were averaged to produce the ensemble averaged diffuse intensity. An example of a diffusive pulse centered at 0.25 MHz with 0.02 MHz bandwidth for sample 05 is illustrated in figure 5.2.16.

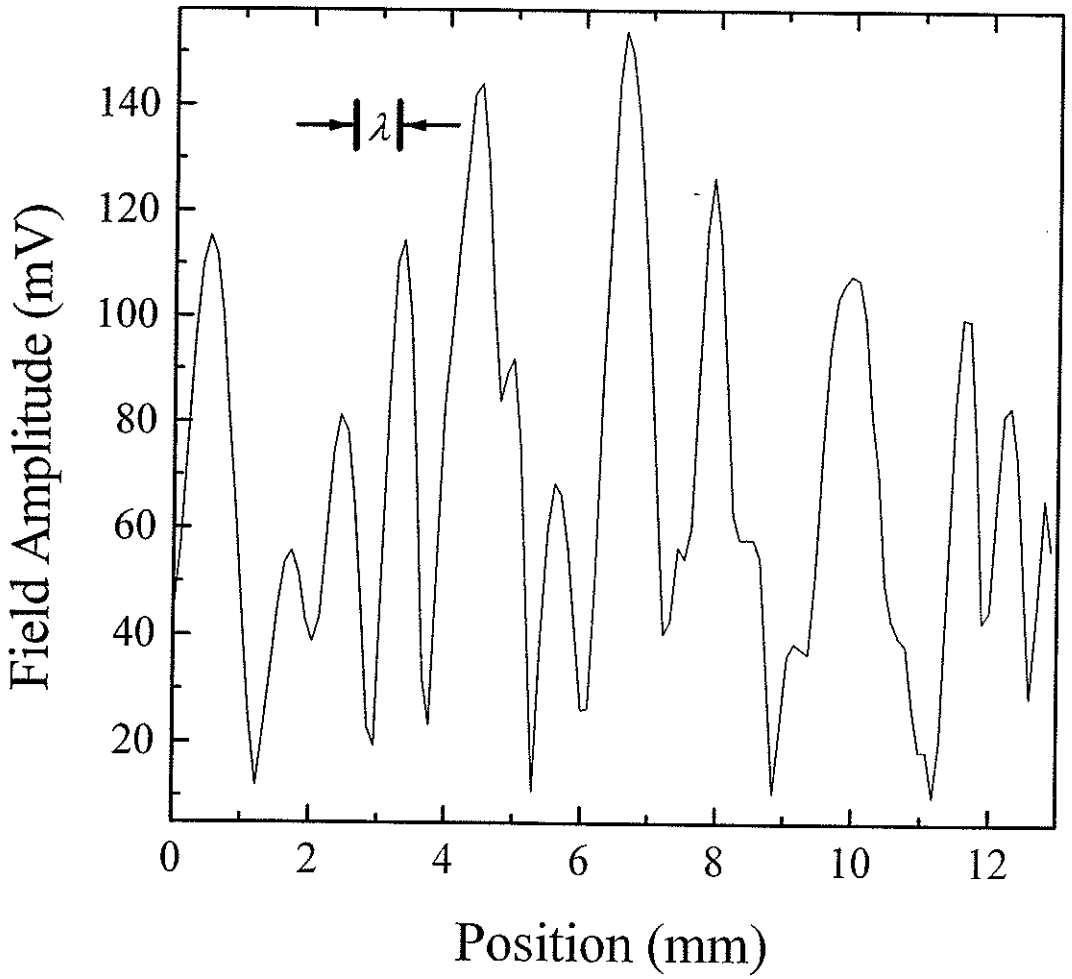

Figure 5. 2. 10 The cross section of the acoustic speckle pattern of multiply scattered sound [from Page *et al.*, 1995; Schriemer, 1997].

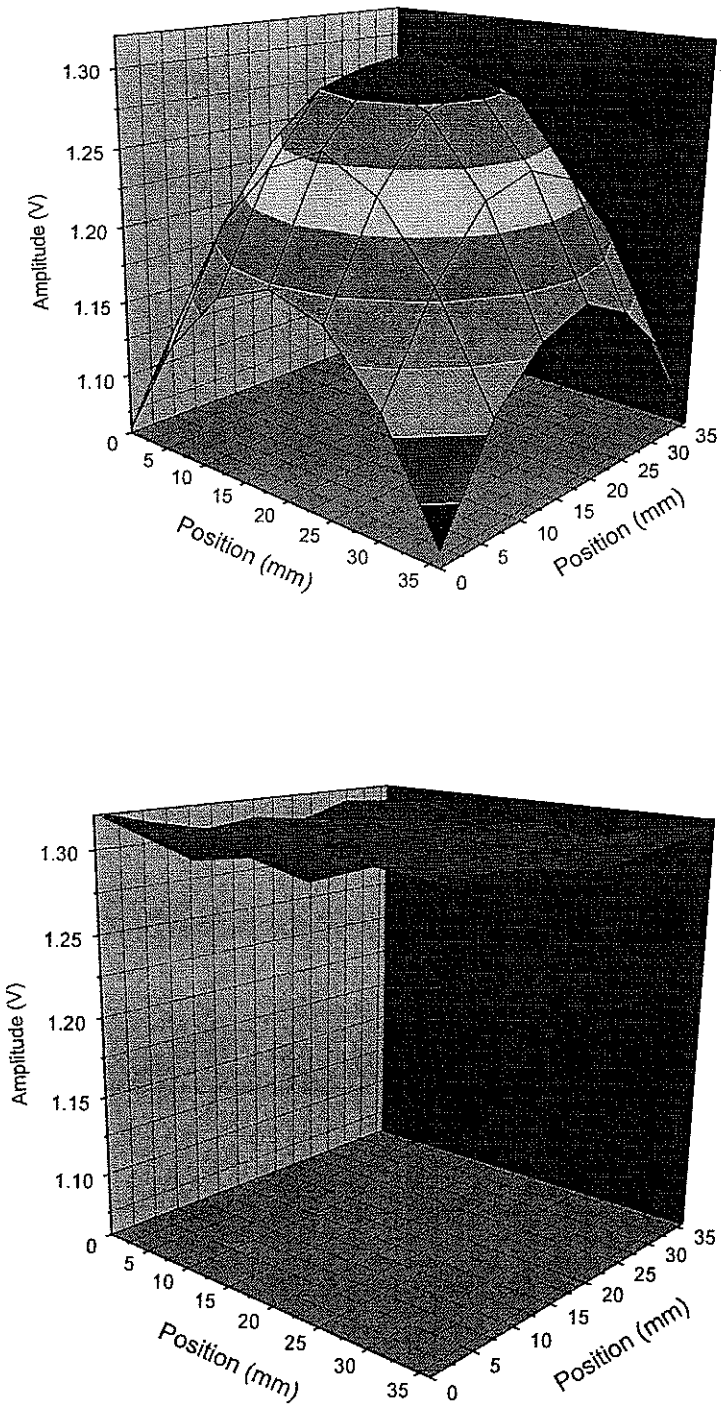

Figure 5. 2. 11 Upper figure: the field pattern of 0.25 MHz transducer. Lower figure: corrected field pattern.

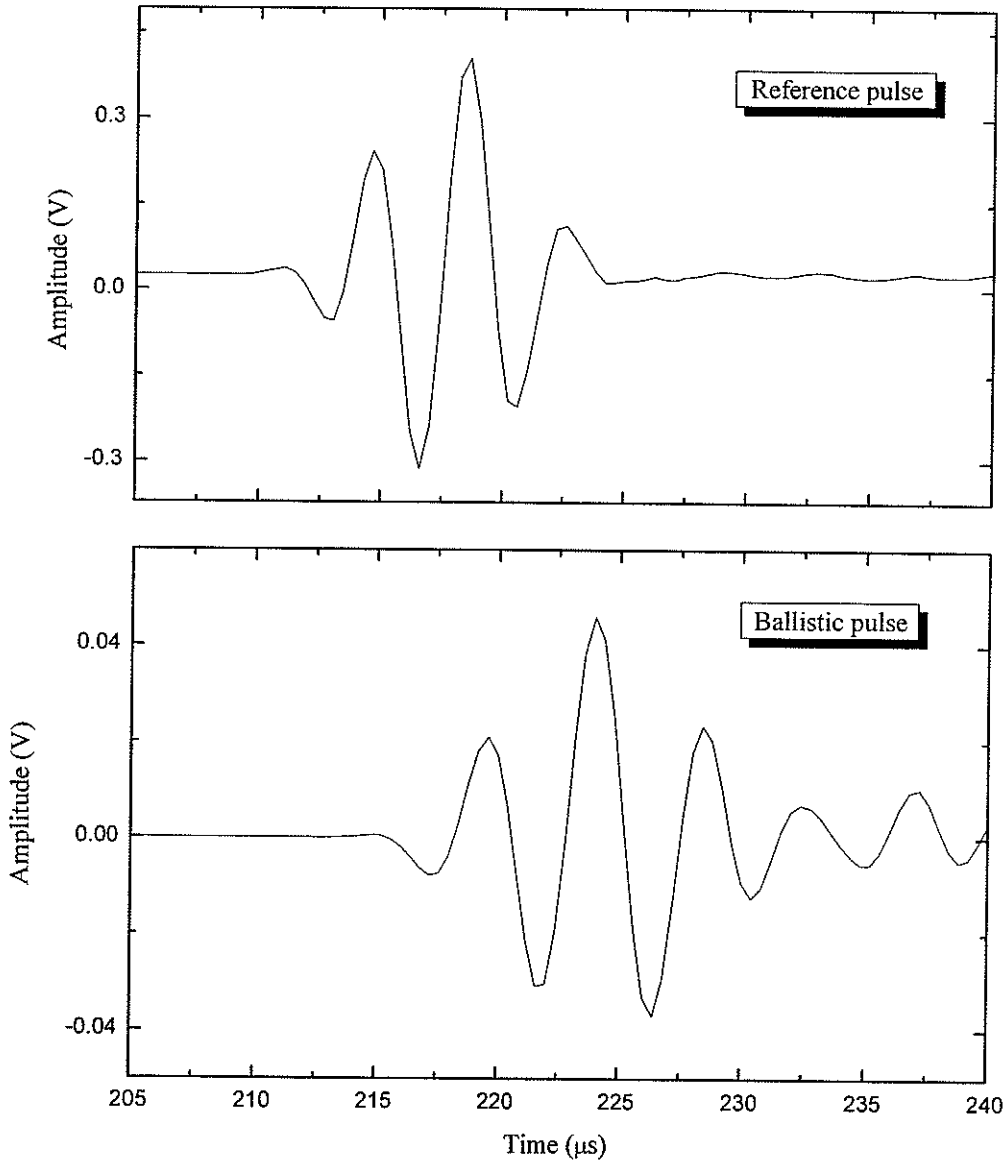

Figure 5. 2. 12 Reference and ballistic pulses measured in the diffusive measurement at 0.25 MHz.

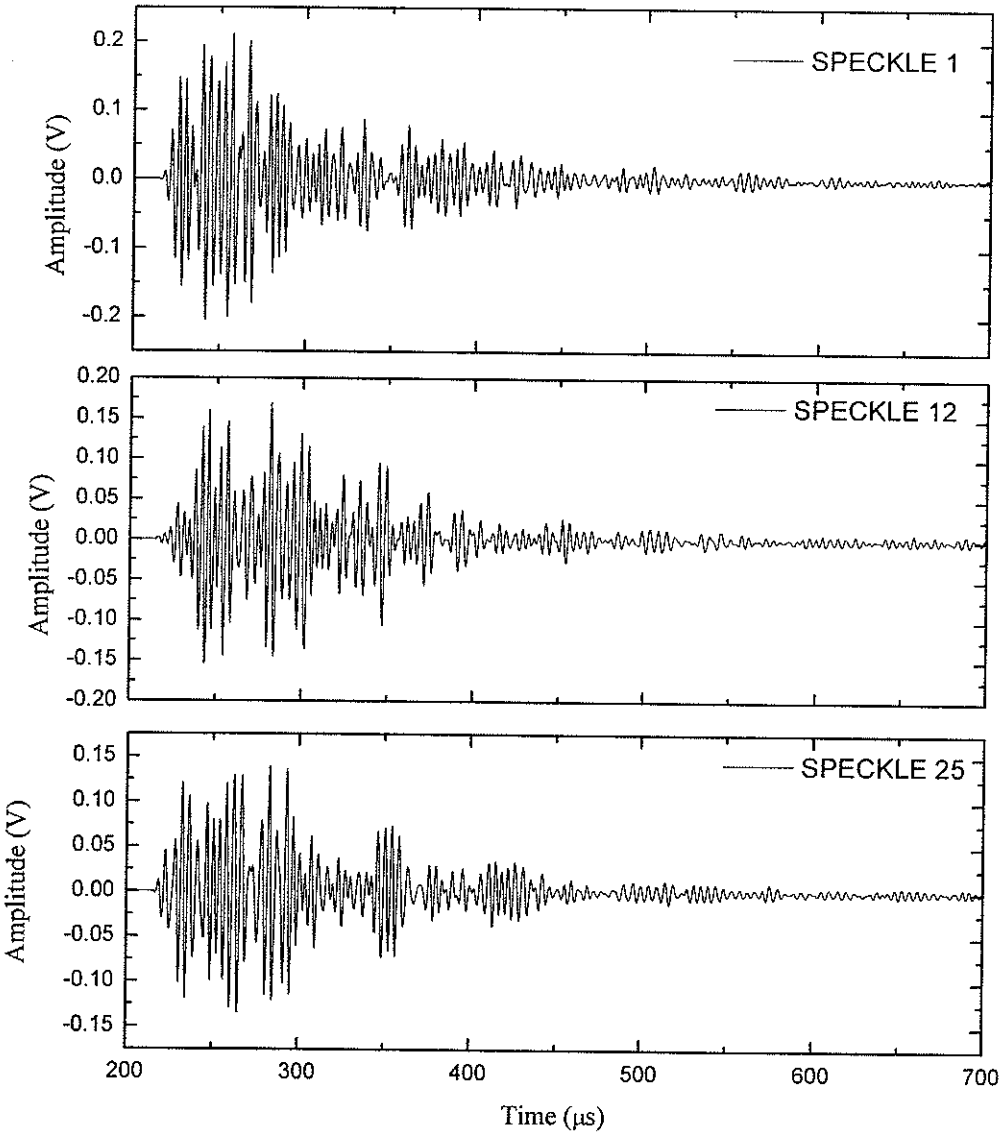

Figure 5. 2. 13 Wave forms in three typical transmitted speckles at 0.25 MHz.

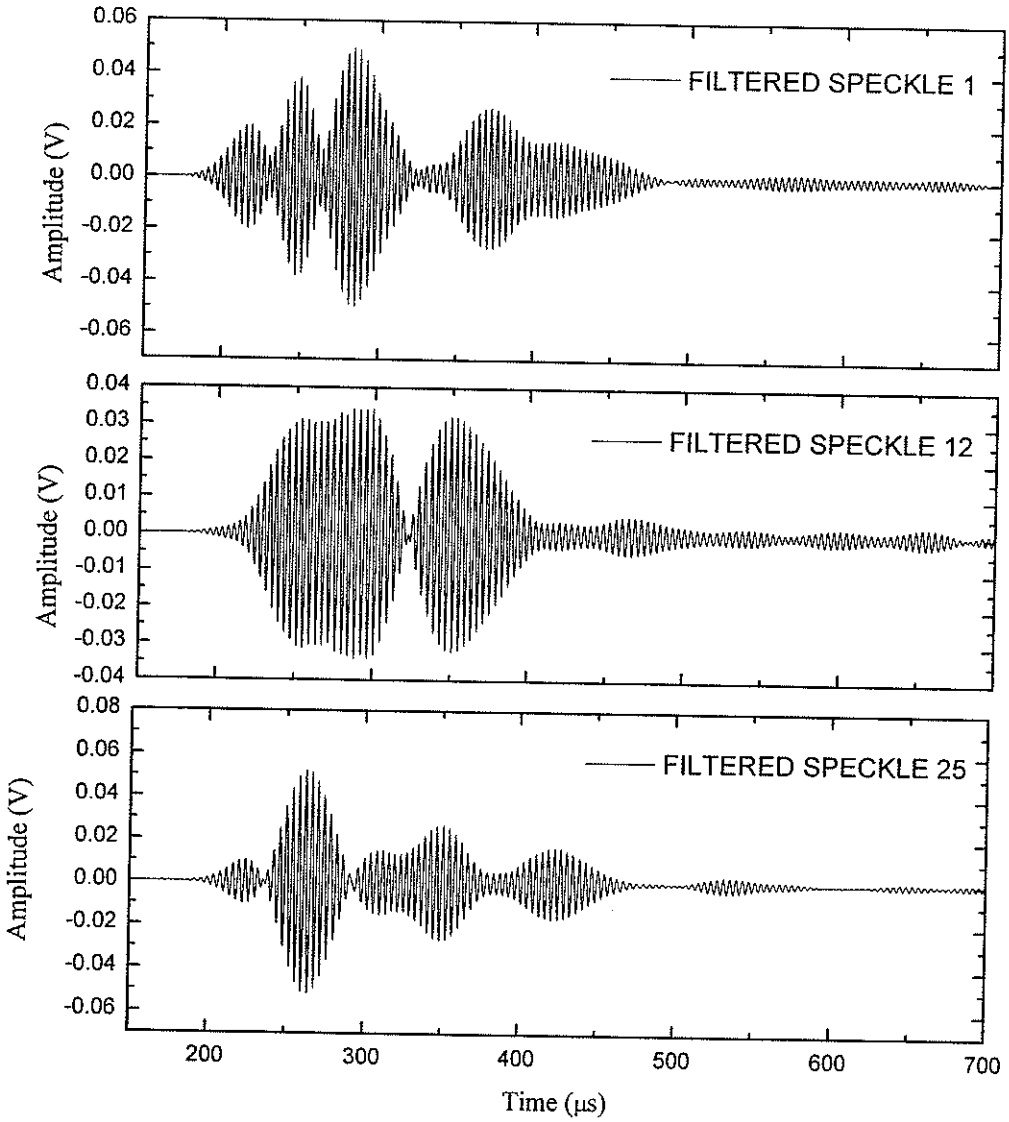

Figure 5. 2. 14 Filtered pulses of three typical transmitted speckles in figure 5.2.13.

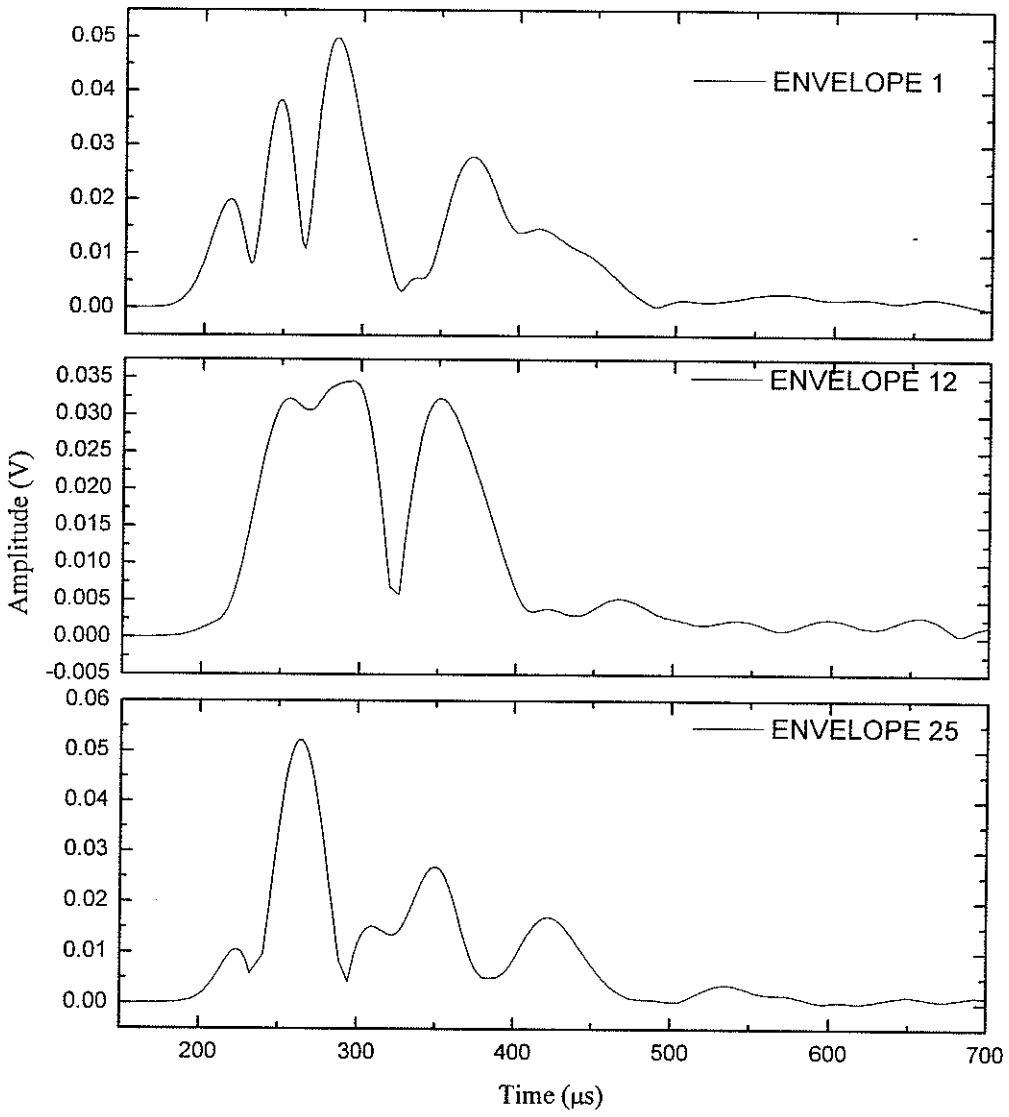

Figure 5. 2. 15 Envelopes of the filtered pulses in figure 5.2.14.

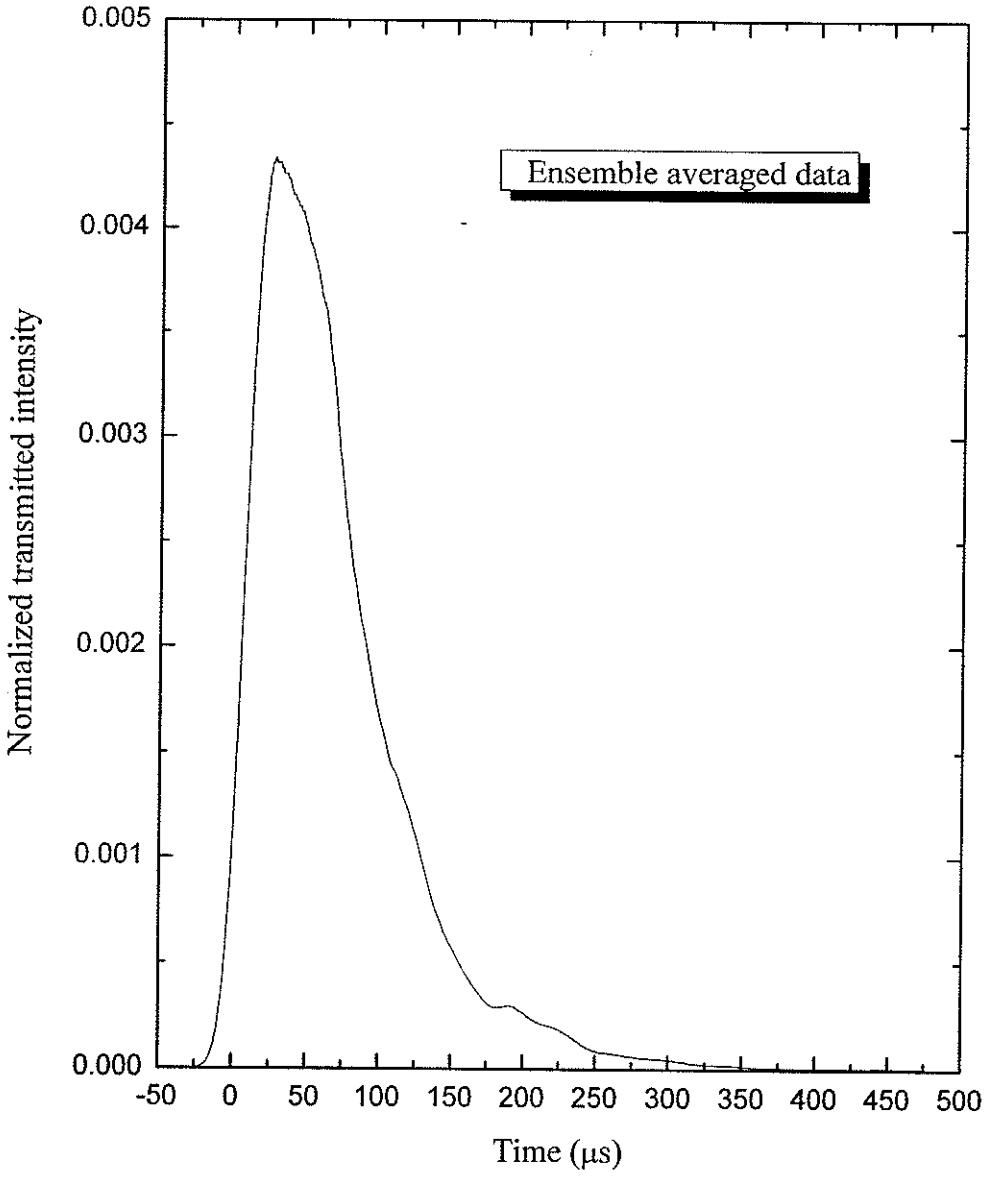

Figure 5. 2. 16 Ensemble averaged diffuse intensity centered at 0.25 MHz with bandwidth of 0.02 MHz .

5.2.4 Fitting the diffusive pulse

5.2.4.1 Introduction

As mentioned in Chapter 2, for a planar wave source, the transmitted flux is described by

$$J(t) = \frac{2De^{-t/\tau_a}}{L^2} \sum_{n=1}^{\infty} A_n e^{-D\beta_n^2 t/L^2} \tag{5-8}$$

A *C* program called con_fit7w was written to fit the diffusive pulse to the expression above. The input parameters that the *C* program needed were:

(1) D: Starting value of the diffusion coefficient

(2) τ_a: Starting value of the absorption time

(3) l^*: The transport mean free path, which was estimated from the weighted average of longitudinal and transverse scattering mean free paths

$$l^* = \frac{\frac{l_{sL}}{v_{p,L}^2} + \frac{2l_{sT}}{v_{p,T}^2}}{\frac{1}{v_{p,L}^2} + \frac{2}{v_{p,T}^2}}, \tag{5-9}$$

where L and T represent longitudinal and transverse, respectively, and v_p is phase velocity.

(4) z_0: The penetration depth into the sample where the source begins to diffuse, which was assumed to be equal to the transport mean free path l^* [Durian, 1994].

(5) L: The thickness of the sample

(6) v_e: the Energy velocity, which was estimated by

$$v_e = \frac{\frac{1}{v_{p,L}^2} + \frac{2}{v_{p,T}^2}}{\frac{1}{v_{p,L}^2 v_{g,L}} + \frac{2}{v_{p,T}^2 v_{g,T}}} \tag{5-10}$$

where p and g represent phase and group velocity, respectively.

(7) R: Angle-averaged reflection coefficient of the diffuse waves. The details of the calculation of R for acoustic wave are summarized by Schriemer (1997). This calculation has been extended to elastic wave by Beck (2000).

(8) An amplitude factor that allows a normalization correction to be made.

The transport mean free path l^*, the penetration depth z_0, the sample thickness L, the energy velocity v_e and the reflection coefficient R were fixed parameters, which were determined numerically, based on ballistic measurements, by using a C program call "crbar.c".

The diffusion coefficient D and absorption time τ_a were the fitting parameters. "crbar.c" provided the estimated diffusion coefficient D based on the expression:

$$D = \frac{1}{3} v_e l^* \tag{5-11}$$

We needed to estimate the initial values of the absorption time τ_a and the normalization factor by guessing. The fitting program calculated a diffusive pulse by using the fixed parameters and estimated parameters. The calculated pulse was then compared to the experimentally determined pulse to see if they were within the given convergence. If

not, the program would adjust the fitting parameters, using a nonlinear least squares minimum procedure, until the given convergence was achieved.

5.2.4.2 Preliminary analysis before fitting

To meet the requirement of the fitting program and make time and amplitude corrections, some preliminary analysis of the reference and diffusive pulses was done. All the analysis could be done on a personal computer rather than a unix/linux machine. In this section, I would like to present the procedure for such analysis.

(1) Filtering.

As mentioned before, to investigate the frequency dependence of the diffusion properties, we needed to filter the pulses with a Gaussian bandpass filter function with a narrow bandwidth. A *C* program "Gauss4alltimes" was applied in this analysis. Usually, ~10% of the transducer frequency was used as the bandwidth, i.e., for 0.25 MHz data, a bandwidth of 0.02 MHz was used.

For the reference pulse, we simply used "Gauss4alltimes" to filtered it to attain required frequency components.

For the diffusive pulse, we made time and amplitude corrections on each individual speckle, as described above, and extracted the ballistic pulse by averaging all of the

corrected speckles, and subtracted the ballistic pulse from each speckle. Then "Gauss4alltimes" was applied to all of the diffusive speckles with the same frequency setting as that of reference pulse.

(2) Envelope

A *C* program "envelope" was used to calculate envelopes of both the filtered reference pulse and the diffusive pulses.

(3) Intensity profile

The intensity profiles of individual diffusive pulses were obtained by squaring the envelopes of them and then averaging the diffuse intensity profiles. This analysis was done by using a *C* program "intdist.c".

The intensity profile of the reference pulse was also required, which was easily created in *Origin* by squaring the envelope of filtered reference pulse.

(4) Time correction

The fitting program required the center of the reference intensity profile to be located at $t = 0$. To do this, we needed to find the time t_{peak} corresponding to the peak of the envelope in *Origin*. Then the time t_{peak} was subtracted from the reference intensity profile in *Origin* or by using the *C* program "subtime.c".

The time correction of the ensemble averaged diffuse intensity required the same peak time correction as the reference pulse and the time correction due to the effect of the thickness of the sample and the walls. Hence, the total time that should be subtracted from the ensemble averaged diffuse intensity profile is expressed by

$$t = t_{peak} - \left(\frac{L_{sample} + 2d_{wall}}{v_{water}} - \frac{2d_{wall}}{v_{wall}} \right) \tag{5-12}$$

(5) Normalization

The fitting program required the normalization of the reference intensity profile. To do this, the numerical value I_{peak} of the reference peak was found and the reference intensity profile was then divided by I_{peak}. To correct the ensemble averaged diffuse intensity, another correction factor due to the difference in the attenuator setting between measurements of reference and diffusive pulses was required in addition to dividing by A_{peak}. The total intensity correction for the ensemble averaged diffuse intensity is expressed by

$$I_{norm} = I_{measured} / \left(I_{peak} \times 10^{\Delta dB/10} \right)$$

where ΔdB is the attenuator difference between reference and diffusive pulses when the data were acquired.

(6) Deleting redundant data points

There should be equal number of data points on both sides of the peak of the reference

intensity profile. Meanwhile, the data points in the reference profile whose absolute values were smaller than 0.01 should be also deleted. To make the fitting program converge quickly, the number of points in the diffusive intensity profile should be around 1000. This elimination of redundant points was done in *Origin*.

After all the procedures above were done, con_fit7w was used to fit the ensemble average diffusive pulse.

5.2.4.3 Plane wave source results

Ensemble averaged diffusive pulses were determined at several frequencies in this frequency regime (0.25 MHz). The incident pulse was Gauss 2 centered at 0.25 MHz. The ensemble averaged diffusive pulses at some certain frequencies (0.2 MHz, 0.25 MHz and 0.3 MHz) for samples 5, 6 and 7 were fitted by the predictions of diffusion theory. The fitting results for sample 5 at each frequency are illustrated in figures 5.2.17, 5.2.18 and 5.2.19. In this frequency regime, the absorption time τ_a determined from the fitting program was infinity, which meant there was no measurable absorption present. The diffusion coefficient D was found to be around 1 mm/μs^2 for all frequencies, which suggested that the diffusion coefficient D was frequency independent in this frequency regime. The values of diffusion coefficient D are shown in table 5.2.1. The diffusion coefficients D for sample 3 and sample 4 are bigger than those for sample 5 and sample 6. These results may suggest that the strength of bonds in sample 3 and sample 4 are

stronger, which was seen from a visual inspection of the size of the necks between the beads in the samples. Stronger bonds are expected to result in larger velocities and mean free paths [Schriemer *et al.*, 1996], and hence larger diffusion coefficients, so that the wave diffuses more rapidly.

D (mm^2/μs)	Sample 3	Sample 4	Sample 5	Sample 6	Sample 7
0.2 MHz	4.6	5.6	2.5	2.0	2.1
0.25 MHz	4.2	5.1	2.3	1.8	1.8
0.3 MHz	4.2	4.3	1.9	1.7	1.7

Table 5.2.1 Diffusion coefficients for different samples.

One thing we should notice is that the values of the diffusion coefficient D in Table 5.2.1 are inconsistent with the relation $D = \frac{1}{3} v_e \times l^*$. This disagreement may be attributed to difficulties in determining the energy velocity v_e, the penetration depth z_0 and reflection coefficient R. The group velocity graph (figure 5.2.9) shows that the group velocities oscillated, which was due to resonant-like standing wave reflections inside the samples. Hence, it was difficult to determine the group velocity. The penetration depth z_0 was taken to be equal to the transport mean free path l^*, which was estimated from the scattering mean free path (5-9), and l^* could be bigger than this estimate. The angle-averaged reflection coefficient could also be bigger when the reflection in the

sample walls was considered. If we adjusted v_e, l^* and R in the fitting procedure, the diffusion coefficient D could be determined that satisfied the relation $D = \frac{1}{3} v_e \times l^*$. Figure 5.2.20 shows the fitting result based on the possible values of v_e and l^* that satisfy $D = \frac{1}{3} v_e \times l^*$. In this fit, the input values v_e = 3 mm/μs and l^* = 1.4 mm were in the reasonable range.

5.2.5 Conclusion

In this section, the method of determining ballistic parameters, and the procedure of analyzing and fitting intensity time profiles were presented. In the diffusive regime, the transmitted intensity shows an exponential decay at long times and the diffusion theory gives a very good description of the data.

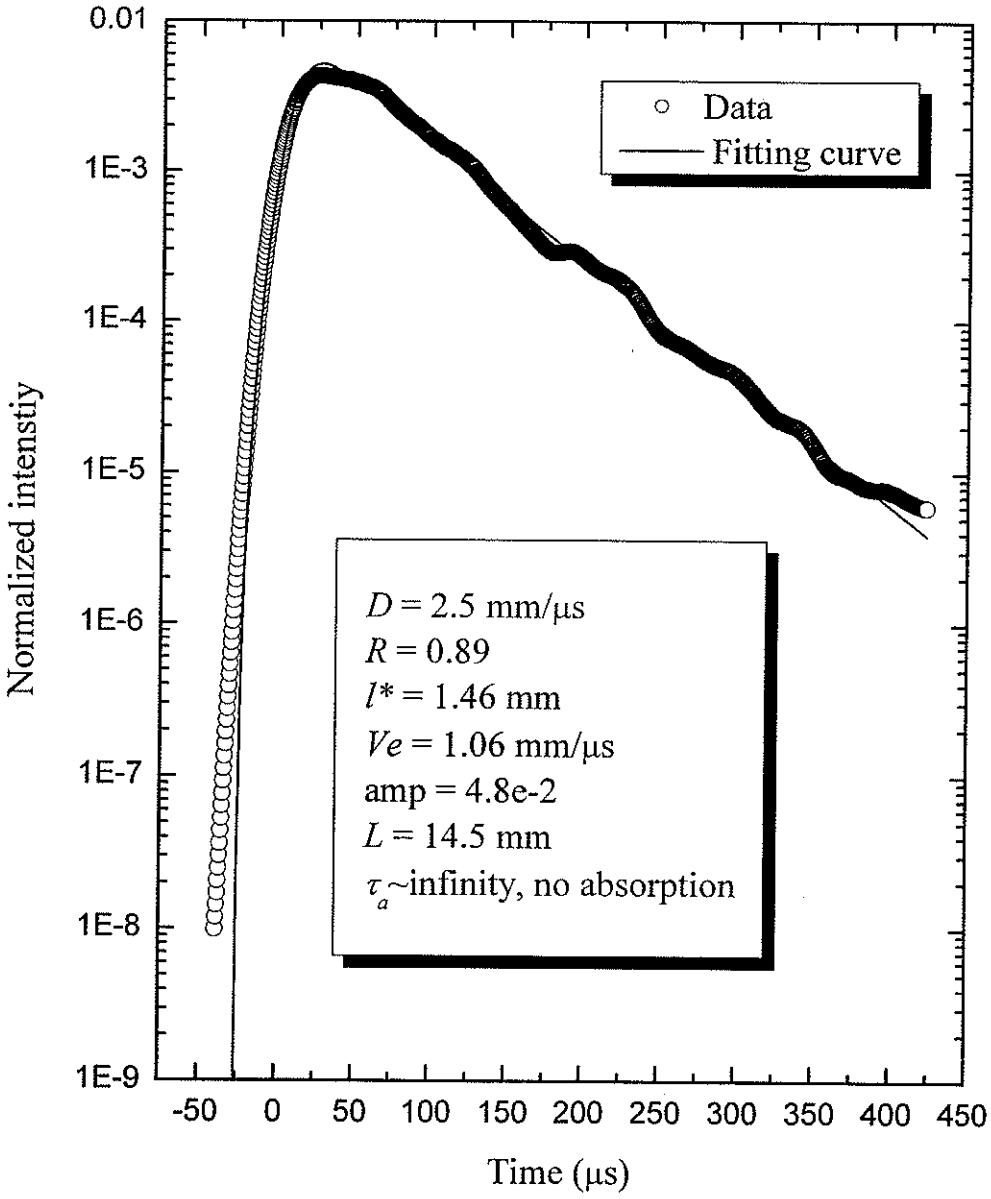

Figure 5. 2. 17 Fitting profile for sample 5 at 0.2 MHz.

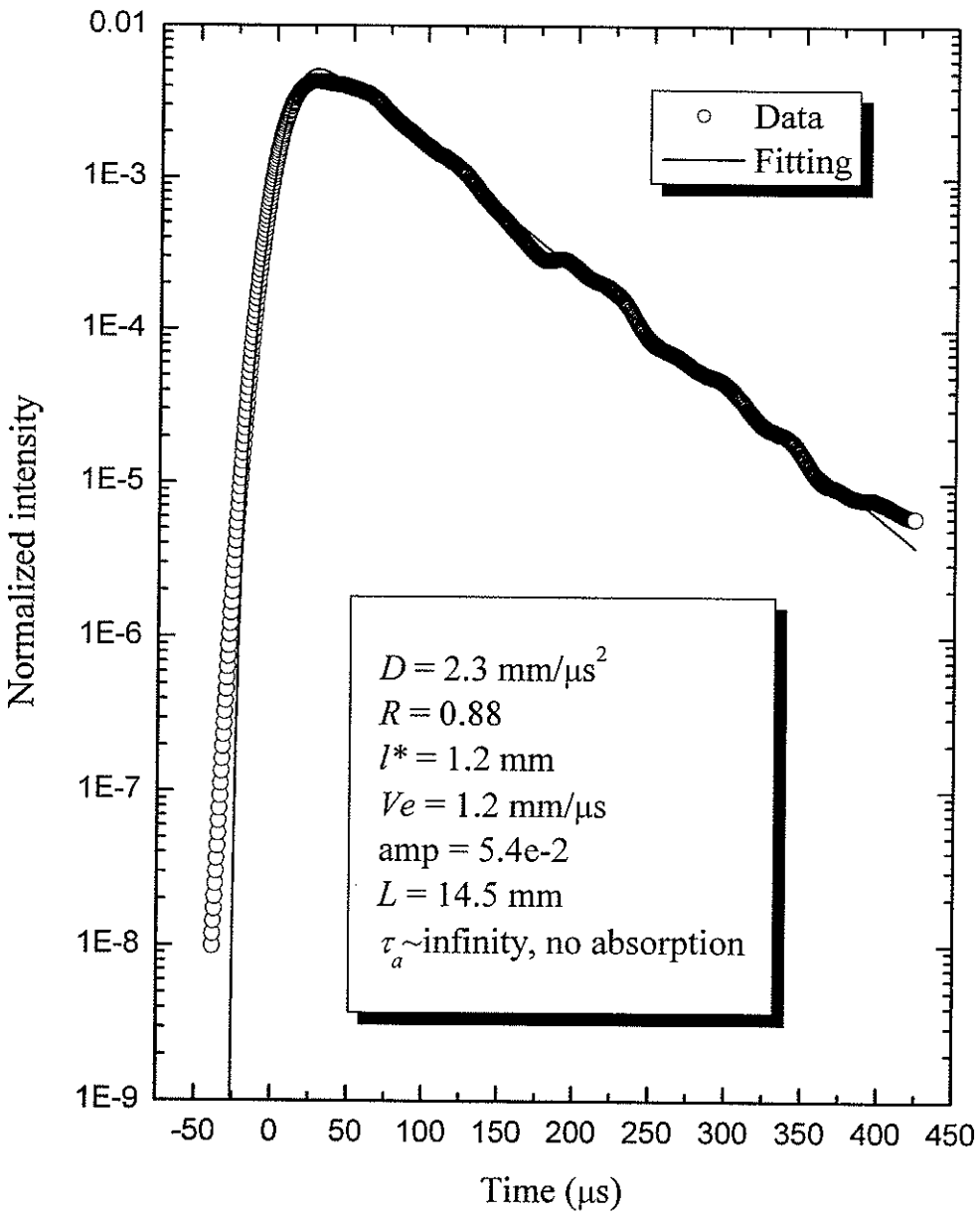

Figure 5. 2. 18 Fitting profile for sample 5 at 0.25 MHz.

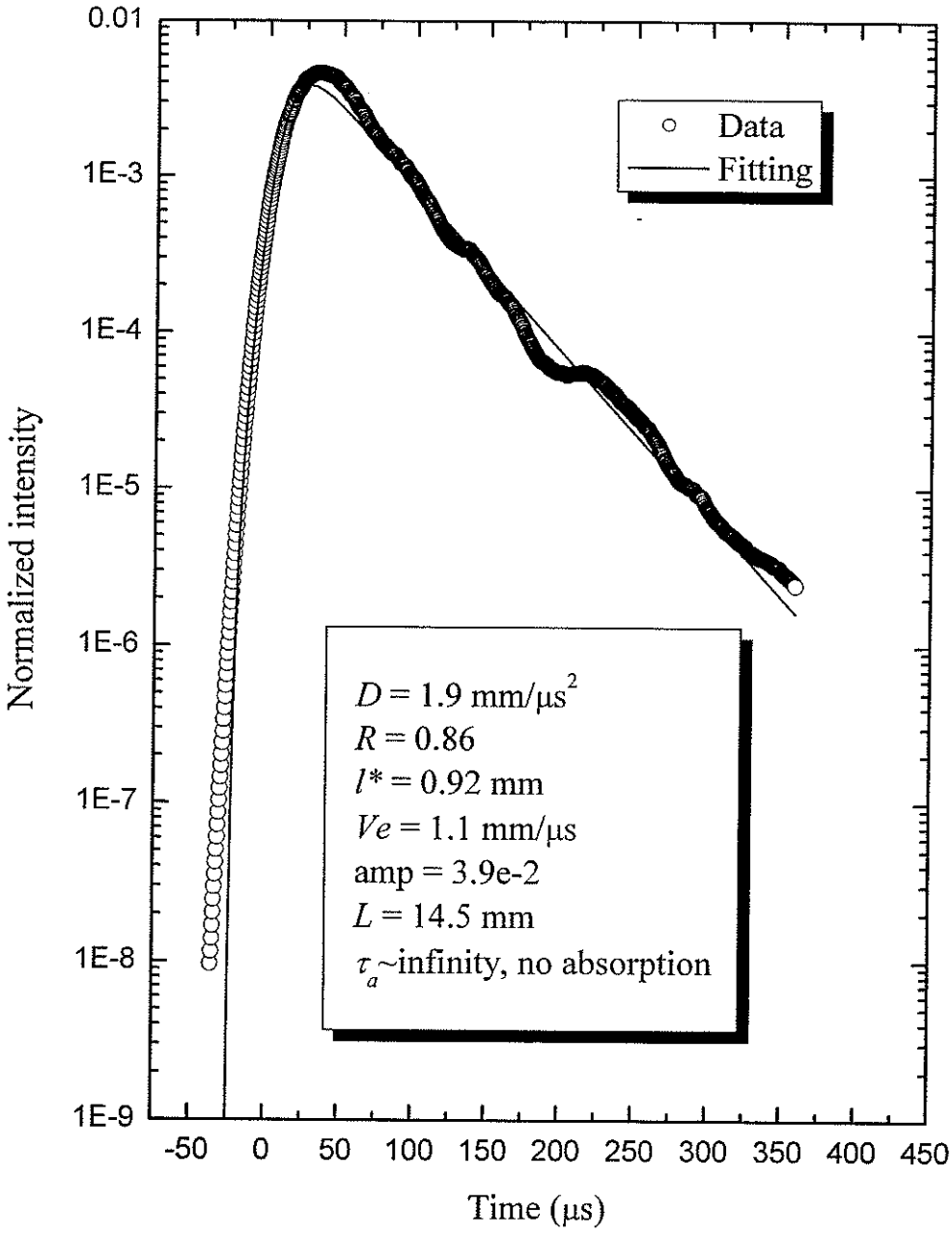

Figure 5. 2. 19 Fitting profile for sample 5 at 0.3 MHz.

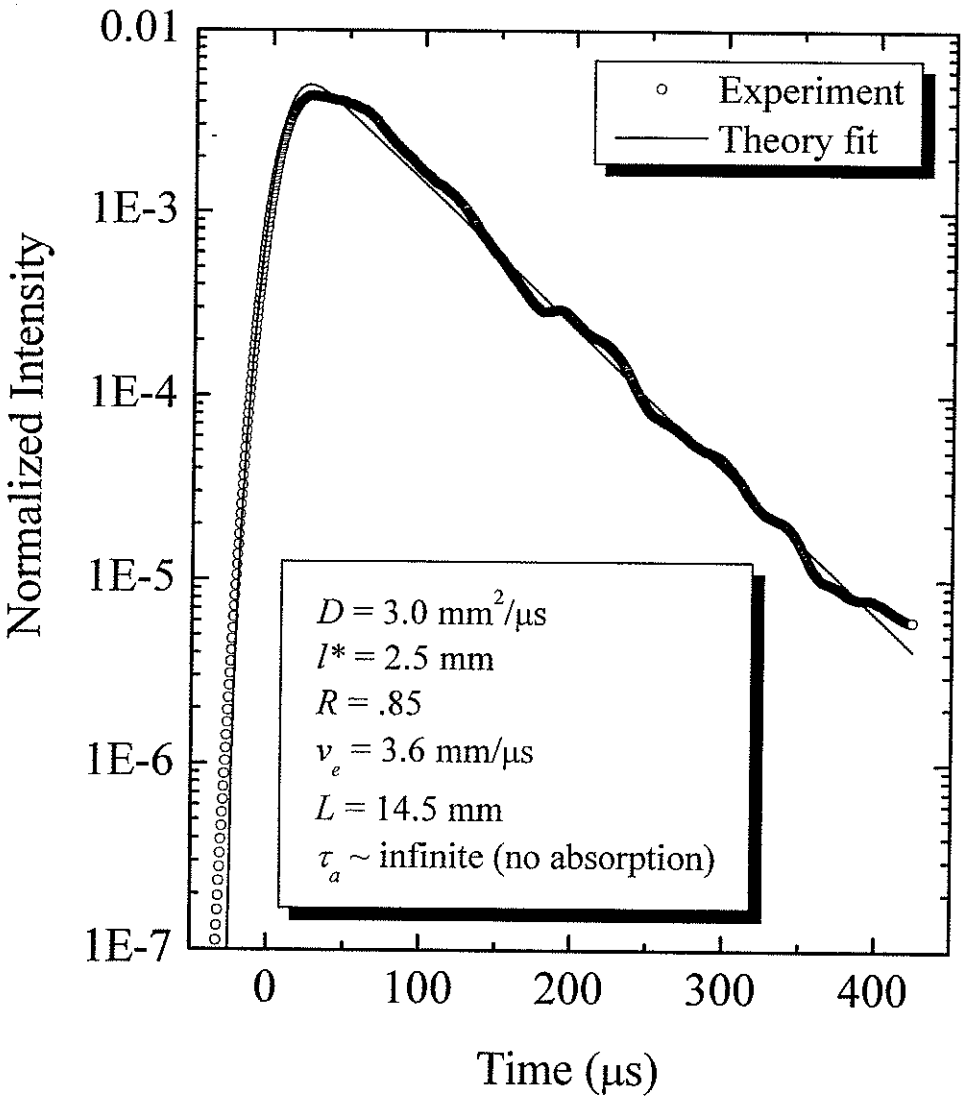

Figure 5. 2. 20 Adjusted fitting for sample 5 at 0.2 MHz.

5.3 Localized regime

5.3.1 Introduction

In the section 5.2, we presented the intensity time profiles of normal diffusive pulses in the lower part of the intermediate frequency range. The time profiles were found to fit the theoretical predictions of the diffusion approximation very well, and had an exponential decay, which indicates that the diffusion coefficient was constant over time. In this section, I will present the results in the upper part of the intermediate frequency range, in which the localization of sound was observed. Two different approaches, both consistent with the theoretical predictions, were applied to demonstrate the localization of sound in this regime. One of the approaches was the observation of a time-dependent diffusion coefficient. In contrast to the exponential tail of the time profile in the diffusive regime, the tail was non-exponential, indicating that the diffusion coefficient was changing over time. The behavior of time-dependent diffusion coefficient was consistent with recent theory predictions for localization. [Skipetrov and Tiggelen, 2006] The other approach was based on measurements of the statistical distribution of the intensity. Rather than the Rayleigh distribution in diffusive regime, the normalized intensity distribution exhibits stretched exponential behavior, which indicates sound localization.

5.3.2 Time-dependent diffusion coefficient

5.3.2.1 Time profile with non-exponential tail

In the upper part of the intermediate frequency regime, a non-exponential tail was observed in the time profile of the ensemble-averaged intensity of the multiply scattered waves. This non-exponential behavior starts at frequencies as low as 1.5 MHz at least and was seen in all samples. Data for all samples are collected in Appendix A. Here I focus on the analysis of data for sample 5. The transmitted intensities in the 2 MHz frequency range were obtained by averaging 3025 speckles to attain smooth results. Figure 5.3.1 shows the transmitted intensity for sample 5 at frequencies of 1.8 MHz, 2 MHz, 2.2 MHz, 2.4 MHz, 2.6 MHz and 2.8 MHz with a 0.2 MHz bandwidth. The solid line shows exponential decay for comparison. A clear departure from exponential decay was found at long times, an effect that cannot be explained by normal diffusion. To make sure that this departure was not due to noise, the noise background before diffusion started was subtracted from the transmitted intensity before further analysis. The dashed line in figure 5.3.2 shows the noise level (2.34×10^{-7}), and the dotted curve shows the transmitted intensity after noise subtraction. To calculate the diffusion coefficient, the derivative of $\ln(I(t))$ should first be taken for every transmission profile, according to equation (2-13). However, the little bumps in the transmission profiles lead to a very noisy signal when the derivative is taken. We found that the intensity transmission profiles of three high frequencies (2.4 MHz, 2.6 MHz and 2.8 MHz) had similar behavior. To improve the signal-to-noise ratio, the average of the transmission

profiles was taken for these three frequencies.

Before further analysis was performed, we tried to use diffusion theory to fit the early time behavior of the high frequency averaged time profile (2.4 – 2.8 MHz), including only the rise and initial exponential decay. Since the transmitted field in this regime was dominated by scattered sound, the ballistic pulse was difficult to determine, so that we could not use independent measurements of the mean free path and phase velocity to estimate l^* and R. Hence, we varied all the fitting parameters to find the best fit, shown by the solid curve in figure 5.3.3; this curve gives a nearly perfect fit to the early time part of the intensity profile. The parameters for the fitted curve are shown in the text panel in figure 5.3.3. The diffusion coefficient was 2.7 $mm^2/\mu s$ and the absorption time τ_a was 83 μs. Apparently, absorption became large enough to measure in this frequency range. Then the intensity transmission profile was corrected by multiplying it by $\exp(t/\tau_a)$ to eliminate the effect of absorption. The hollow circle symbols in the figure 5.3.3 show the modified time profile with no absorption; these corrected data were found to satisfy the power law, shown by the dashed curve in figure 5.3.3, $I(t) \propto t^{-(1+s)}$ with s ~ 0.85. This behavior is in sharp contrast to the exponential decay in the diffuse regime. This observation of power law decay suggests the localization of sound. [Skipetrov and Tiggelen, 2006]

To directly investigate the behavior of the diffusion coefficient, the logarithm of this

average profile in figure 5.3.3 was taken and is shown by the hollow circles in the upper panel of figure 5.3.4. Before taking the derivative of $\ln(I(t))$, the $\ln(I(t))$ data still needed further smoothing, which was done in origin by averaging 200 adjacent data points, yielding the solid curve in the upper panel of figure 5.3.4. The derivative of $[-\ln(I(t))]$ is shown as hollow circle symbols in the lower panel of figure 5.3.4. A fit of a constant plus a function that is proportional to $1/t$ is shown by the solid curve. This fit to the tail of the derivative (for $t > 150$ μs, i.e. $t >> \tau_D$) gave $1.81/t+1/83.4$.

The theory prediction (2-13) gives $-\frac{d}{dt}(\ln I(t)) = \frac{D(t)}{[(L+2z_0)^2/\pi^2]} + \frac{1}{\tau_a}$. However, this expression used an approximate solution, which is valid only when l^*/L and R are small. This condition is not true for our case, so we need to use the exact solution instead of the approximate solution. From equation (2-11) we obtain

$$-\frac{d}{dt}(\ln I(t)) = \sum_{n=1}^{\infty}[\frac{\beta_n^2}{L^2}D(t) + \frac{1}{\tau_a}] \qquad (5\text{-}8)$$

Since β_1 is dominant at long times, equation (5-8) can be approximated as

$$-\frac{d}{dt}(\ln I(t)) = \frac{\beta_1^2}{L^2}D(t) + \frac{1}{\tau_a} \qquad (5\text{-}9)$$

By comparing this expression to the fitted expression $1.81/t+1/83.4$, the absorption time τ_a of 83.4 μs can be determined, which is consistent with the fitting parameter τ_a = 83 μs given by the diffusion theory. Meanwhile, the result $\frac{\beta_1^2}{L^2}D(t) = 1.81/t$ can

be derived. Hence, $D(t)$ is expressed as $D(t) = \frac{1.81L^2}{\beta_1^2 t}$. The value of β_1 is given by the lowest positive zeros of the transcendental equation (2-3), which was calculated to be 1.054 by using Maple. Therefore, $D(t) = 340/t$, which is plotted in figure 5.3.5, along with the scaled experimental data, $-\frac{L^2}{\beta_1^2}\frac{d}{dt}(\ln I(t)) - \frac{1}{\tau_a}$.

The same analysis was done for lower frequency averaged time profiles as well. The fitted result is presented in figure 5.3.6, giving $D = 2.6$ mm^2/μs and $\tau_a = 110$ μs. β_1 for this setting was calculated to be 1.33. Hence, the time-dependent $D(t)$ was expressed as $260/t$. The other relevant results are presented in figures 5.3.7 and 5.3.8.

This time-dependent diffusion clearly indicates that the localized regime has been reached. However, there is still some uncertainty in the magnitude of $D(t)$, since this depends on β_1, which is depends on the fitting parameters l^* and R, although $D(t)$ clearly decays as $1/t$. In the next section, I will describe ratio measurements by which the additional information on time-dependent diffusion coefficient can be measured independent of all other parameters in the model for $I(t)$.

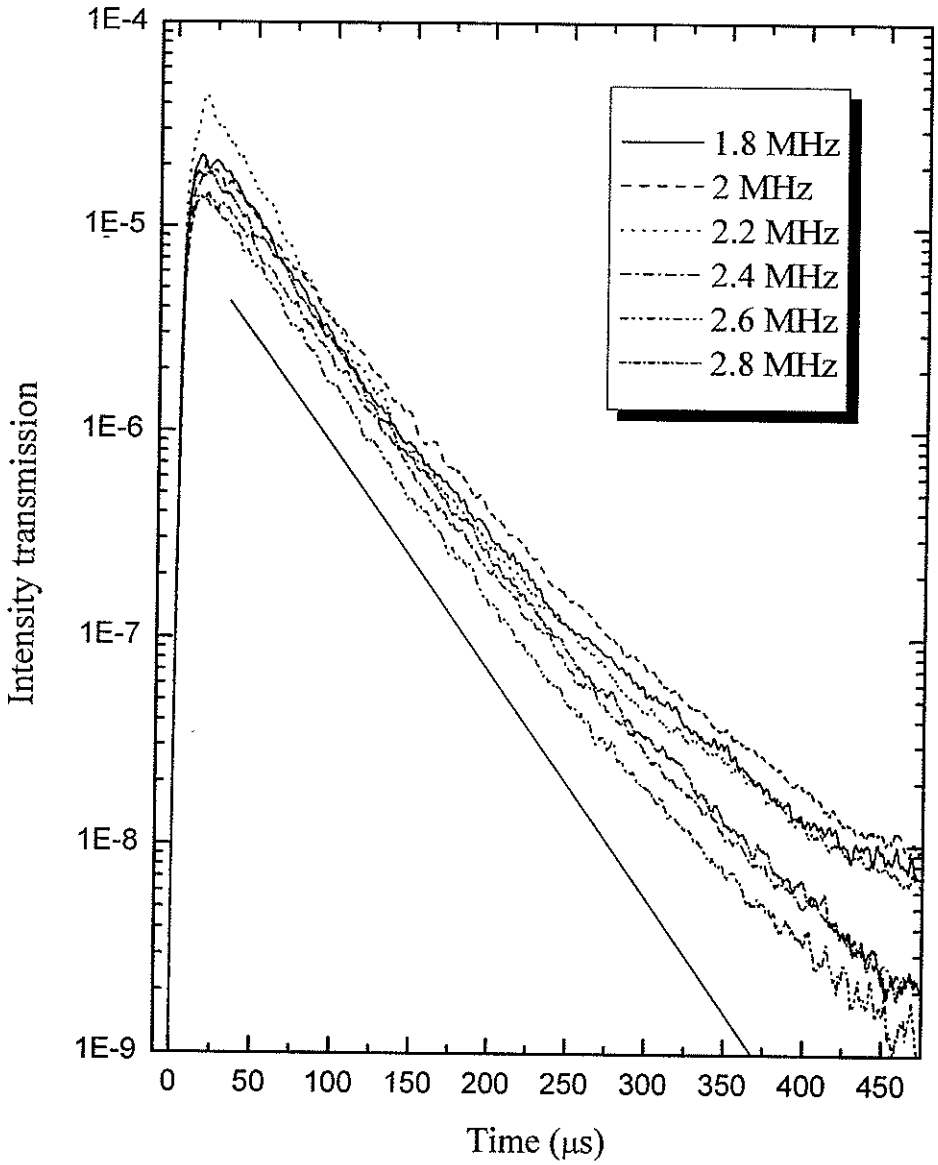

Figure 5. 3. 1 Intensity transmission for different frequency components. The solid line shows the exponential decay for comparison.

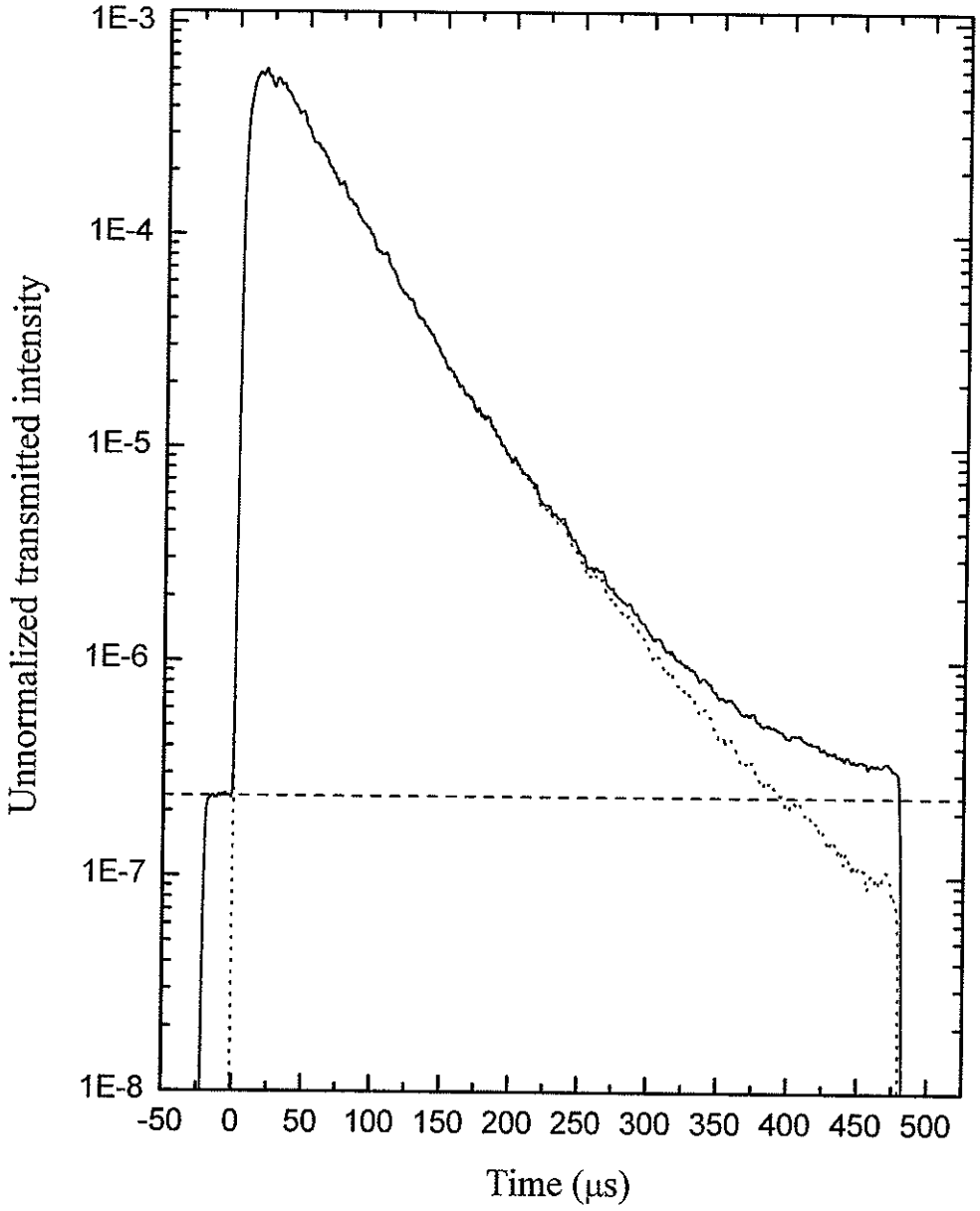

Figure 5. 3. 2 The solid curve shows the transmitted intensity with noise background. The dashed line shows the noise level. The dotted curve shows the transmitted intensity after noise subtraction.

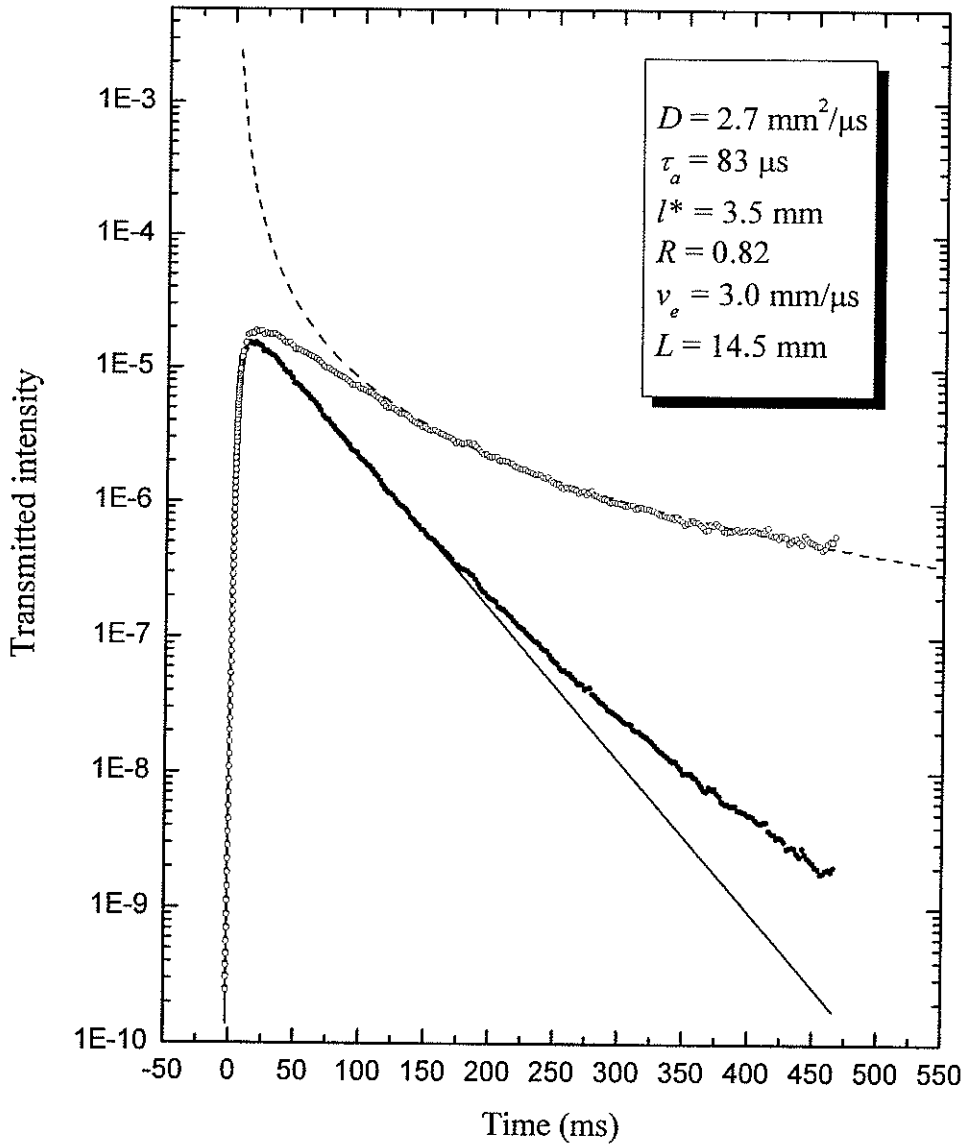

Figure 5. 3. 3 Solid circles: Transmitted intensity averaged over frequencies of 2.4 MHz, 2.6 MHz and 2.8 MHz. Solid curve: fit of the solution of the diffusion equation to the early time behavior. Hollow circles: Transmitted intensity corrected by eliminating absorption. Dashed curve: Power law fit to the intensity transmission at long times (see text).

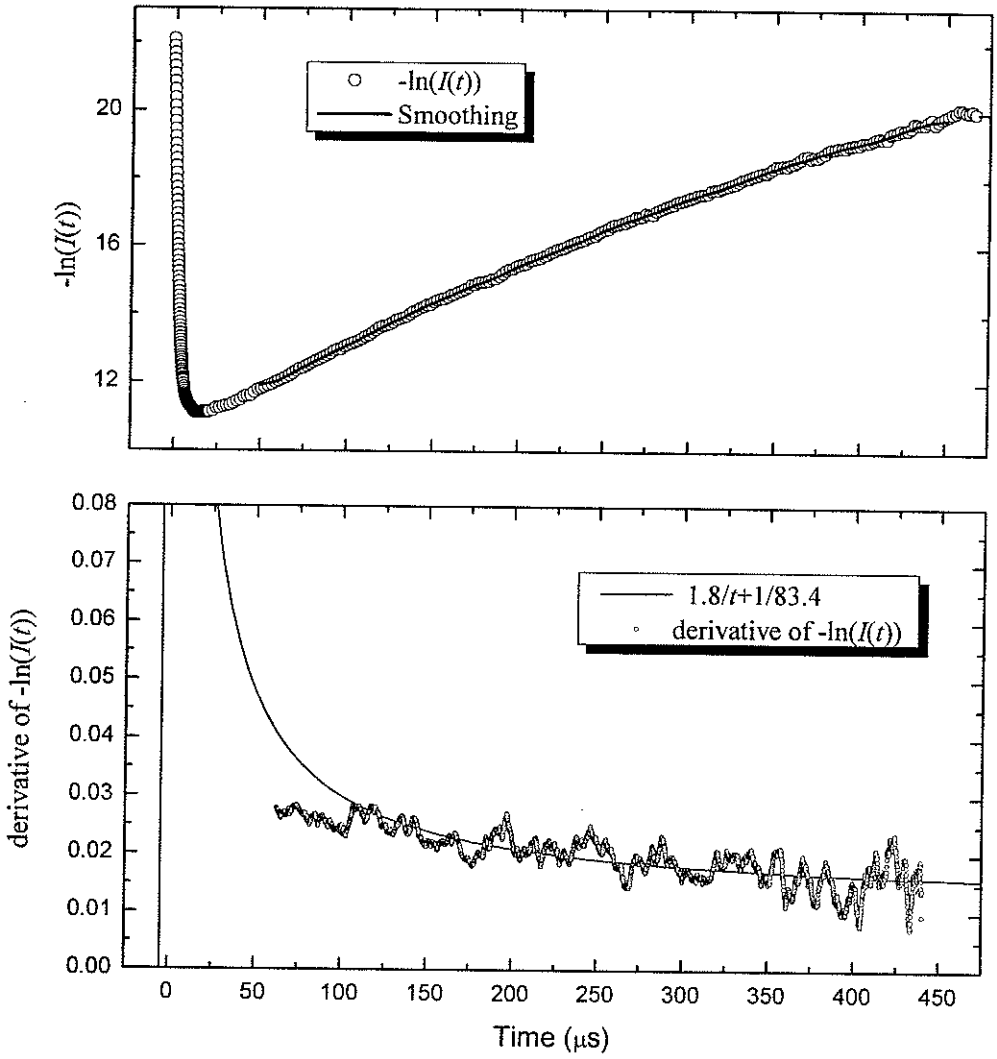

Figure 5. 3. 4 Upper panel: The hollow circles show the logarithm of the transmitted intensity and the solid curve is the smoothed result for $\ln(I(t))$. Lower panel: The hollow circle symbol shows the derivative of $\ln(I(t))$ and the solid curve is the theoretical fit to the data.

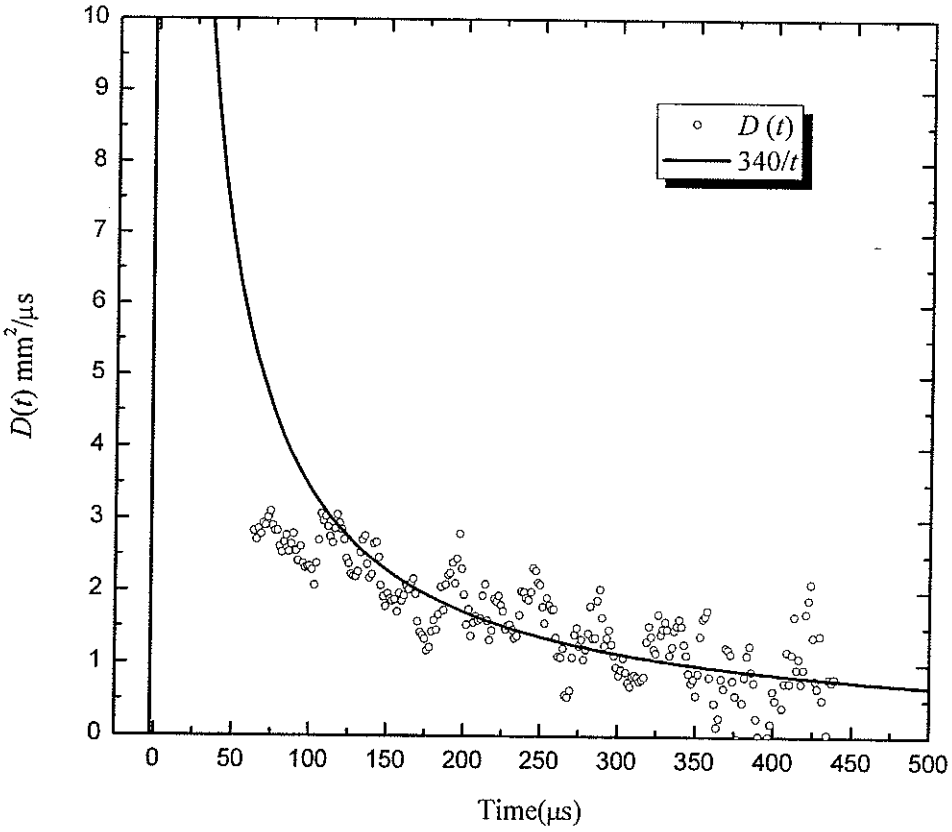

Figure 5. 3. 5 Time-dependent diffusion coefficient: $D(t) = 340/t$.

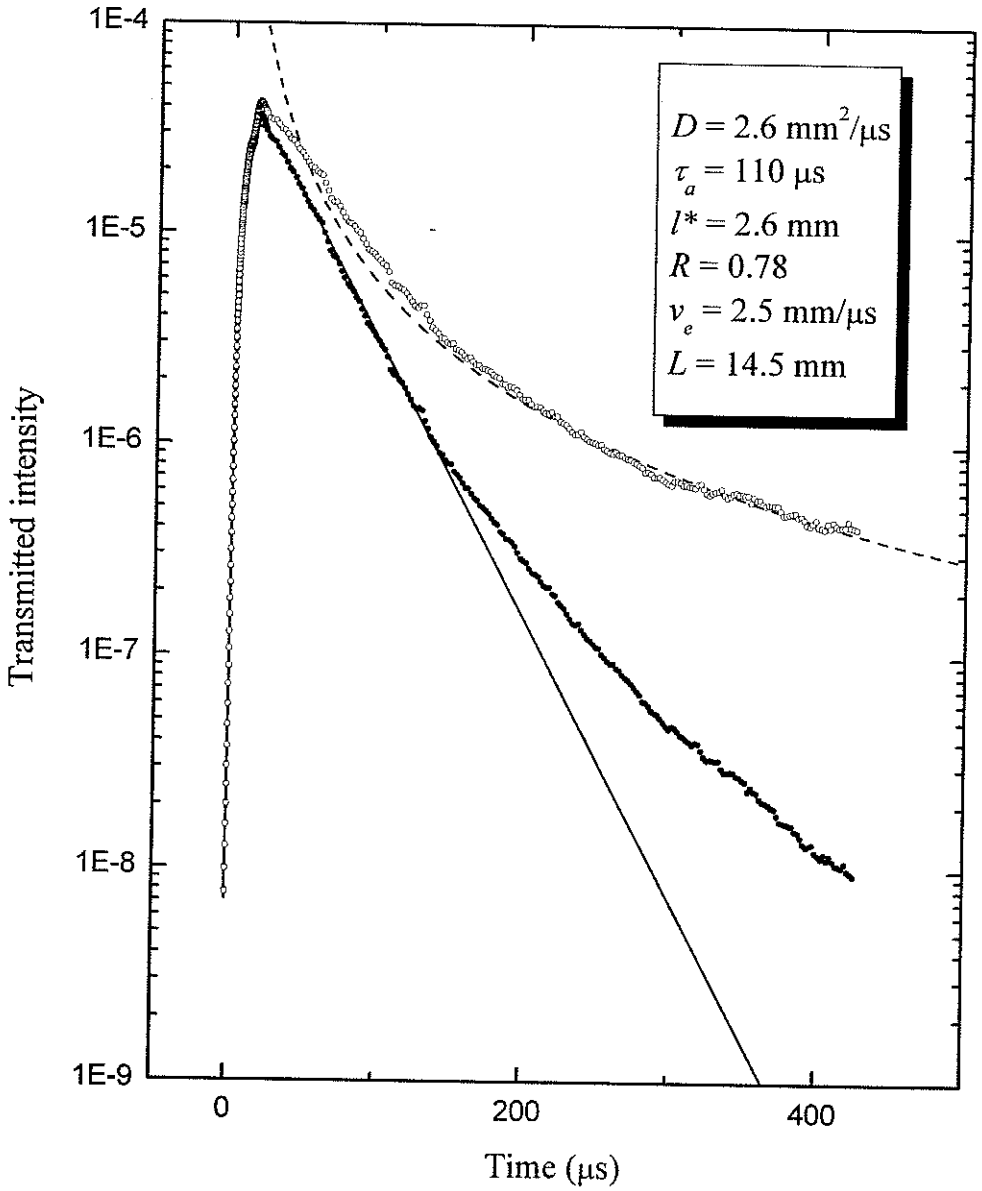

Figure 5. 3. 6 Solid circles: Transmitted intensity averaged over frequencies of 1.8.4 MHz, 2 MHz and 2.2 MHz. Solid curve: fit of the solution of the diffusion equation to the early time behavior. Hollow circles: Transmitted intensity corrected by eliminating absorption. Dashed curve: Power law fit to the intensity transmission at long times. (see text)

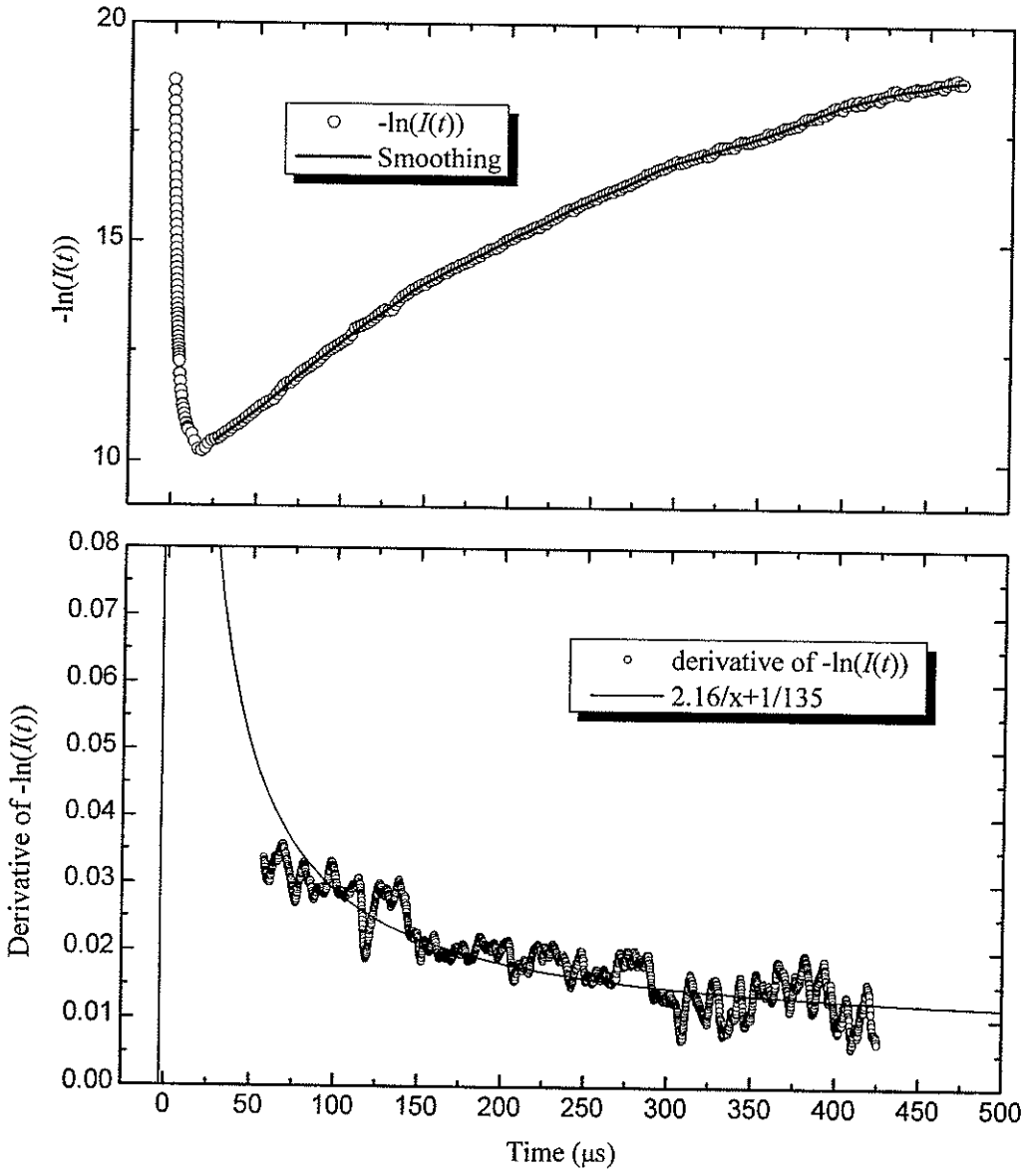

Figure 5. 3. 7 Upper panel: The hollow circles show the logarithm of the transmitted intensity and the solid curve is the smoothed result for $\ln(I(t))$. Lower panel: The hollow circles show the derivative of $\ln(I(t))$ and the solid curve is the theoretical fit to the data.

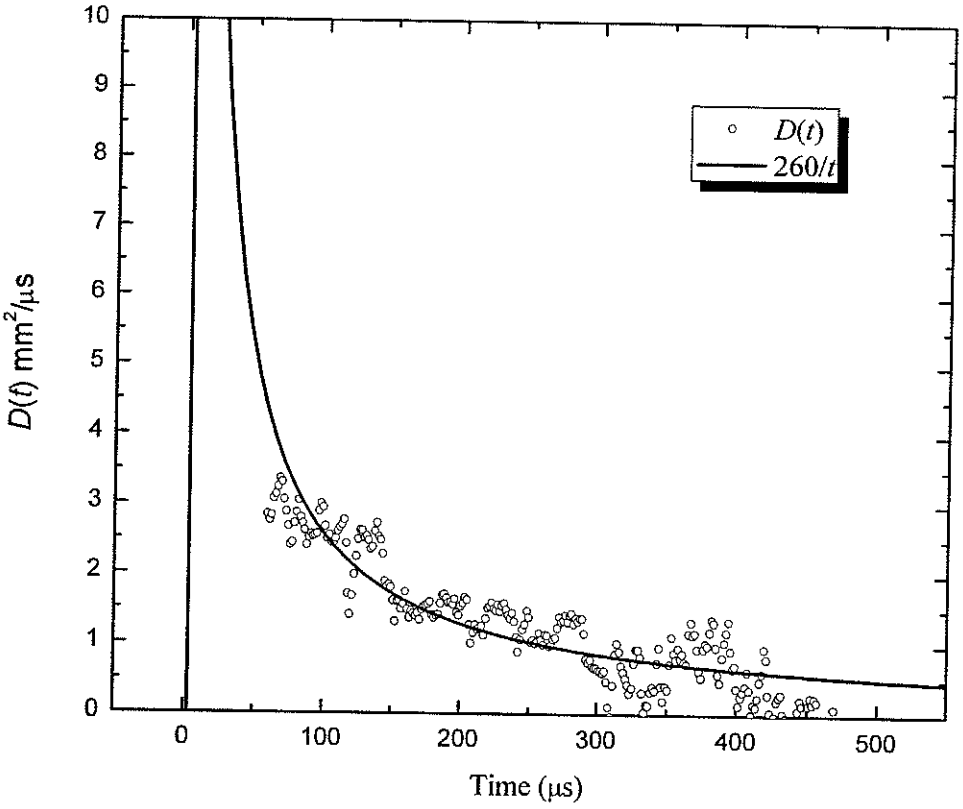

Figure 5. 3. 8 Time-dependent diffusion coefficient: $D(t) = 260/t$.

5.3.2 Ratio measurements

5.3.2.1 The displaced point source technique

To circumvent the uncertainty in the parameters other than $D(t)$ that determine $I(t)$, we first applied the displaced point source technique. The experiment procedure was described in section 4.4.2.2, where it was shown that the expression for the time-dependent diffusion coefficient $D(t)$ is

$$D(t) = \frac{d}{dt}\left(\frac{-[(x_{off} - x_{on})^2 + (y_{off} - y_{on})^2]}{4 \ln I_{ratio}}\right) \tag{5-10}$$

The displacement between the on- and off-axis positions of the hydrophone in our experiment was 20 mm. This expression for $D(t)$ is independent of absorption and boundary effects. Again, to reduce the uncertainty in the data, we averaged the transmitted intensity over a band of frequencies that had similar behavior. The average was taken of 2.4 MHz, 2.6 MHz, 2.8 MHz, 3 MHz and 3.2 MHz intensity transmission profiles for both on- and off-axis measurements, as shown in the upper panel of figure 5.3.9. Since the input beam was not an ideal point source, a correction for this was needed before performing the next step in the analysis. The cross section of the input beam was approximated by a Gaussian profile, as shown in figure 5.3.10. The solid curve in figure 5.3.10 is the Gaussian fit to the input beam profile, which gave a width $\sigma = 2.29$ mm. Then, the point source transmitted flux was corrected by convolving the point source transmitted flux with the Gaussian input beam profile. Since the input beam profile was symmetric in x and y directions, and only the integral in x direction was

considered:

$$J_{corrected}(t) = \int_{-\infty}^{\infty} J(t) e^{-x^2/2\sigma^2} dx = \left(\int_{-\infty}^{\infty} e^{-r^2/4\int_0^t D(t')dt'} e^{-x^2/2\sigma^2} dx \right) \frac{e^{-t/\tau_a} \sum_{n=1}^{\infty} A_n e^{-D_B \beta_n^2 t / L^2}}{2L^2 t}$$

$$= \frac{2\sqrt{\pi} e^{-x_o^2 \Big/ 2\left(\sigma^2 + 2\int_0^t D(t')dt'\right)}}{\sqrt{\left(\sigma^2 + 2\int_0^t D(t')dt'\right) \Big/ \left(\sigma^2 \int_0^t D(t')dt'\right)}} \frac{e^{-t/\tau_a} \sum_{n=1}^{\infty} A_n e^{-D_B \beta_n^2 t} / L^2}{2L^2 t} \quad (5\text{-}11)$$

x_0 was 0 and 20 mm for on- and off-axis geometry respectively. Then, the ratio of off-axis intensity to on-axis intensity is given by

$$I_{ratio}(t) = e^{\frac{-x_o^2}{2\left(\sigma^2 + 2\int_0^t D(t')dt'\right)}}$$

Hence,

$$\int_0^t D(t')dt' = -\frac{x_o^2}{4\ln(I_{ratio}(t))} - \frac{\sigma^2}{2}$$

Therefore,

$$D(t) = \frac{d}{dt}\left[-\frac{x_o^2}{4\ln(I_{ratio}(t))} - \frac{\sigma^2}{2} \right]$$

Because of noise, further smoothing of $\int_0^t D(t')dt'$ was needed before taking the derivative, which was done in Origin by averaging 500 adjacent points. $\int_0^t D(t')dt'$ is shown by the hollow circle symbols in the middle panel in figure 5.3.9 and the smoothing of $\int_0^t D(t')dt'$ is illustrated by the solid curve in the middle panel in figure 5.3.9. After

taking the derivative of $\int_0^t D(t')dt'$, the diffusion coefficient thus obtained is illustrated by the hollow circles in the lower panel in figure 5.3.9. The diffusion coefficient was fitted to the theoretical prediction that $D \propto 1/t$ at long times. The result of this fit is shown by the solid curve, giving D(t) = 6.6/*t*, which also proved that the diffusion coefficient was decreasing as 1/*t*.

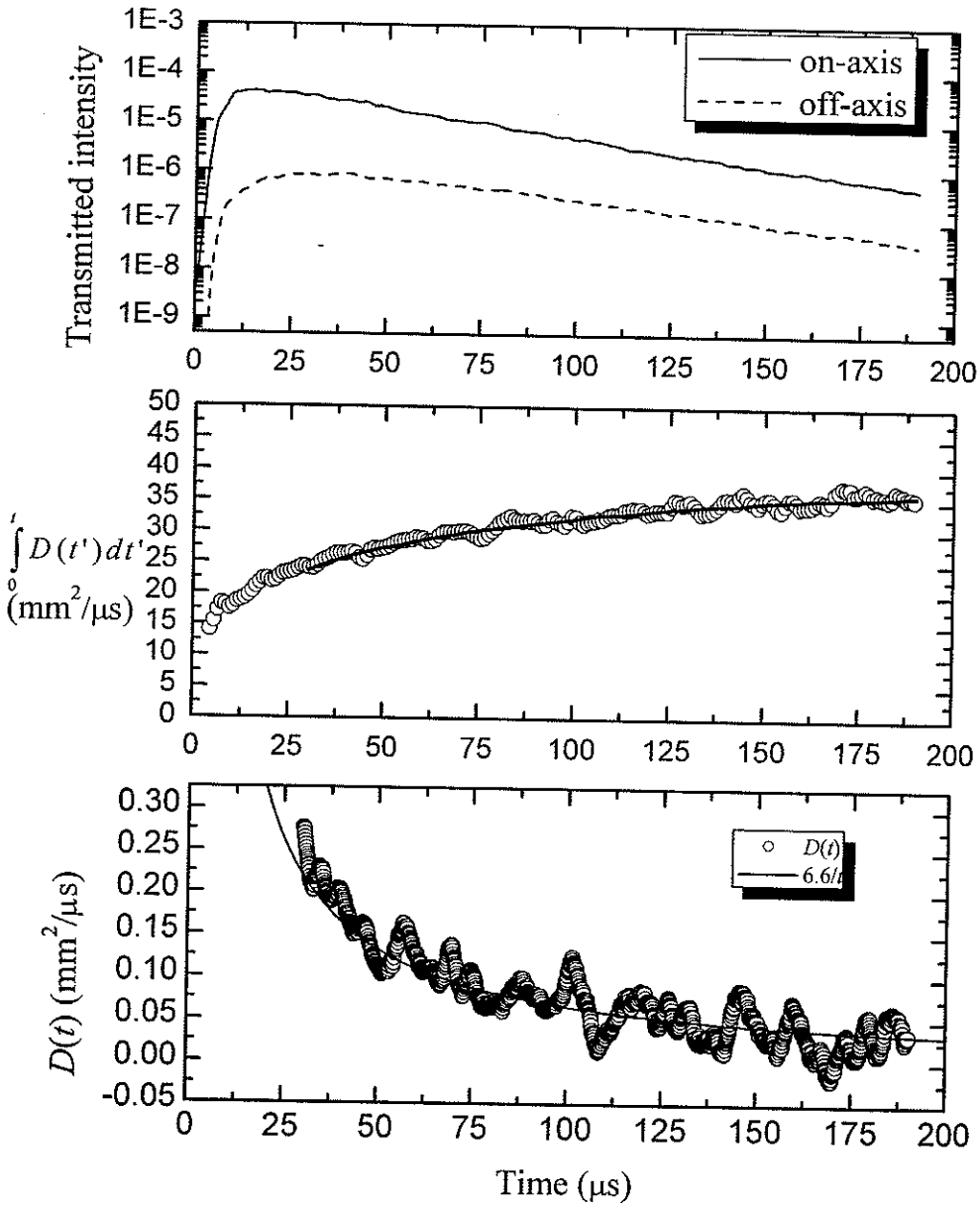

Figure 5. 3. 9 Upper panel: The solid and dashed curves show the on- and off-axis intensity transmission, respectively. Middle panel: The hollow circles show $\int_0^t D(t')dt'$ and the solid curve is the smoothed result. Lower panel: The hollow circles show the time-dependent diffusion coefficient $D(t)$ and the solid curve is the fitted theoretical curve for $D(t)$.

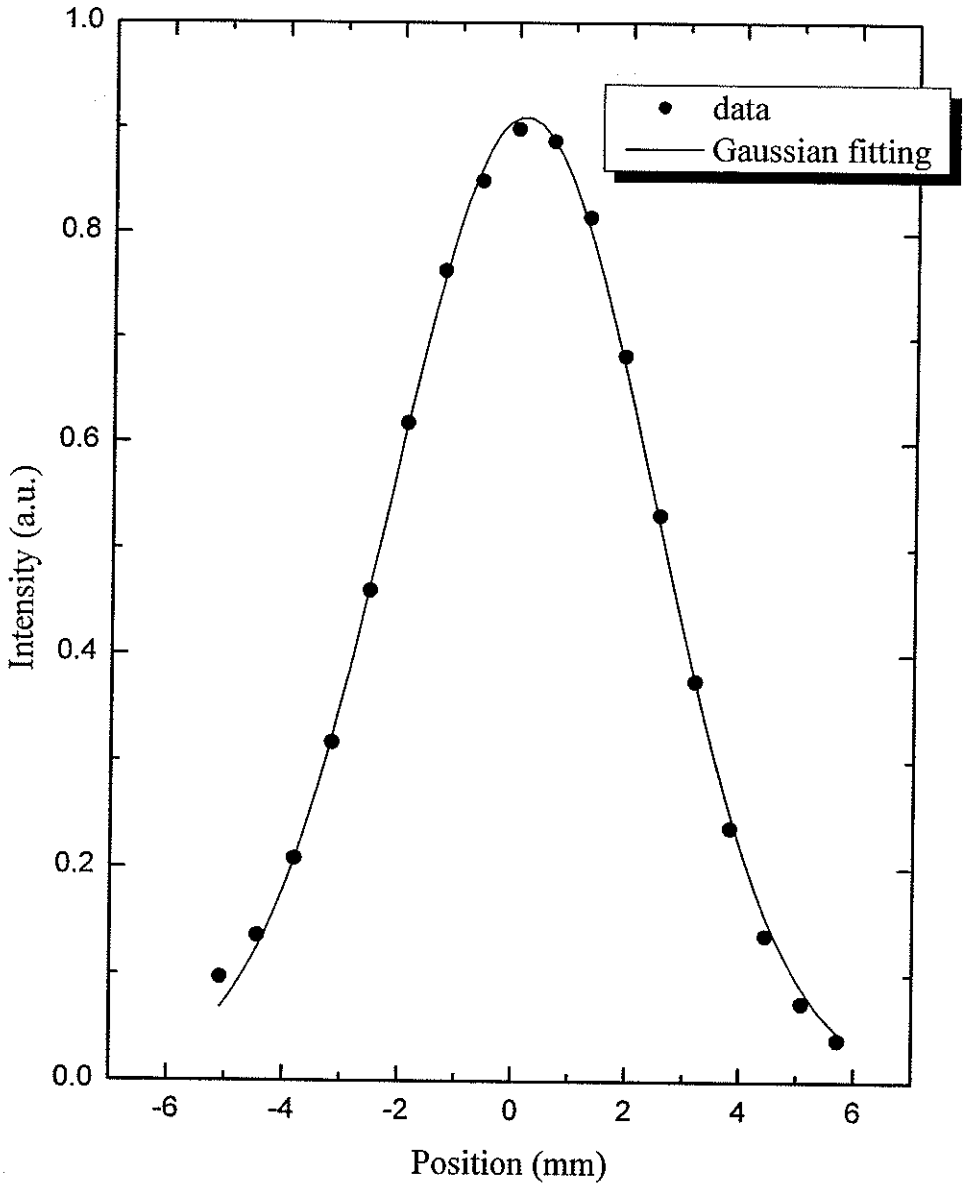

Figure 5. 3. 10 The cross section of input beam profile of the focusing 2.25 MHz transducer, for which the focusing length is 6 inches (150 mm).

5.3.2.2 Ratio of plane wave measurements to point source measurements

In addition to the displaced point source technique, the ratio of the plane wave measurement of $I(t)$ to the point source measurement can also be applied to cancel out all parameters other than D and to check the displaced point source technique result. The same frequency range of data as that analyzed for the displaced point source technique was used. After correcting for the finite widths of the input beam of the quasi-plane wave source and the point source, and taking the ratio of their intensities, we get:

$$I_{ratio} = \frac{I_{plane}}{I_{point}} = \frac{1 + \dfrac{2\int_0^t D(t')dt'}{\sigma_{point}^2}}{1 + \dfrac{2\int_0^t D(t')dt'}{\sigma_{plane}^2}} \tag{5-12}$$

Hence,

$$\int_0^t D(t')dt' = \frac{\sigma_{point}^2}{2} \frac{(I_{ratio} - 1)}{1 - I_{ratio}(\dfrac{\sigma_{point}}{\sigma_{plane}})^2} \tag{5-13}$$

Therefore,

$$D(t) = \frac{d}{dt}\left[\frac{\sigma_{point}^2}{2} \frac{(I_{ratio} - 1)}{1 - I_{ratio}(\dfrac{\sigma_{point}}{\sigma_{plane}})^2} \right] \tag{5-14}$$

Before taking the derivative, we again smoothed $\int_0^t D(t')dt'$, shown by hollow circles in the upper panel in figure 5.3.11, by averaging over 500 adjacent points, giving the solid curve in the upper panel in figure 5.3.11. After taking the derivative, $D(t)$ was obtained,

as shown in the lower panel in figure 5.3.11. The fitting of $D(t)$ at long times gave $4.0/t$, also showing that the diffusion coefficient decreased with time as $1/t$, although the value found for $D(t)$ was smaller than that found by the displaced point source technique.

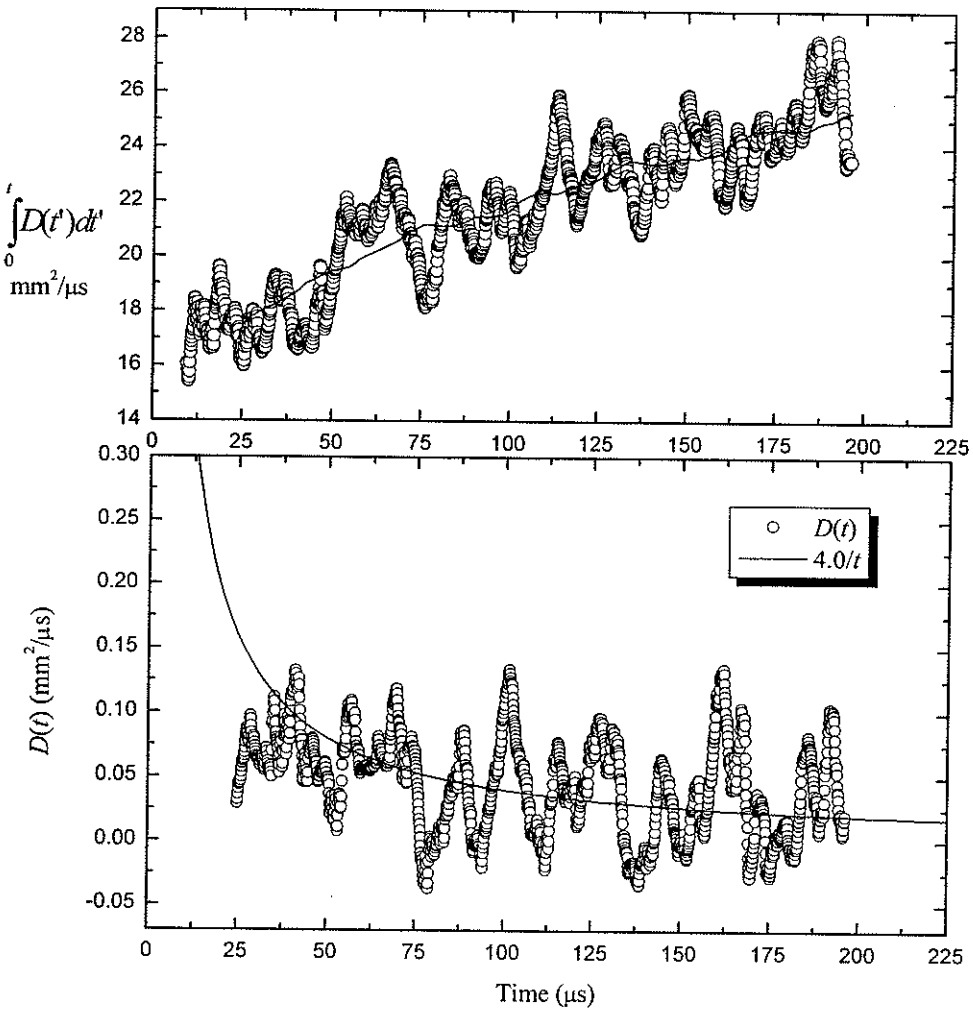

Figure 5. 3. 11 Upper panel: The hollow circles show $\int_0^t D(t')dt'$ and the solid curve is the smoothed result. Lower panel: The hollow circles show the time-dependent diffusion coefficient $D(t)$ and the solid curve is the fit of the theoretical prediction.

5.3.2.3 Discussion

From both of the direct time profile analysis and ratio measurement analysis, we found the diffusion coefficient is time dependent and decays as $1/t$ at long times. However, the value of $D(t)$ found from the ratio measurements was much smaller than that from the time profile measurement. This difference suggests that the localization in the transverse direction is much stronger than the localization in longitudinal direction. This result may be taken as experimental evidence that the diffusion coefficient is a function of both position and time in the localized regime, as proposed in a recent theoretical model for the dynamics of localization in open 3D media. [Skipetrov and Tiggelen, 2006]

5.3.3 Statistical approach

5.3.3.1 Probability distribution of normalized intensity

As described in Chapter 2, in the diffuse regime, the probability distribution of the normalized intensity is described by the Rayleigh distribution as [e.g., see Chabanov *et al.*, 2000]

$$P\left(\frac{I_{ab}}{\langle I_{ab}\rangle}\right)=\exp\left(-\frac{I_{ab}}{\langle I_{ab}\rangle}\right) \tag{5-15}$$

where $\langle I\rangle$ is the averaged intensity of all the speckles.

In the localized regime, the probability distribution of the normalized intensity is predicted to satisfy a stretched exponential distribution [Chabanov *et al.*, 2000]

$$P\left(\frac{I_{ab}}{\langle I_{ab}\rangle}\right)\sim\exp\left(-2\sqrt{g' I_{ab}/\langle I_{ab}\rangle}\right) \tag{5-16}$$

where g' is a localization parameter. This stretched exponential form is predicted to hold for large $\frac{I_{ab}}{\langle I_{ab}\rangle}$.

For a complete set of data over a wide frequency range and for several samples, see Appendix B. To calculate the probability of $I_{ab}/\langle I_{ab}\rangle$, the number of values of $I_{ab}/\langle I_{ab}\rangle$ falling in a certain bin size was counted and then was normalized by the total number and the bin width. Usually, a larger bin width was chosen for large $I_{ab}/\langle I_{ab}\rangle$, where the number of counts was low and I_{ab} decreased relatively slowly, than for low

$I_{ab}/\langle I_{ab}\rangle$, thus ensuring optimal statistics at large I_{ab} while not forgoing good resolution at small I_{ab}. Take the intensity distributions for sample 3 in the low frequency range (~ 0.7 MHz) for example. 289 speckles were acquired in this frequency range. The intensity distributions at 0.6 MHz, 0.7 MHz and 0.9 MHz were found to be similar. To improve the statistics, the number of counts in each $I_{ab}/\langle I_{ab}\rangle$ bin for these three frequencies was added together, and the resulting average distribution was then normalized. The resulting intensity distribution for this frequency range is shown in figure 5.3.12. The solid line represents the Rayleigh distribution. The excellent agreement between this distribution and the data indicates that the modes are diffusive.

The high frequency range around 2 MHz was also investigated. More than 3025 speckles were acquired for this frequency range. The distribution of $I_{ab}/\langle I_{ab}\rangle$ for sample 5, sample 6 and sample 7 in the frequency range 2.3 MHz, 2.4 MHz, 2.5 MHz behaved similarly. Thus, to improve statistics, the distribution of $I_{ab}/\langle I_{ab}\rangle$ for these frequencies and samples were averaged together. Hence, the number of speckles involved was more than 26500, which gave very good statistics. The resulting intensity distribution is shown in figure 5.3.13. We can see the intensity distribution shows a clear departure from the Rayleigh distribution, which is shown by the dashed line. The solid curve is a fit to the tail ($I_{ab}/\langle I_{ab}\rangle > 10$) of the data with equation (5-16). The best fit of equation (5-16) to the data gives $g' = 0.84 \pm 0.10$, which indicates the modes are localized in this frequency range.

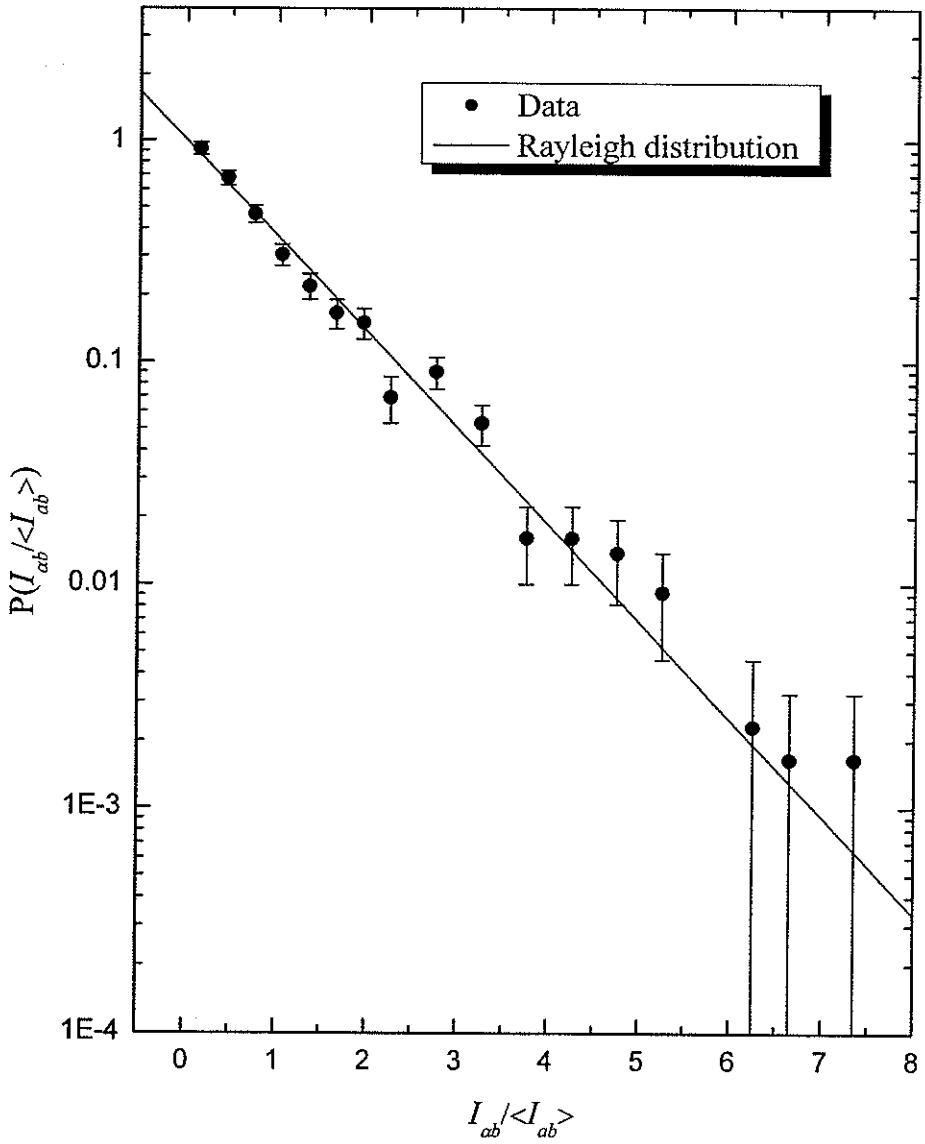

Figure 5. 3. 12 Intensity distribution in the low frequency range (~ 0.7 MHz) compared with the Rayleigh distribution.

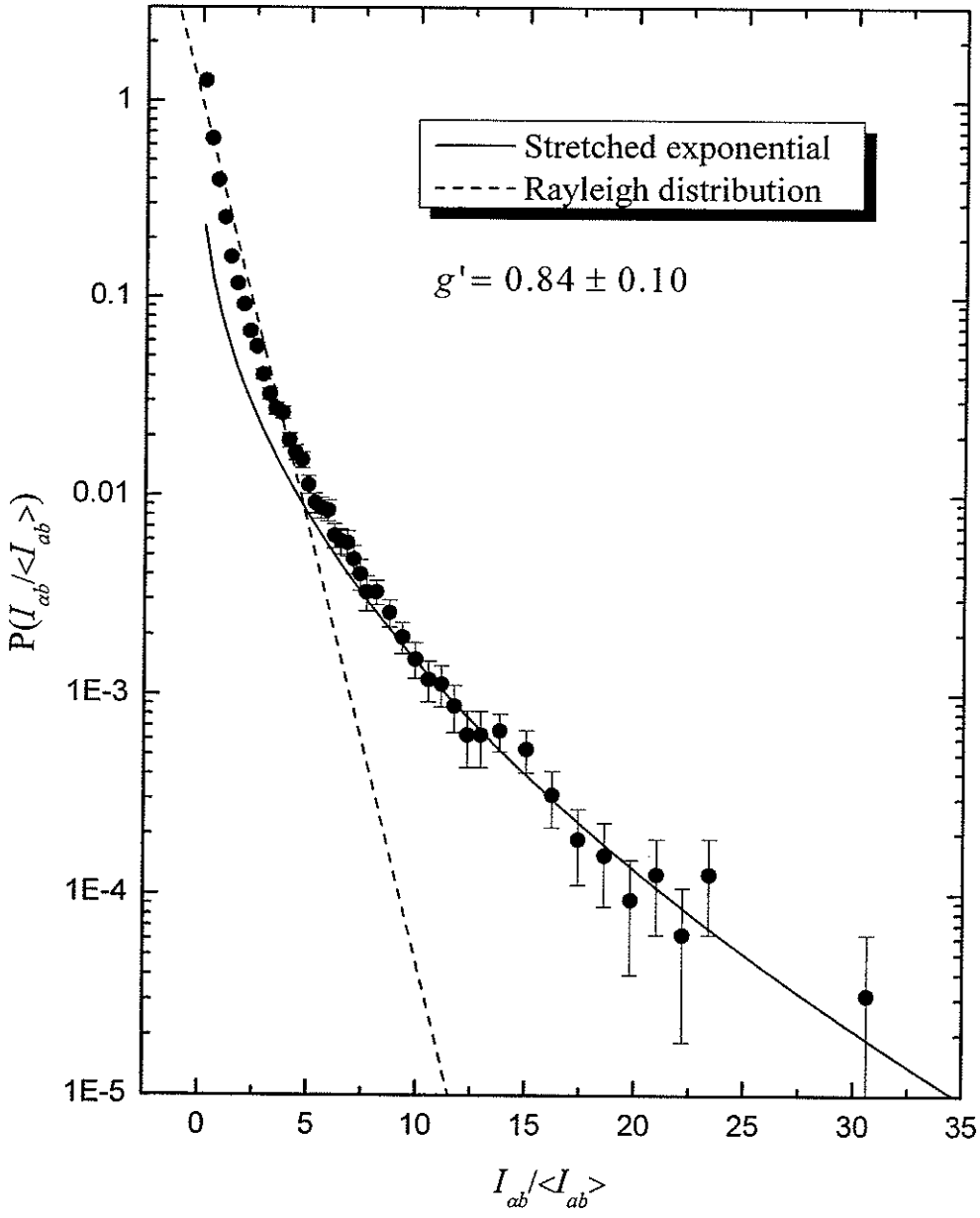

Figure 5. 3. 13 Intensity distribution in the high frequency range (~ 2.4 MHz) compared with a stretched exponential distribution.

5.3.3.2 Variance of the normalized intensity

The localization of waves is characterized by large fluctuations in all transmission quantities. For quasi-one dimensional samples, it has been demonstrated that localization is achieved when the variance of the normalized transmission satisfies [Chabanov *et al.*, 2000]

$$\mathrm{var}(I_{ab} / \langle I_{ab} \rangle) \geq \frac{7}{3} \qquad (5\text{-}17)$$

whether absorption is present or not. This condition (5-17) corresponds to the localization parameter $g' \leq 1$. Although, equation (5-17) is only known to hold for quasi-one dimensional systems, measurements of the variance of the normalized intensity can still be used to probe the approach to localization for our 3D samples.

The upper panel in figure 5.3.14 illustrates the dependence of the variance of the normalized intensity on frequency. The horizontal dashed line shows the threshold value of 7/3. Although this threshold may not be an accurate criterion for localization in 3D [Kogan and Kaveh, 1995], we can see that as the frequency increased, the variance also increased, suggesting that the modes become more localized at higher frequencies. The variances for different samples were also compared, and were found to have a similar increasing trend, as shown in figure 5.3.15. The average variance for 2.3 MHz, 2.4 MHz and 2.5 MHz for sample 5, sample 6 and sample 7 was calculated to be 2.90±0.15, corresponding to $g' = 0.70 \pm 0.06$ if equation (2-17) is assumed, which was close to the value ($g' = 0.84 \pm 0.10$) obtained from the stretched exponential fitting in the last section.

This suggests that equation (5-17), or a relationship that is very similar to it, may also hold for three dimensions as well.

The dependence of the transmission coefficient on frequency was also measured, and is shown in the lower panel in figure 5.3.14. To measure the transmission coefficient, the amplitudes of the FFT spectra of each speckle, obtained by hydrophone scanning, were averaged and then normalized by the reference pulse. This normalization therefore eliminated the dependence on transducer response, and gave an accurate measure of the average amplitude of the response function of the medium. The most striking feature of the transmission coefficient is the existence of band gaps, which correspond to the large dips in the transmission; the existence of band gaps in this random system was also observed previously by Turner *et al.* (1998). As pointed out by Turner *et al.*, the upper edges of the bandgaps correspond to scattering resonances of the isolated aluminum spheres, suggesting that the mechanism that gives rise to the band gaps is more analogous to the tight binding model in solid state physics than the Bragg scattering mechanism (which requires a periodic structure). In this weak network system, the scattering resonances, which correspond to large amplitude ultrasonic displacements in the beads, become broadened by the coupling between adjacent beads and also shifted to somewhat higher frequencies, forming the transmission bands that are seen above 0.5 MHz. In between the transmission bands, band gaps are formed, since the overlap in the resonances of the weakly sintered beads is not complete.

The scattering resonances of the beads, short-range order effects that influence the coupling between the beads, and the associated band gaps, facilitate the transition from propagating to localized modes in the samples. We can see that spikes in the variance of the transmitted intensity appear near the lower frequency edge of the band gaps of the sample, indicating that the modes are strongly localized at these frequencies. The widest band gap appears around 0.55 MHz, as shown in figure 5.3.16. The variance reached 360 at the lower frequency edge of the band gap near 0.45 MHz.

The near-field intensity speckle pattern is also very helpful to demonstrate the signature of diffusive or localized regimes. Figure 5.3.17 shows the near-field intensity speckle pattern at 0.7 MHz. Most speckles overlap with each other, indicating that ultrasound can readily diffuse through the sample suggesting that the modes are diffusive. By contrast, the near field intensity speckle pattern at 2.4 MHz is shown in figure 5.3.18. The pattern is dominated by a few bright spikes with little overlap between speckles, which is another signature of the localization of classical waves [John, 1997]. Thus figure 5.3.18 adds additional evidence that the localization of sound has been observed in the upper part of the intermediate frequency regime in these samples.

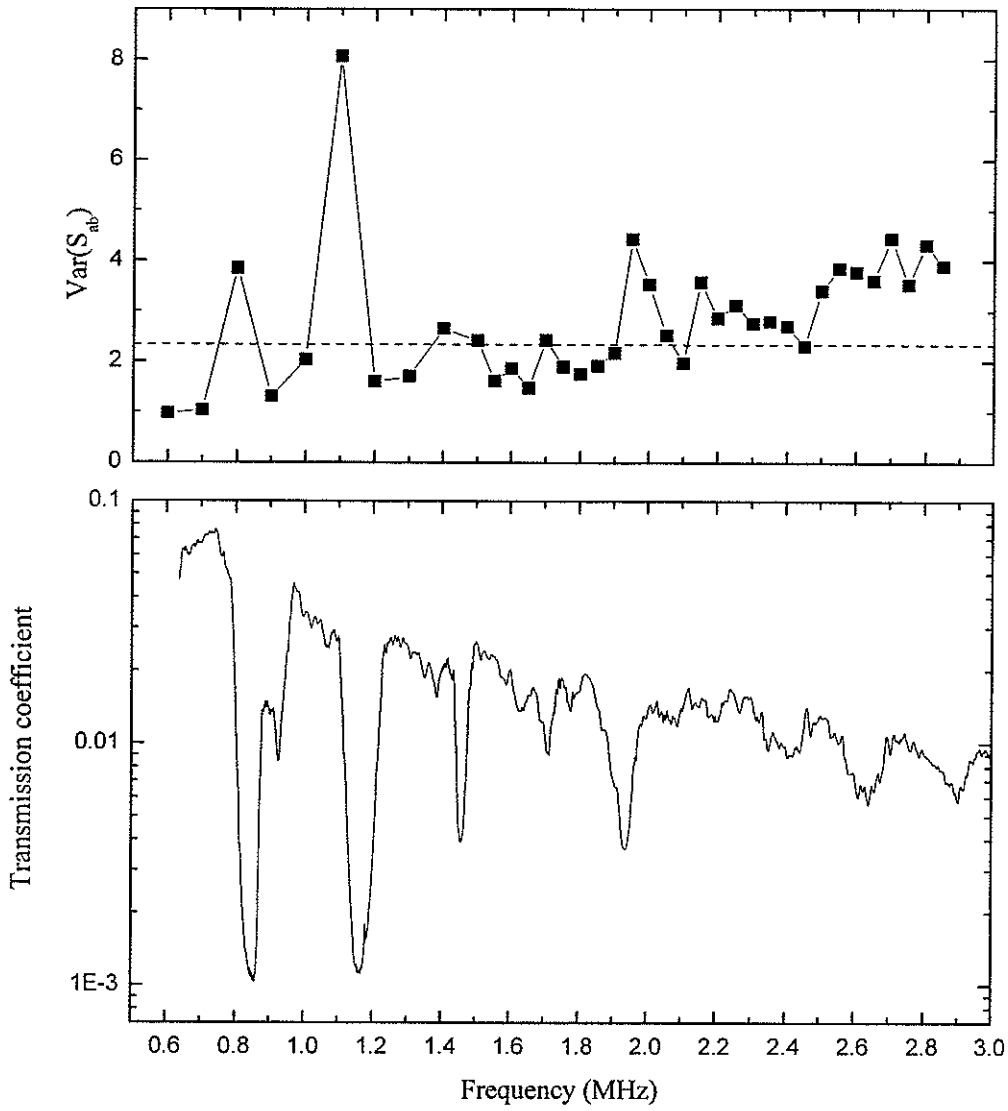

Figure 5. 3. 14 Upper panel: Variance of normalized intensity dependence of frequency. Lower panel: Amplitude transmission coefficient dependent of frequency.

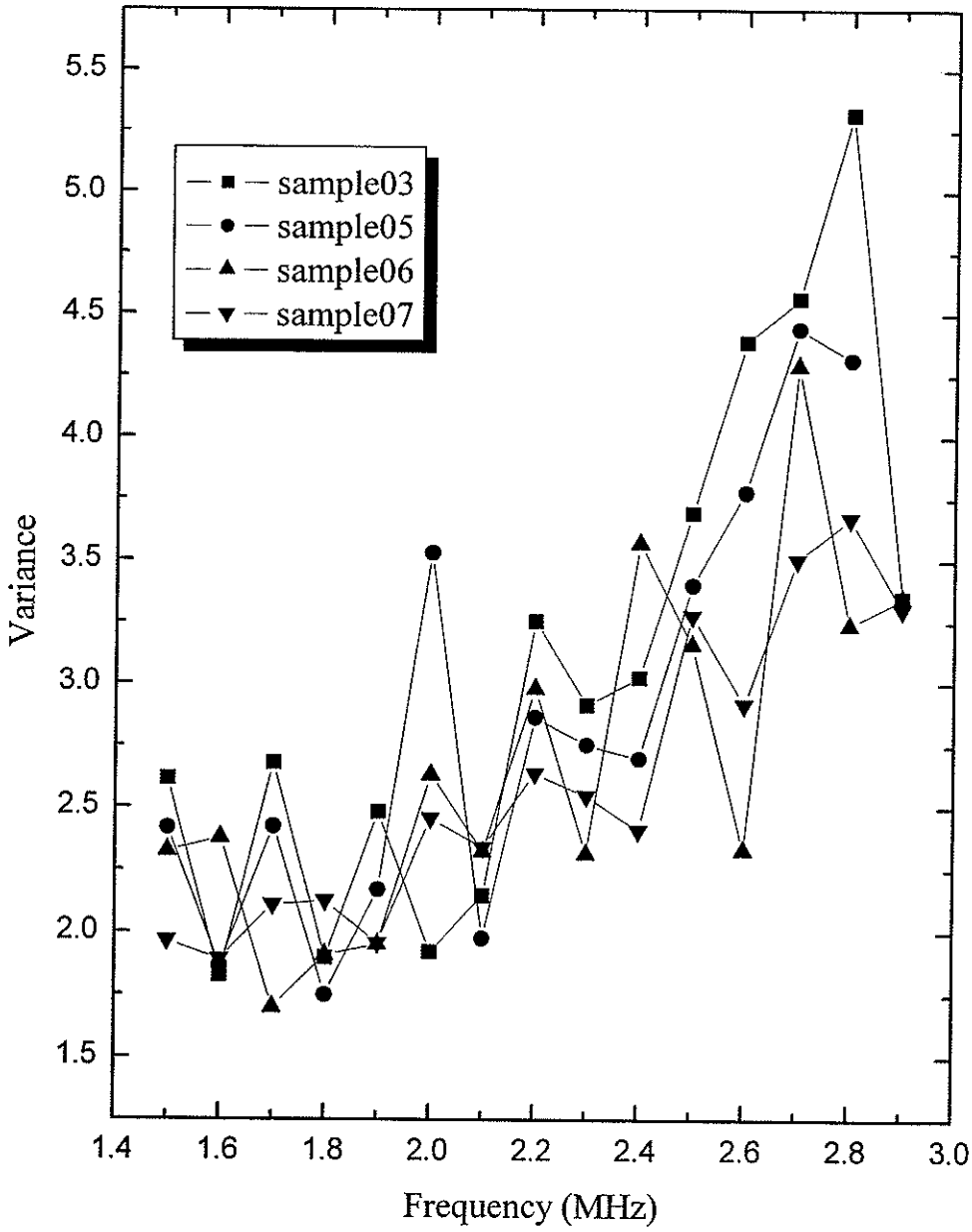

Figure 5. 3. 15 Variance comparison for different samples.

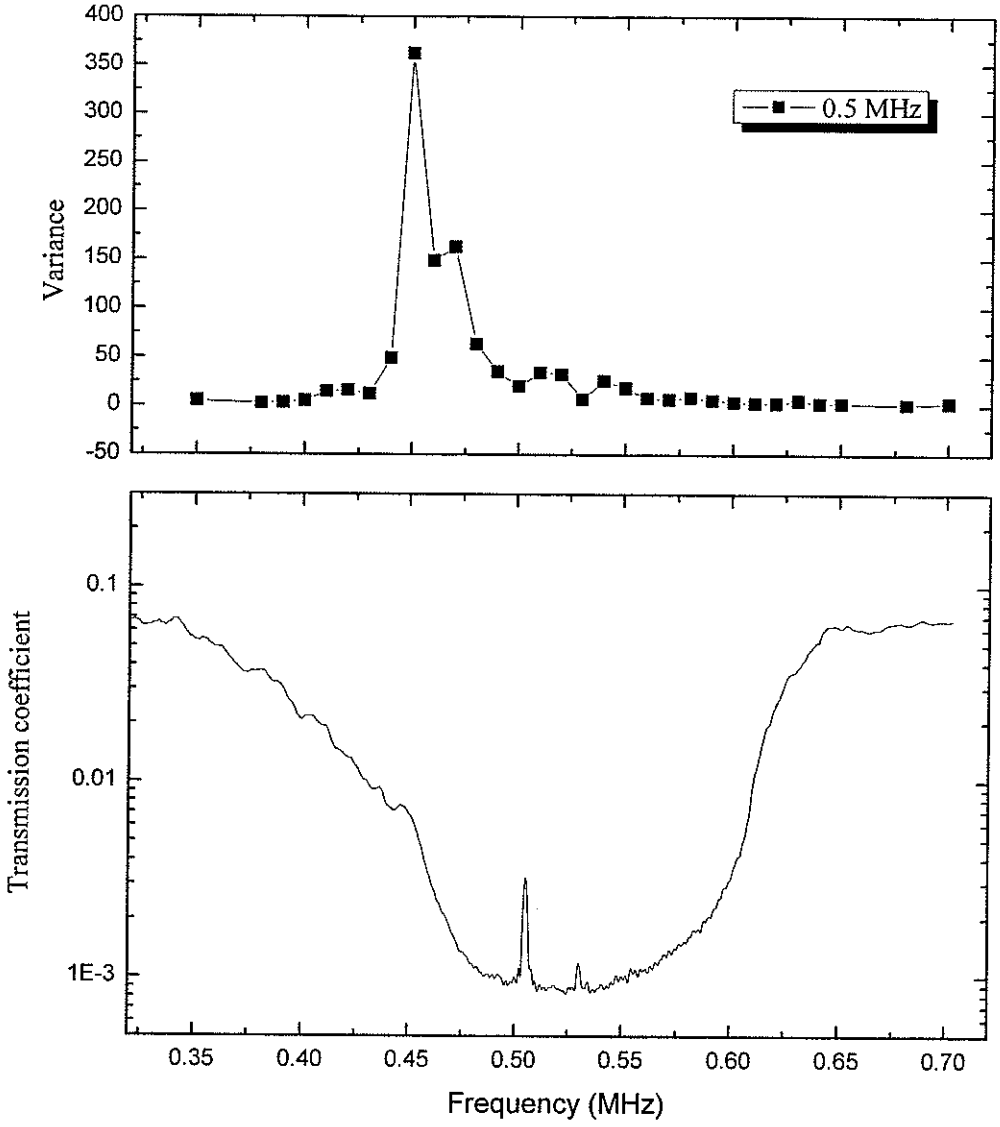

Figure 5. 3. 16 Upper panel: Variance of normalized intensity dependence of frequency. Lower panel: Amplitude transmission coefficient dependent of frequency.

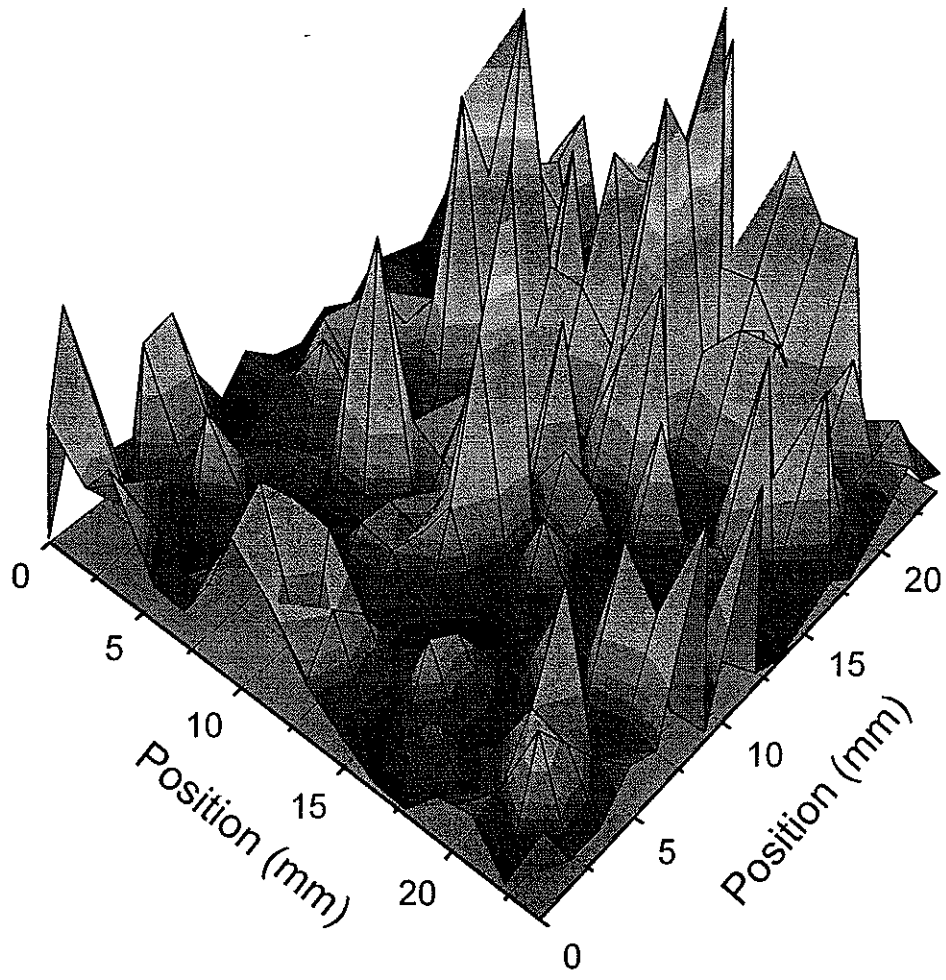

Figure 5. 3. 17 Near-field speckle pattern at 0.7 MHz.

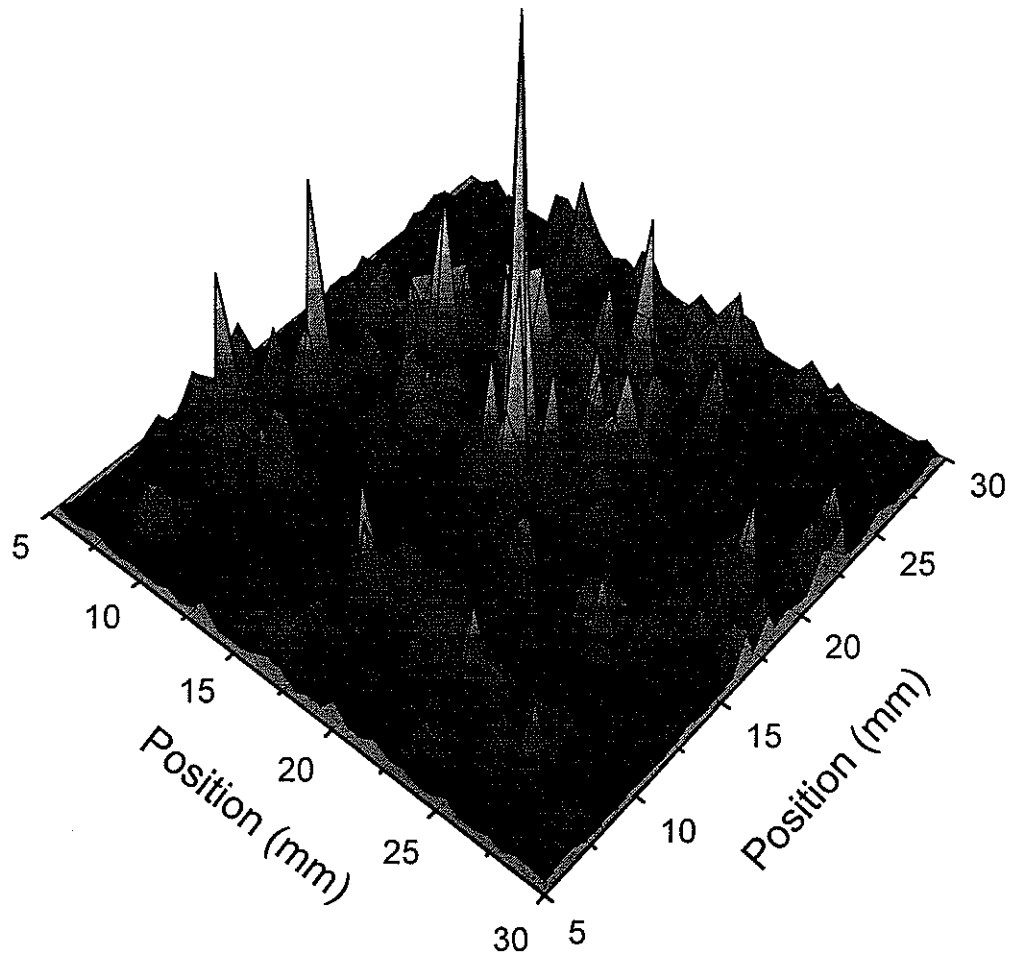

Figure 5. 3. 18 Near-field speckle pattern at 2.4 MHz.

5.4 Crystal

5.4.1 Motivation

In the last section, the band gaps, associated with short range order and the effect of scattering resonances of the weakly sintered beads, were found for the random samples. Here, the transmission spectrum of the crystals, for which the sintered aluminum beads were periodically positioned, was investigated. Recently there has been a lot of work, theoretically and experimentally, on band gaps in three-dimensional phononic crystals [Liu *et al.*, 2000; Yang *et al.*, 2002; Page *et al.*, 2003, Sukhovich *et al.*, 2004, Page *et al.*, 2005]. For those phononic crystals, the scatterers were monodisperse beads periodically arranged in a close packed lattice, in which the beads touched each other but were not attached to each other by bond connections. In this section, we present the results for crystals made from our sintered beads system, in which sound propagation must proceed through the network of coupled beads rather than through the surrounding medium, making a complementary phononic structure to those studied previously.

5.4.2 Transmission coefficient

Three crystals of 3 layers, 4 layers and 6 layers, respectively, were made. In the experiment, the incident pulse propagated along the [111] direction of a face centered cubic lattice, in accordance with the design of the crystals. Two large-element-diameter transducers were used to perform transmission coefficient measurements at 0.1 MHz, 0.25 MHz, 0.5 MHz, and 1 MHz. The experimental procedure was the same as that of

ballistic measurements for random samples. From the transmission measurement, band gaps, which corresponded to very small values of the transmission coefficient, were found in some frequency ranges. The first widest band gap appeared around 0.55 MHz for the three crystals. Figure 5.4.1 shows the details of input and averaged transmitted pulses, and their Fourier spectra around 0.5 MHz for the 3-layer crystal. Figure 5.4.2 shows the details of the band gap around 0.5 MHz for the 3-layer crystal.

The transmission coefficient over the whole frequency range that we investigated is plotted in figure 5.4.3 for three crystals with different thicknesses. As was mentioned in the sample preparation section, our crystals had some missing bonds. Due to some degree of disorder in the crystals, the amplitude transmission coefficient became noisier as the sample thickness increased. The band gaps showed up in the same frequency range for the three crystals. The comparison of the transmission coefficient between the 4-layer crystal and the random sample number 3 is shown in figure 5.4.4. The band gaps appeared around the same frequencies, and have a similar width. Remarkably, the random sample has a deeper band gap, showing that short range order, rather than perfect periodic order, is all that is needed to form band gaps in this system.

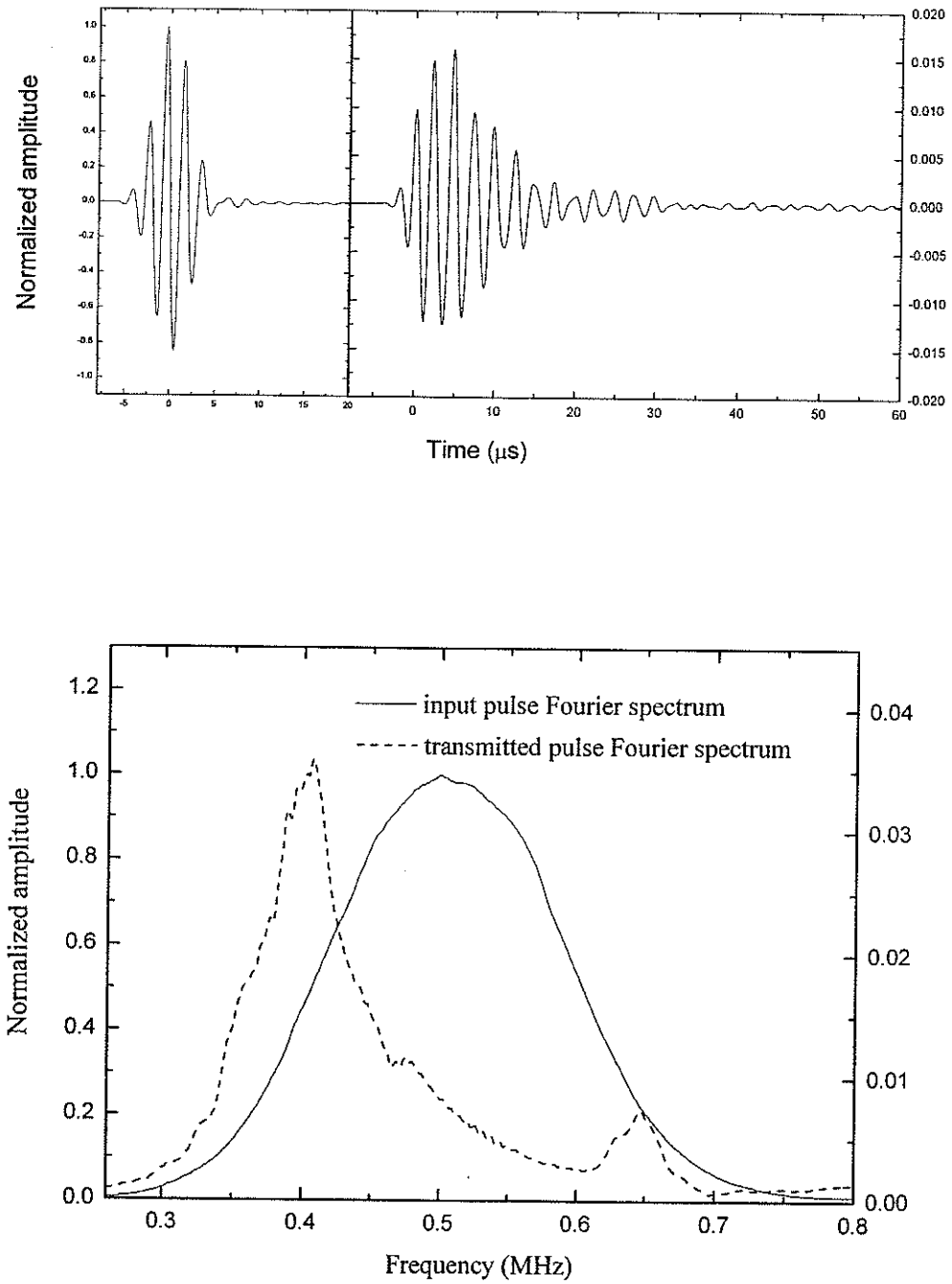

Figure 5. 4. 1 Upper panel: 0.5 MHz input and transmitted pulses through a 3-layer crystal. Lower panel: Fourier spectrums of input and transmitted pulses.

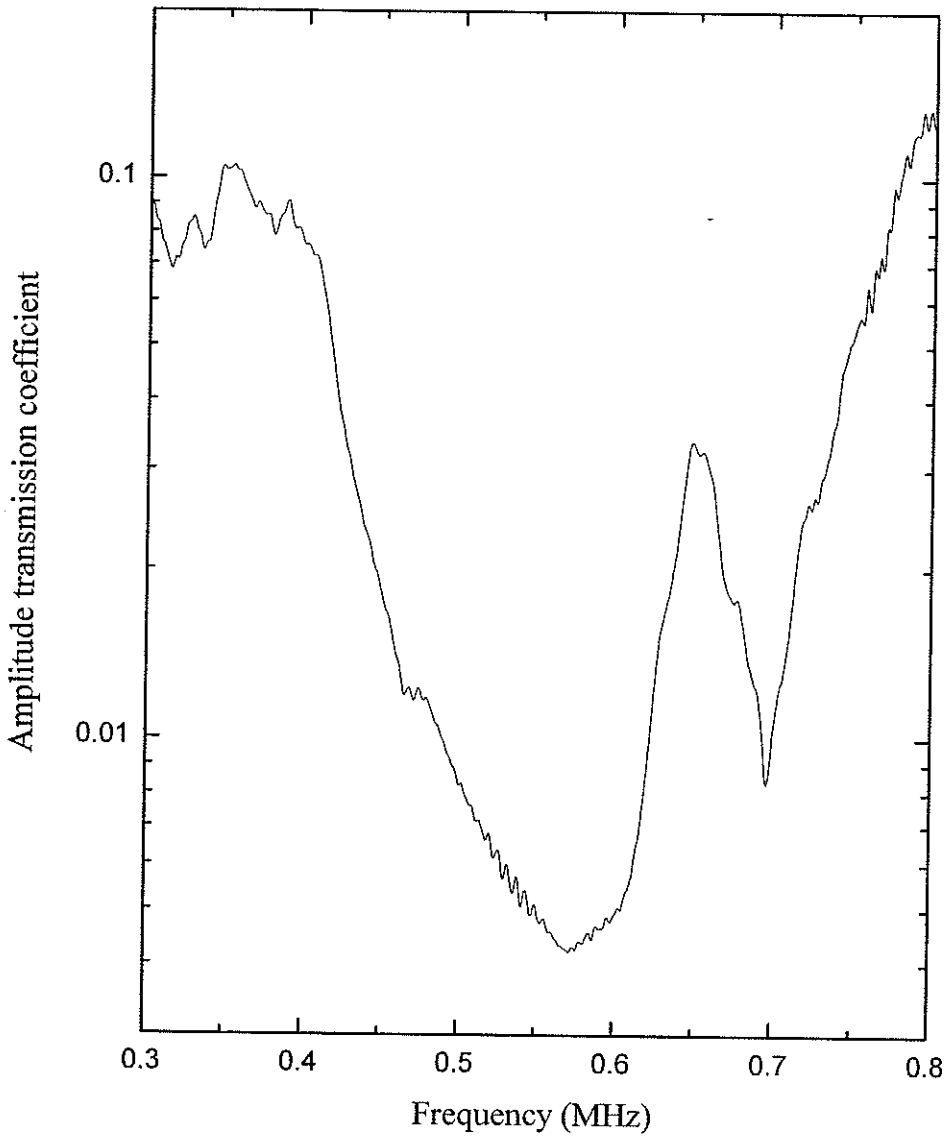

Figure 5. 4. 2 Frequency dependence of the transmission coefficient in the widest band gap for 3-layer crystal.

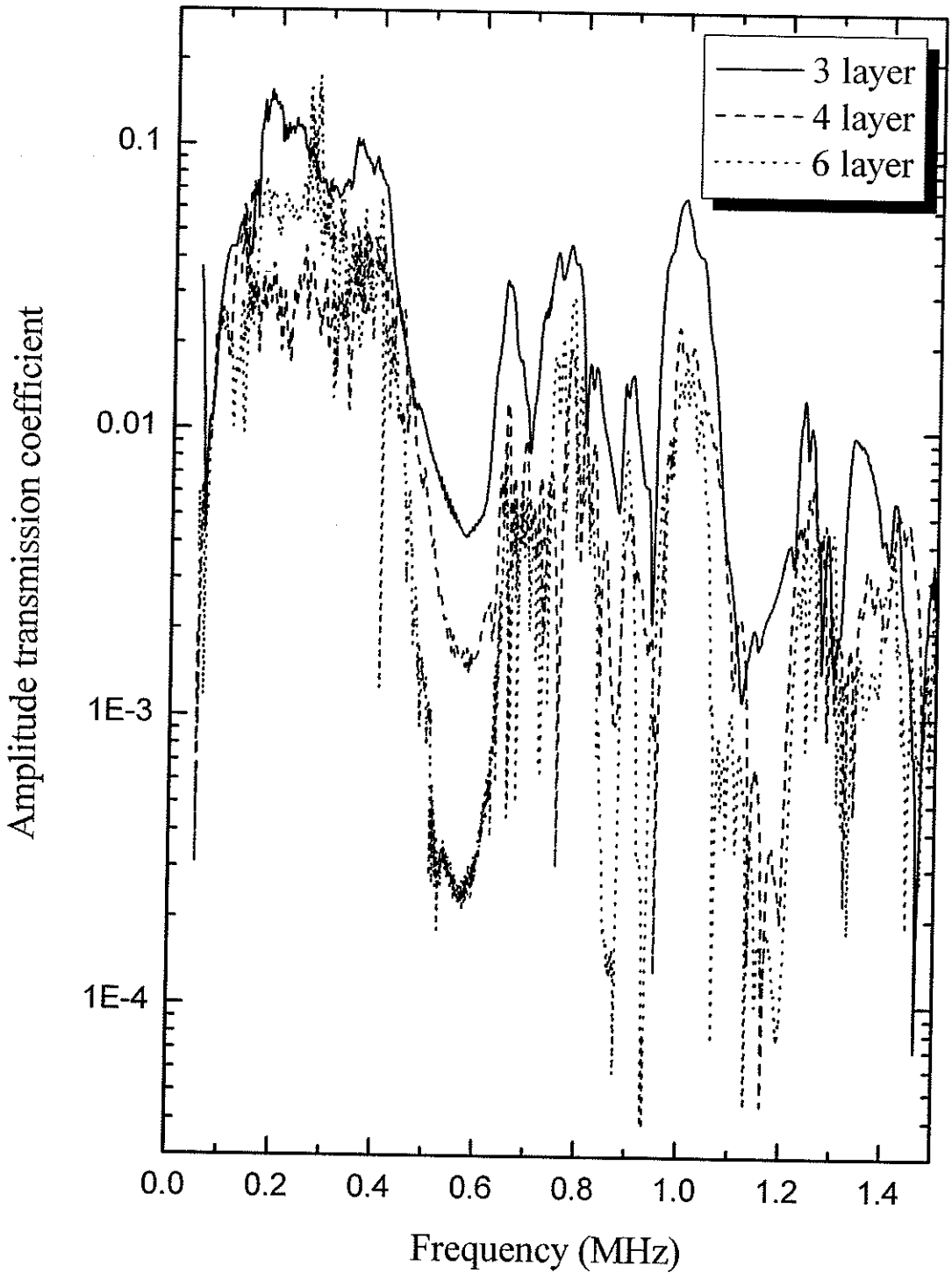

Figure 5. 4. 3 Amplitude transmission coefficient of crystals with different thickness.

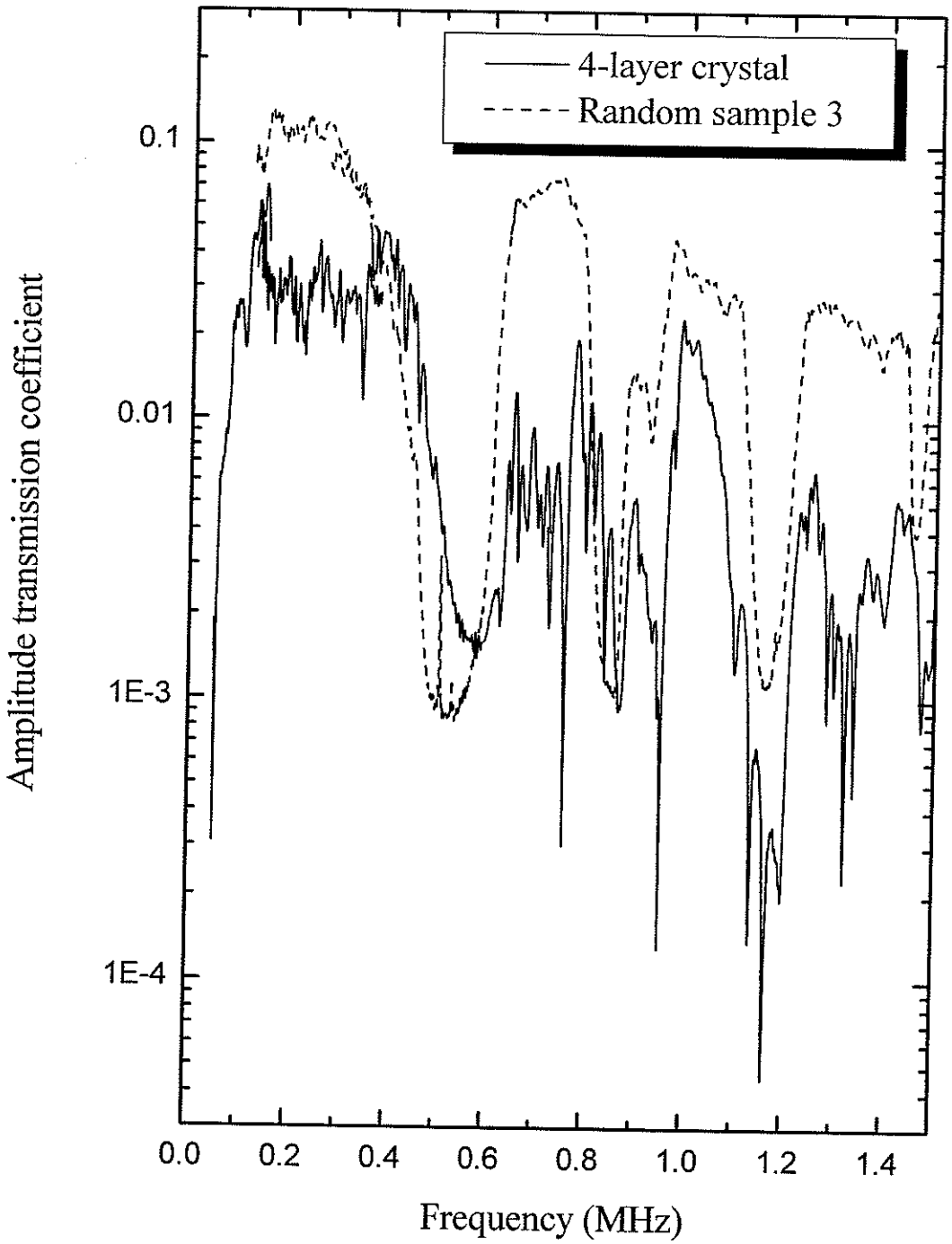

Figure 5. 4. 4 Comparison of amplitude transmission coefficient between the 4-layer crystal and random sample 3. The two samples have similar thickness, 14.2 and 14.5 mm, respectively.

5.4.2 Group and phase velocity, and dispersion

For phononic crystals made from tungsten carbide beads immersed in water, ultrasound tunneling was reported in the band gap [Yang *et al.*, 2002]. In the band gaps of these phononic crystals, the group velocities were found to increase as the sample thickness increased, implying a tunneling time that is independent of thickness. In this section, group velocities were also determined for our three crystals. In our crystals, an even more striking effect was observed: the group velocity was found to be negative in the first widest band gap of the 3 crystals, as illustrated in figure 5.4.5. This counterintuitive effect results from the unusual dispersion in our crystals, which causes the beginning of the pulse to travel faster than the tail, so that the peak of the pulse traveling through the crystal emerges from the far side of the crystal before the peak of the incident pulse has entered the crystal. From the plot, we can see that the negative group velocities became more negative in the band gap as the crystal thickness increased. Meanwhile, because of some degree of disorder in the crystals, the frequency range of negative group velocity shrank as the crystals became thicker.

This observation of negative group velocities for evanescent modes in the gap is a rather dramatic extension of previous observations of "supersonic" acoustic velocities in phononic crystals [Yang *et al.*, 2002], as well as superluminal group velocities for optical pulses tunneling through the band gap of photonic crystals [e.g., see Steinberg *et al.*, 1993]. For example, in a 1D photonic crystal made from a multilayer dielectric mirror,

a group velocity equal to $1.7c$ was found, where c is the velocity of light in vacuum [Steinberg *et al.*, 1993]. More recently, a coaxial photonic crystal has been constructed in which the tunneling of a pulse through the band gap is so fast that a negative group velocity was observed [Munday and Roberston, 2002], although it is not clear that the origin of negative group velocity in this simple 1D coaxial cable structure is same as in our 3D phononic crystal. In all these cases, it is important to realize that there is no violation of causality: the effect arises from a change in shape of the pulse due to interference of the different frequency components, which in the case of anomalous dispersion cause the peak of the pulse to be advanced rather than retarded in time as it travels through the crystal.

Phase velocities were also measured from the pulse transmission data, starting at lowest frequency range (0.1 MHz) where the correct $n2\pi$ shift was easiest to determine. It was found that the phase velocity was remarkably small at low frequencies, even for the largest possible values ($n = 0$). Thus the data shown in figure 5.4.6 are the fastest phase velocities in the 0.1 MHz frequency range, and data for higher frequencies were joined smoothly to form a continuous curve over the entire frequency range. Figure 5.4.6 shows that phase velocities increased rapidly in low frequency range and dropped significantly around 0.7 MHz, which was the high frequency edge of the gap.

Figure 5.4.7 illustrates the dispersion relation, which gives the relation between

frequency and wave vector, where the wave vector k is determined from the measured frequency and phase velocity v_p

$$k = \frac{2\pi}{\lambda} = \frac{2\pi f}{v_p}, \tag{5-1}$$

The group velocity can be expressed as

$$v_g = d\omega / dk, \tag{5-2}$$

where $\omega=2\pi/f$ is angular frequency. Hence, the negative slope around 0.5 MHz in the dispersion curve is consistent with negative group velocity.

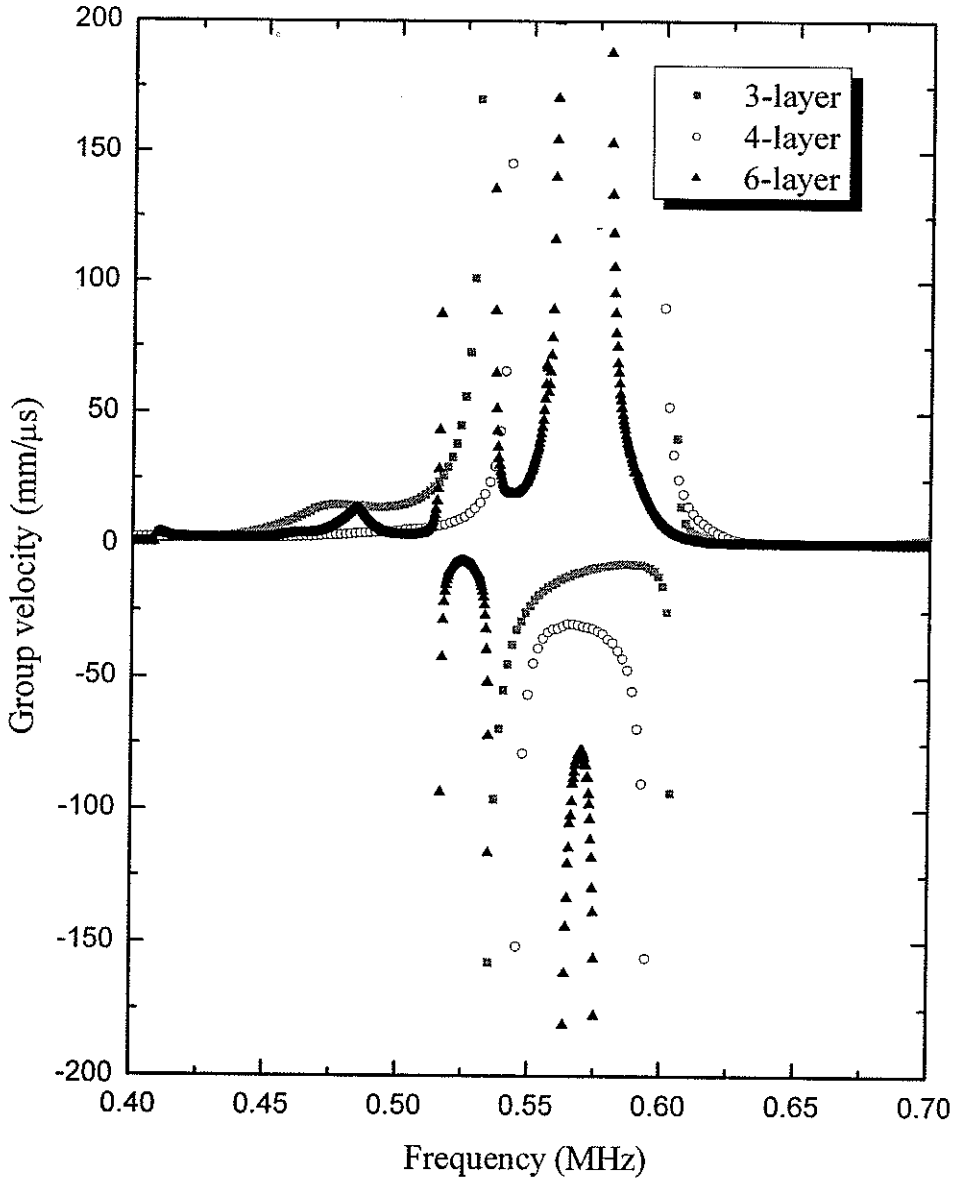

Figure 5. 4. 5 Group velocities in the widest band gap of 3 crystals.

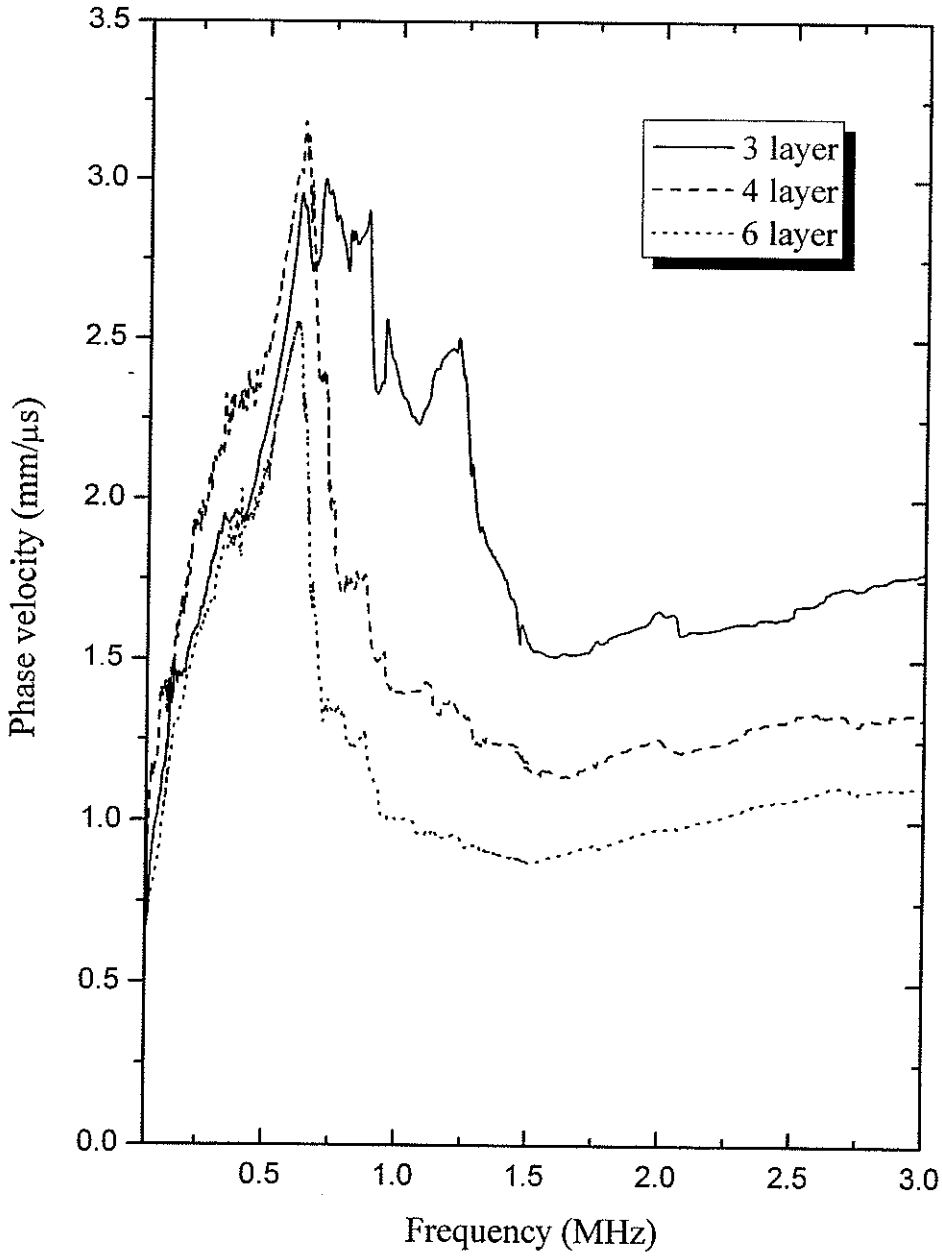

Figure 5. 4. 6 Frequency dependence of phase velocities for 3 crystals.

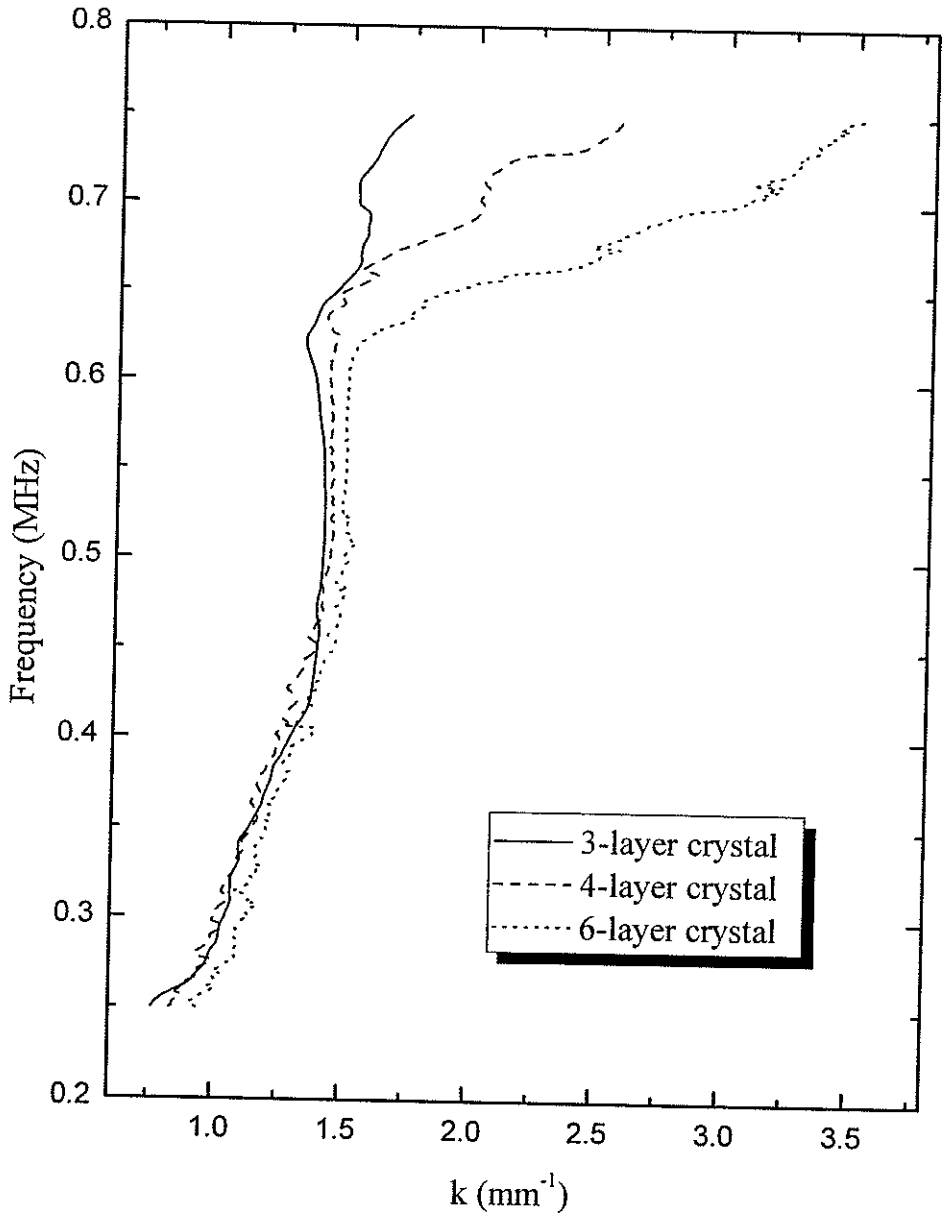

Figure 5. 4. 7 Dispersion curve of the 3 crystals in the vicinity of the first band gap.

Chapter 6 Conclusions

The transport of ultrasonic waves through sintered aluminum bead samples was studied in the intermediate frequency range, in order to investigate the effects of very strong scattering on wave propagation in both disordered and crystalline media.

In the lower part of the intermediate frequency range (~0.25 MHz), we first measured the ballistic parameters, the scattering mean free path as well as the phase and group velocities, and used these parameters to evaluate the boundary conditions that influence diffusive transport. Then the ensemble-averaged transmitted intensity $I(t)$ was determined at different frequencies. $I(t)$ for all the samples was found to have an exponential decay at long times, which was very well explained by diffusion theory. The fitting to the measured $I(t)$ with the predictions of diffusion model enabled the values of the diffusion coefficient D and the absorption time τ_a to be determined. The values of D varied from 1 $mm^2/\mu s$ to 2 $mm^2/\mu s$ for different samples, and D was found to be independent of frequency in this frequency regime. This result is consistent with measurements of the diffusion coefficient in very porous glass bead networks throughout the lower part of the intermediate frequency regime [Page *et al.*, 2004], which in that case extended over a much wider frequency range than in our less porous samples. The absorption time τ_a was found to be infinity by the fitting, so that it was too small to measure in the diffusive regime. The success of explaining the data by diffusion theory

indicated that the multiply scattered ultrasound propagates by diffusion in the lower part of the intermediate frequency range, which is therefore the diffusive regime.

In the upper part of the intermediate frequency range (~ 2 MHz), the scattering of ultrasonic waves became stronger, so that the ballistic parameters were difficult to measure. By contrast, the ensemble-averaged transmitted intensity $I(t)$ was accurately determined in this frequency range. In contrast to the diffusive regime, the tail of $I(t)$ had a non-exponential decay, which cannot be interpreted by the diffusion theory. In this frequency range, the absorption time τ_a became measurable. By fitting the initial increase and the exponential part of the early time behavior of $I(t)$, τ_a was determined. After making a correction for absorption by multiplying $I(t)$ by $\exp(t/\tau_a)$, the tail of $I(t)$ was found to obey the power law, $I(t) \sim t^{-(1+s)}$ with $s \approx 0.85$, which was predicted by the theoretical calculations for localization [Skipetrov and van Tiggelen, 2006]. We then calculated the values of the diffusion coefficient D from $I(t)$, and found the diffusion coefficient D was time-dependent and was decreasing as $1/t$ at long times, which was also consistent with the localization theory.

In addition to the observation of time dependence in the diffusion coefficient, the statistical approach was used to show another signature of localization. The normalized transmitted intensity was measured and the intensity distribution $P(I_{ab}/\langle I_{ab}\rangle)$ was then obtained. The tail (s_{ab}>10) of the intensity distribution at frequencies near 2.4 MHz

was found to exhibit stretched exponential behavior, $P(s_{ab}) \sim \exp(-2\sqrt{g' s_{ab}})$, instead of the observed exponential decay in the diffusive regime. By fitting this stretched exponential model to the data, the localization parameter g' was determined, giving $g' = 0.84 \pm 0.10$, which was consistent with the theoretical predication for localization that $g' < 1$ [Chabanov *et al.*, 2000]. A large variance of the normalized transmitted intensity was also found, which again is consistent with localization of classical waves. We found that the variance increased as the frequency increased, indicating that the waves become more localized at higher frequencies, but no sudden onset of localization can be inferred from these data. This is also consistent with a recent theoretical prediction that the localization transition is smooth for open systems [Skipetrov and van Tiggelen]. Although the relation, $P(s_{ab}) = \int_0^\infty \frac{ds_a}{s_a} P(s_a) \exp(-s_{ab}/s_a)$ [Kogan and Kaveh, 1995], is only known to be valid for quasi-one dimensional systems, hence, so is the relation between g' and the variance of s_{ab}, we still used it to obtain an additional estimate for g'. This relation gives $g' = 0.70 \pm 0.06$, which is close to the value of g' obtained from the fitting to the tail of the intensity distribution, suggesting the relation between g' and s_{ab} may even hold for three-dimensional samples. The consistency of these observations with the localization theory indicated the modes were localized in the upper part of the intermediate frequency range, which can therefore be termed the localized regime.

Additional experiments were performed on phononic crystals, made from sintered

aluminum beads in an fcc structure, to investigate the effects of positional order on the band gaps that underlie much of the interesting wave physics in this system. In common with other phononic crystal systems, the main focus was on the transmission coefficient and the coherent velocities (phase and group). It was found that the long range periodic order of the crystals had little effect on the position of the band gaps, confirming that the dominant mechanism for the band gaps is coupled bead resonances and not Bragg scattering. The slight shift in the lowest band gap to higher frequencies can be explained by the additional number of contacts between the beads in the crystal (12 for a close-packed fcc structure), since this will have the effect of shifting the resonances to higher frequencies due to the additional stiffness imposed by neighboring beads. The dynamics of wave transport through the band gap was investigated by measuring the group velocity, which was found to be negative in the gap, with increasingly large negative values for v_g being observed as the thickness of the crystals increased. This observation of negative group velocity is intriguing, because of the close analogy between the tunneling of evanescent waves through a band gap in a phononic crystal and the tunneling of a particle through a potential barrier in quantum mechanics [Yang *et al*, 2002].

In conclusion, the most significant contribution reported in this thesis is the evidence for the localization of ultrasonic (acoustic or elastic) waves in a random system with very strong scattering. For over 20 years, convincing evidence for localization of acoustic

waves in three dimensional systems has been elusive, so that these new results on time dependent diffusion and non-Rayleigh statistics represent a very significant step forward by demonstrating that classical wave localization is indeed possible in 3D. In addition, these data are motivating new theoretical work that has already begun in collaboration with Sergey Skipetrov and Bart van Tiggelen to model the time and position dependence of the diffusion coefficient quantitatively, and thus hold promise for advancing our understanding of this challenging wave phenomenon. My results are also motivating new experiments in the Ultrasonics Research Laboratory to explore additional phenomena that have not previously been seen for ultrasonic waves, such as the behavior of the phase and phase derivatives near the localization transition, as well as the possibility of observing enhanced correlations, both dynamic and static, in speckle patterns in the localization regime; in all these cases, there have been recent theoretical predictions that so far have not been examined experimentally.

Appendices

Appendix A Transmitted intensity profiles

A.1 Transmitted intensity profiles in the 0.25 MHz frequency range

A.1.1 Sample 3

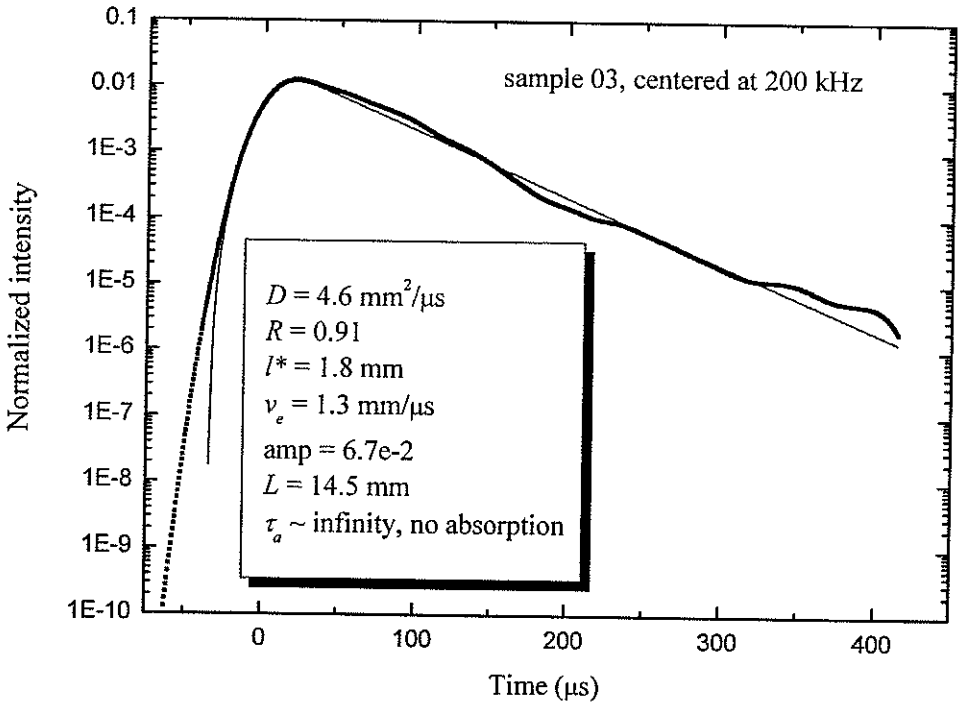

Figure A. 1 Transmitted intensity profile at 0.2 MHz for sample 3.

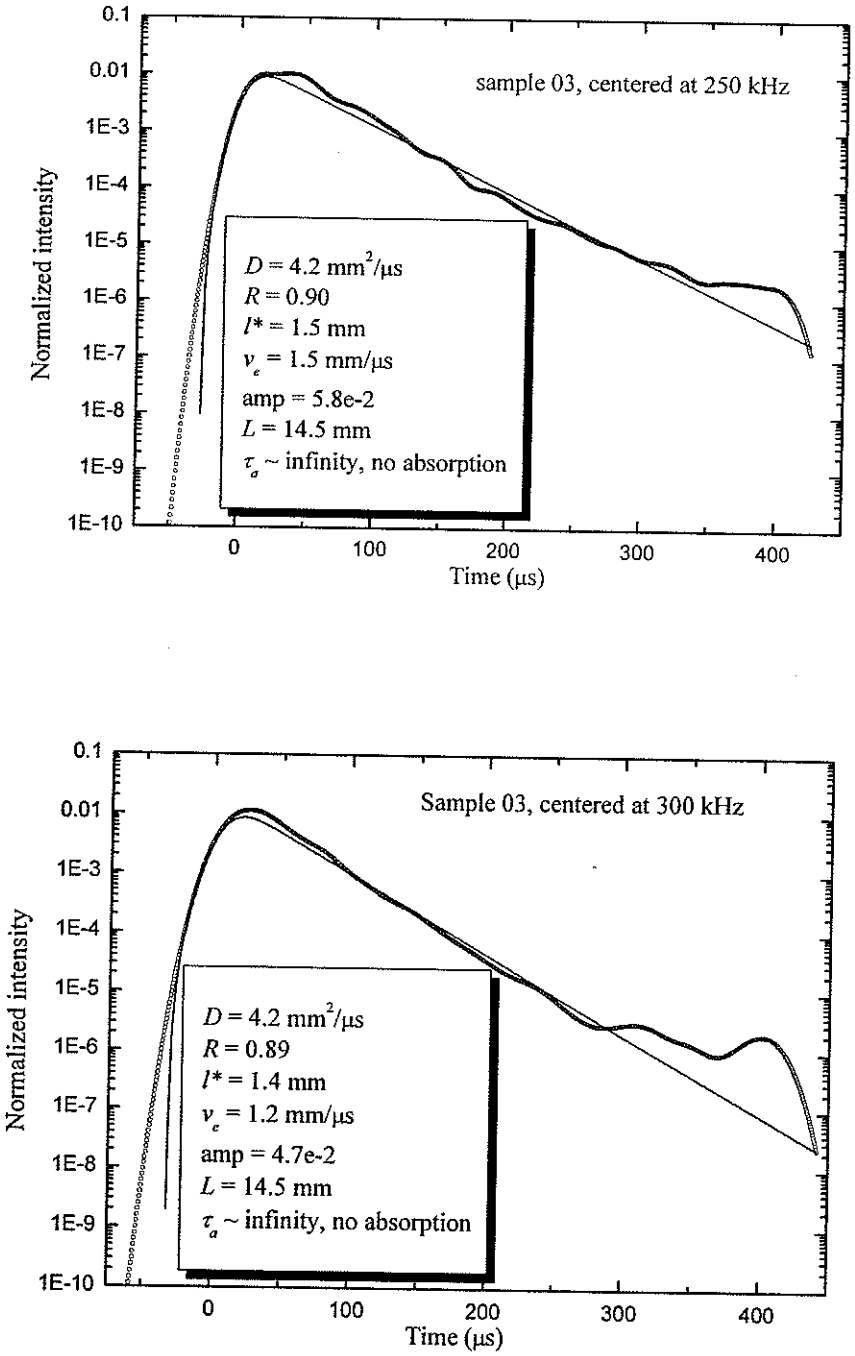

Fig. A.2. Upper figure: transmitted intensity profile at 0.25 MHz for sample 3; Lower figure: transmitted intensity profile at 0.3 MHz for sample 3.

A.1.2 Sample 4

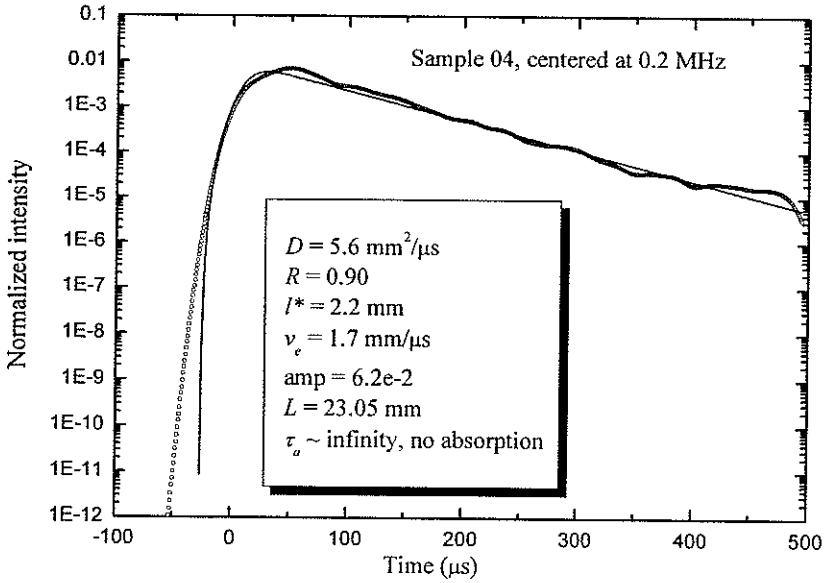

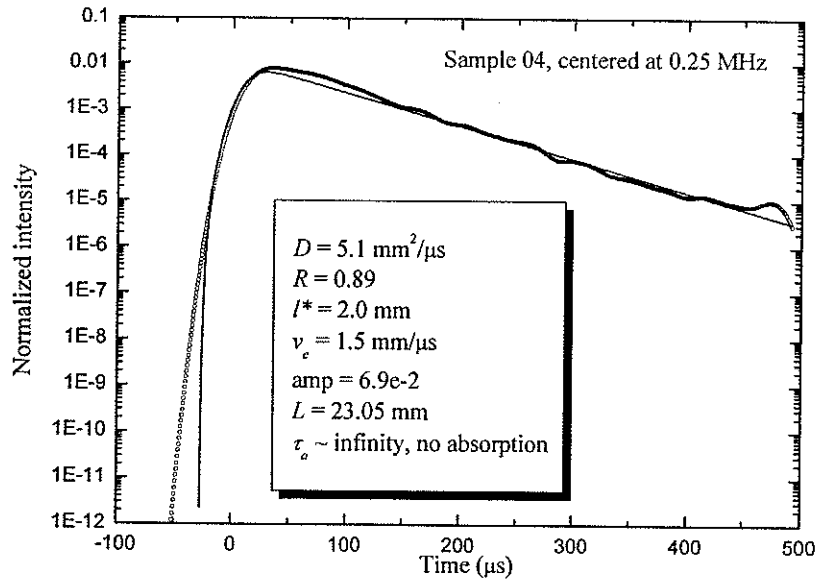

Fig. A.3. Upper figure: transmitted intensity profile at 0.2 MHz for sample 4; Lower figure: transmitted intensity profile at 0.25 MHz for sample 4.

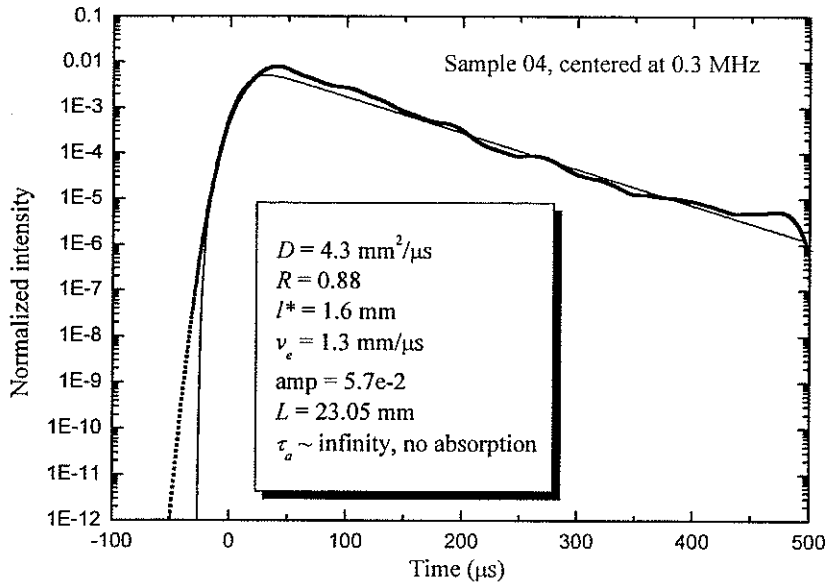

A.1.3 Sample 6

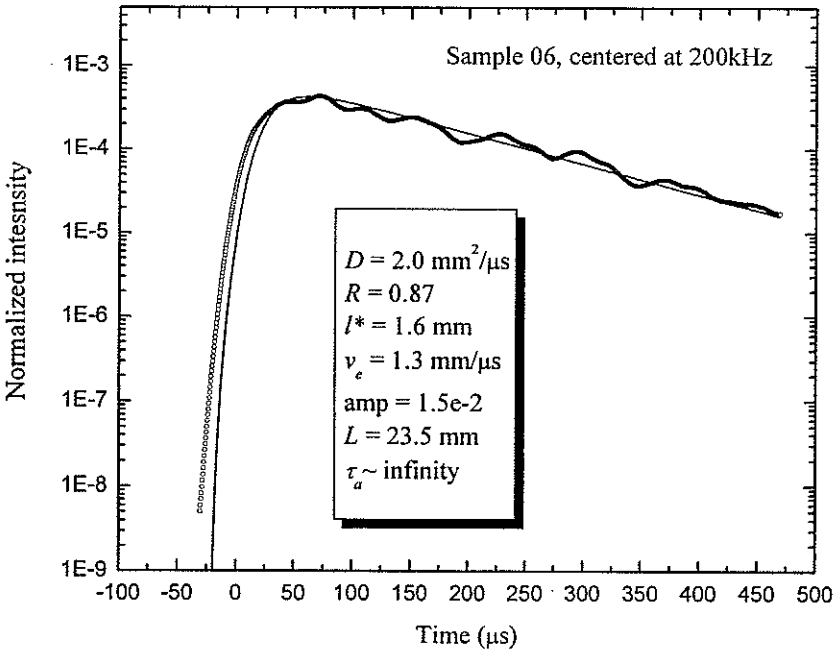

Fig. A.4. Upper figure: transmitted intensity profile at 0.3 MHz for sample 4; Lower figure: transmitted intensity profile at 0.2 MHz for sample 6.

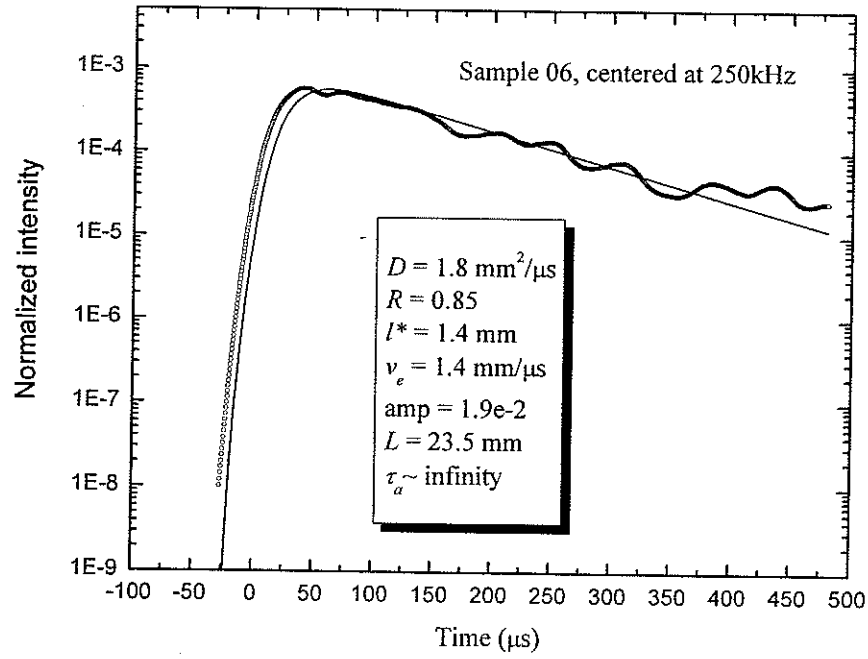

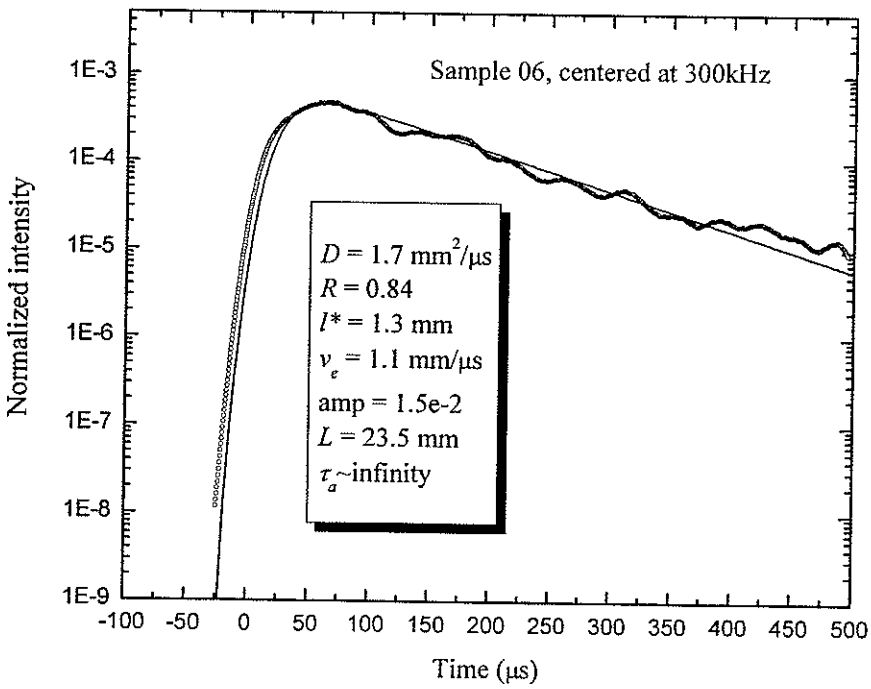

Fig. A.5. Upper figure: transmitted intensity profile at 0.25 MHz for sample 6; Lower figure: transmitted intensity profile at 0.3 MHz for sample 6.

A.1.4 Sample 7

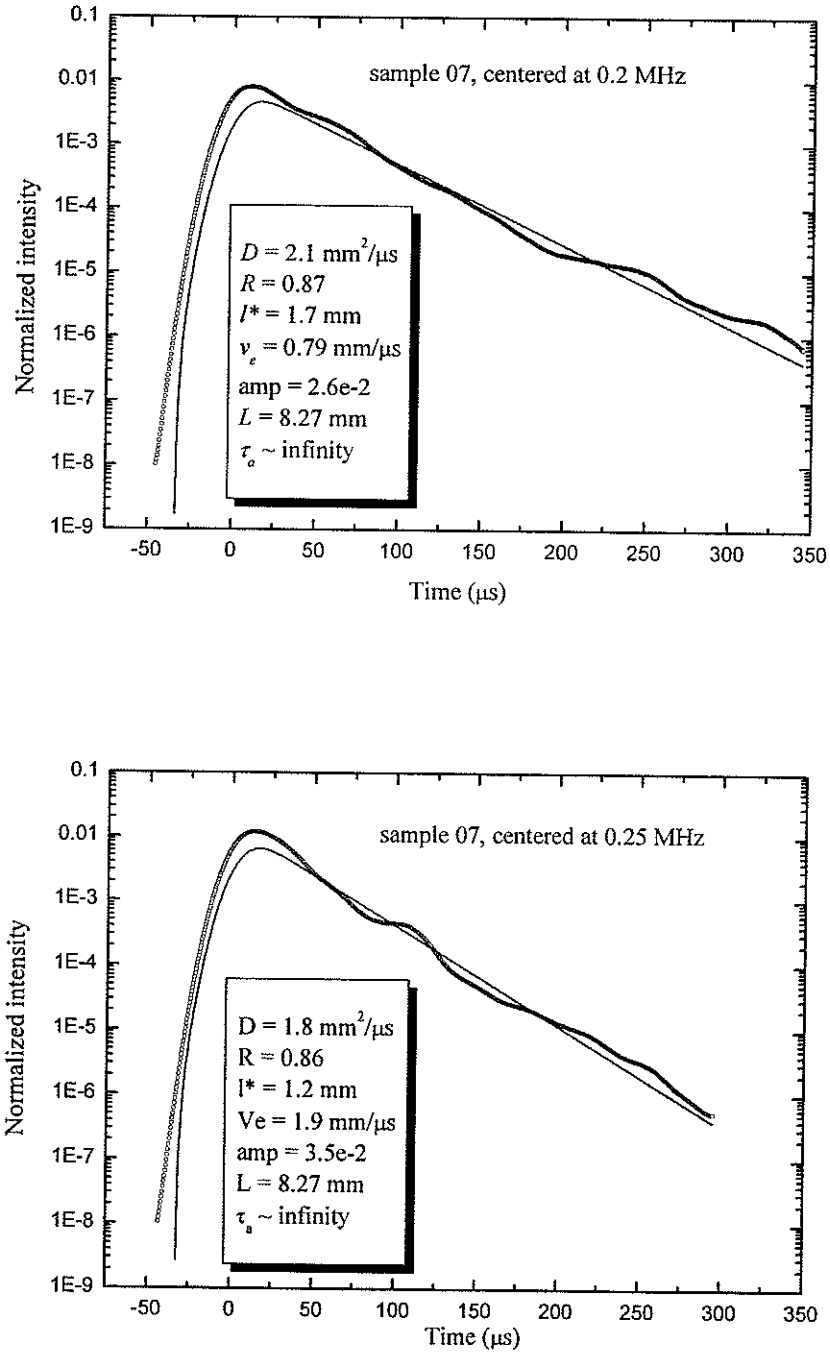

Fig. A.6. Upper figure: transmitted intensity profile at 0.2 MHz for sample 7;
Lower figure: transmitted intensity profile at 0.25 MHz for sample 7.

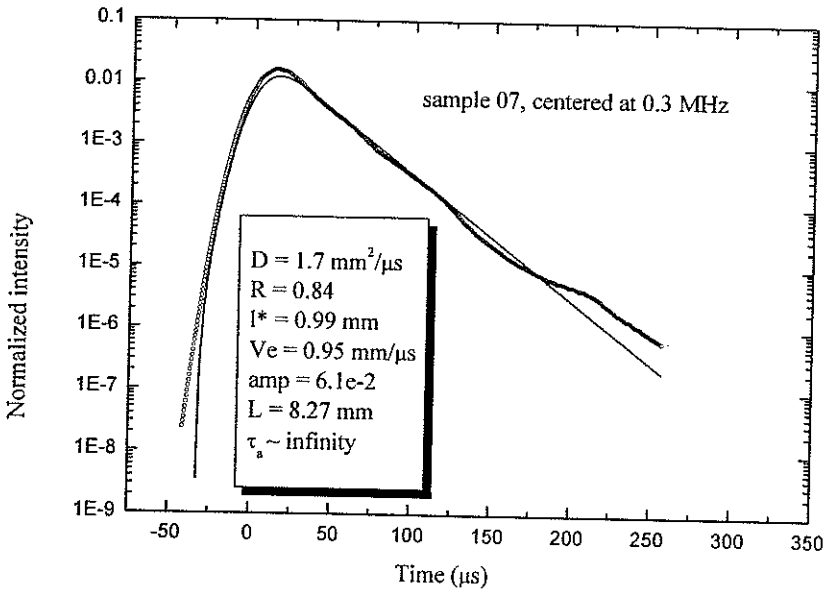

Fig. A.7. Transmitted intensity profile at 0.3 MHz for sample 7.

A.2 Transmitted intensity profiles in the 1 MHz frequency range

A.2.1 Sample 3

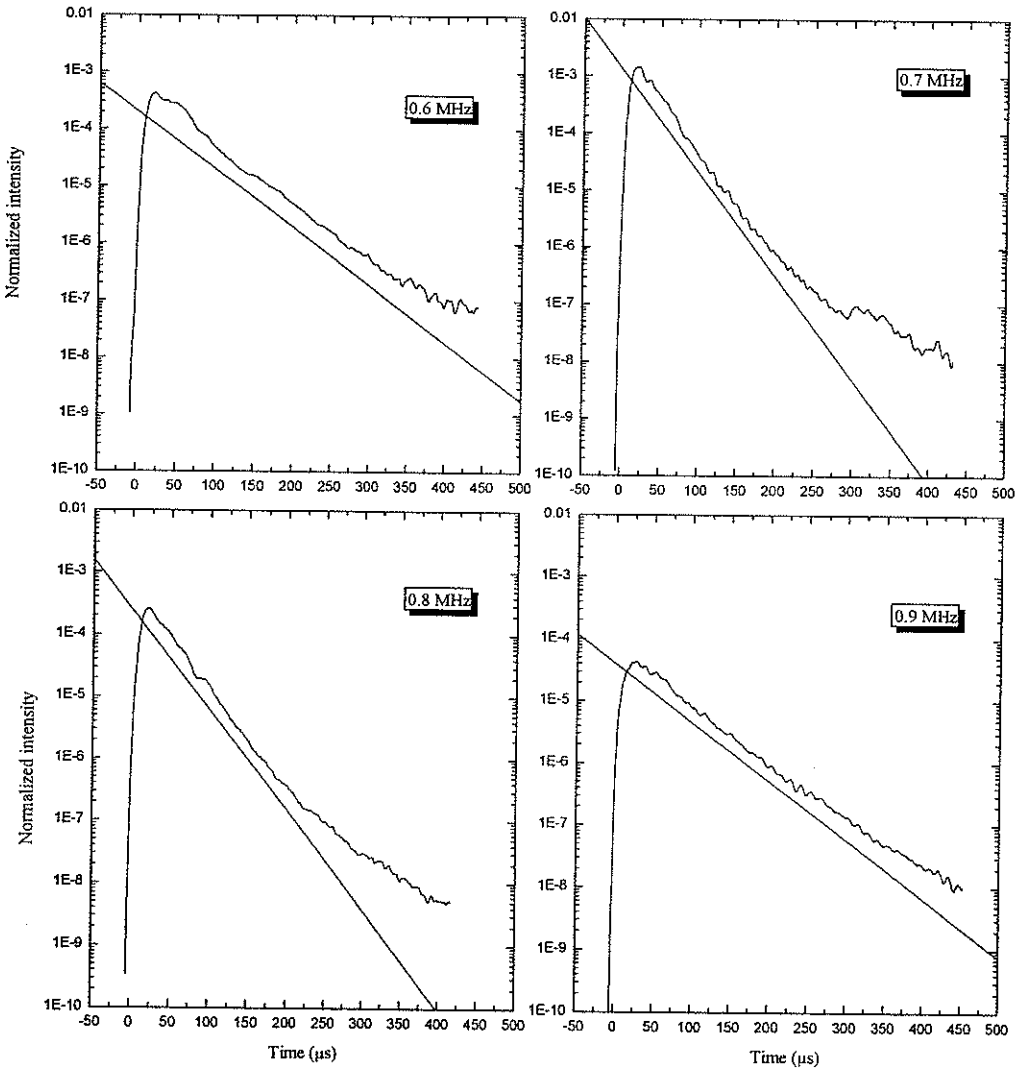

Fig. A.8. Transmitted intensity profile at 0.6 MHz, 0.7 MHz, 0.8 MHz and 0.9 MHz for sample 3.

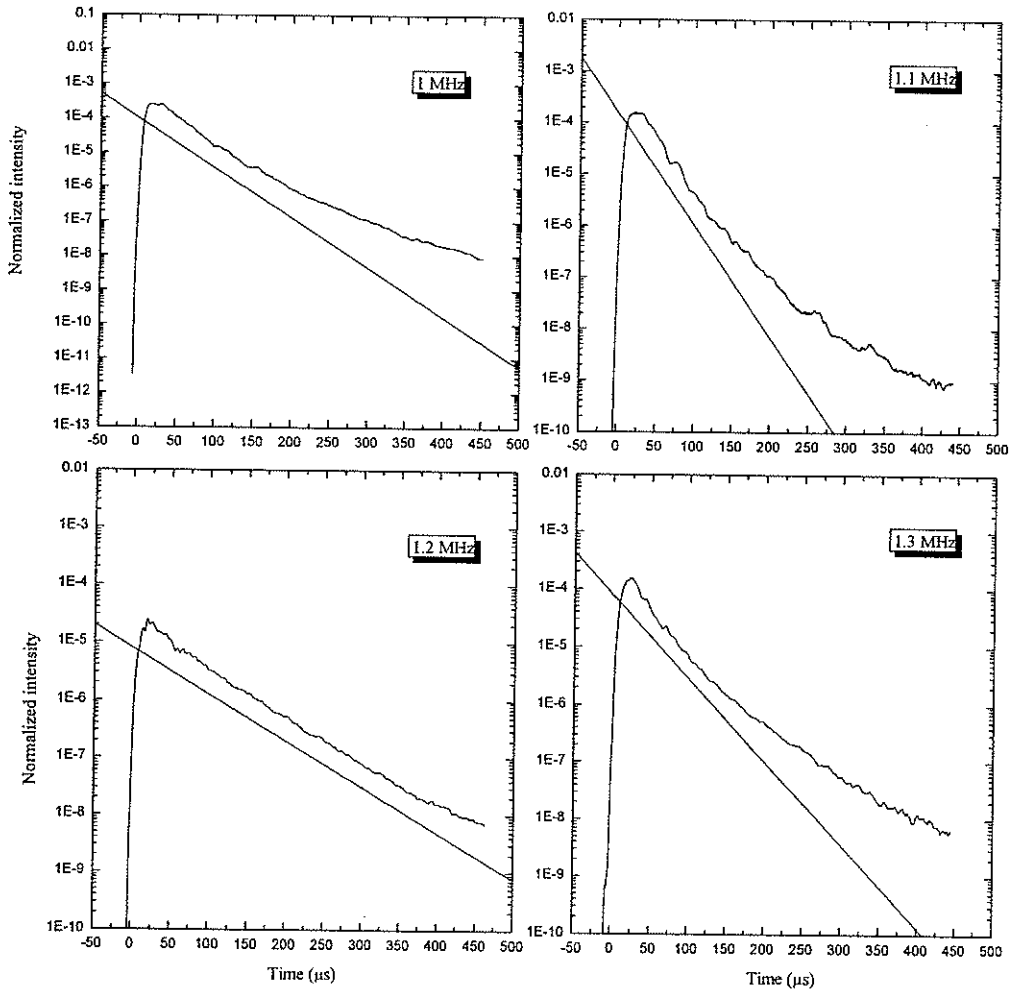

Fig. A.9. Transmitted intensity profile at 1 MHz, 1.1 MHz, 1.2 MHz and 1.3 MHz for sample 3.

A.2.2 Sample 4

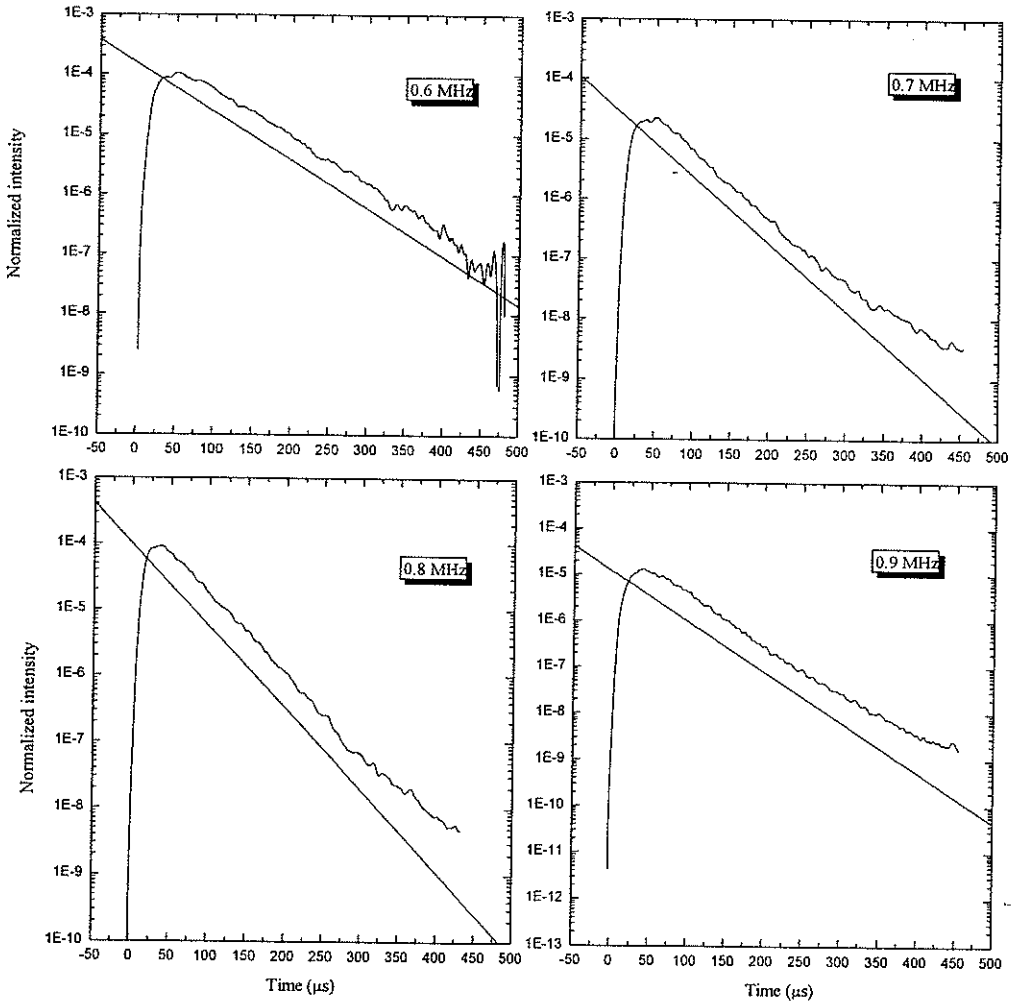

Fig. A.10. Transmitted intensity profile at 0.6 MHz, 0.7 MHz, 0.8 MHz and 0.9 MHz for sample 4.

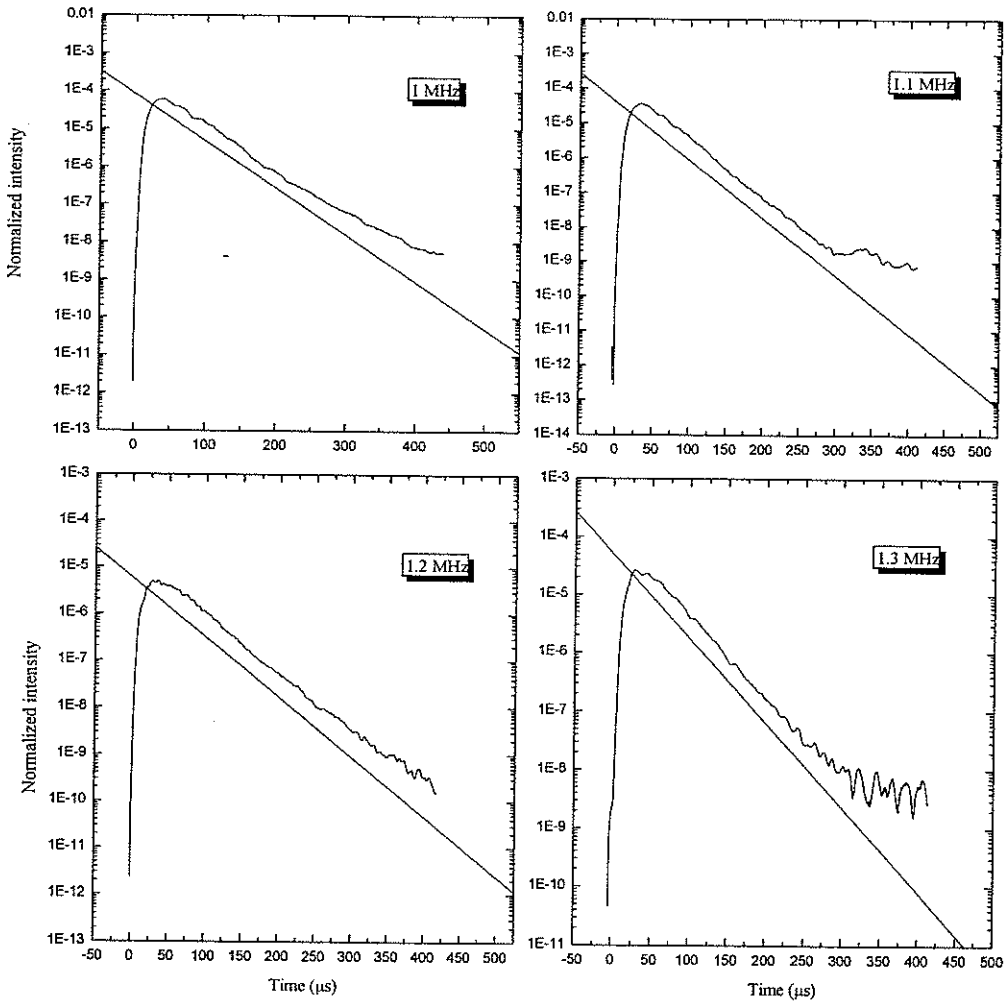

Fig. A.11. Transmitted intensity profile at 1 MHz, 1.1 MHz, 1.2 MHz and 1.3 MHz for sample 4.

A.3 Transmitted intensity profiles in the 2 MHz frequency range

A.3.1 Sample 3

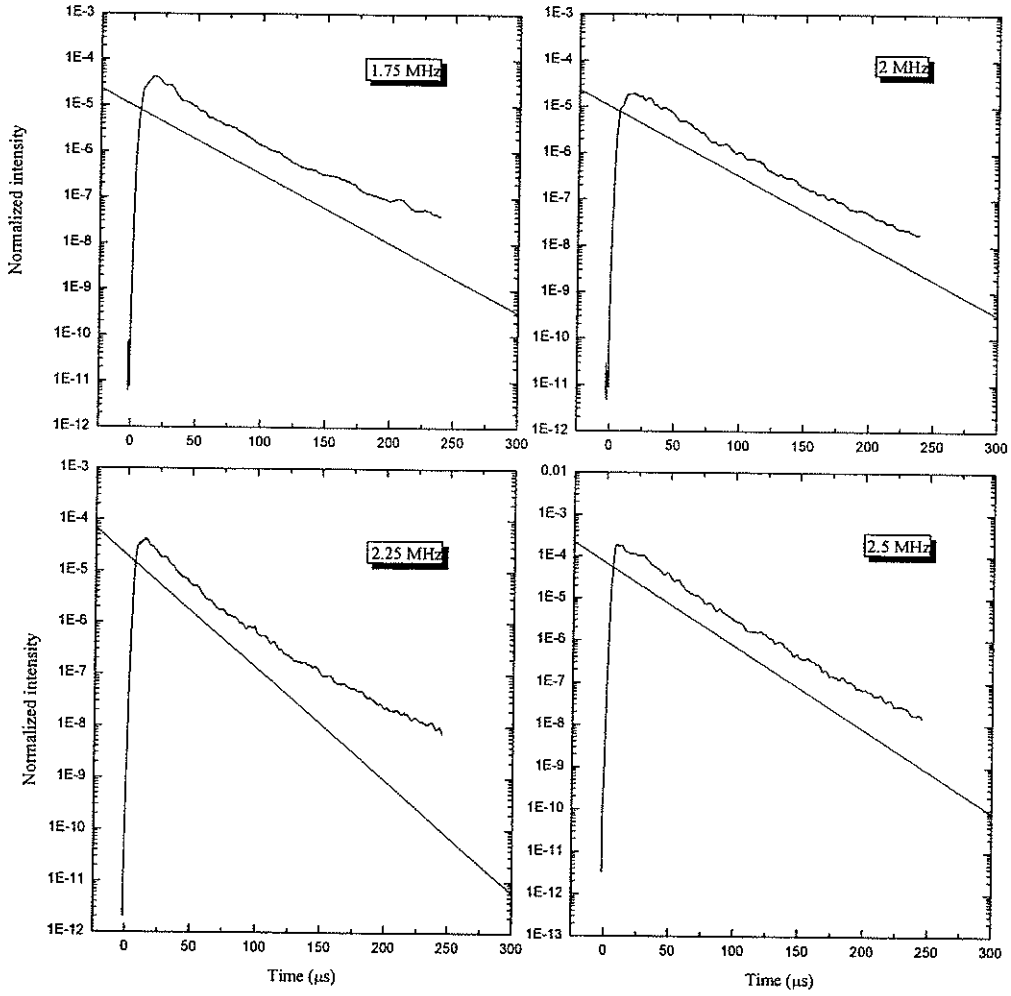

Fig. A.12. Transmitted intensity profile at 1.75 MHz, 2 MHz, 2.25 MHz and 2.5 MHz for sample 3.

A.3.2 Sample 4

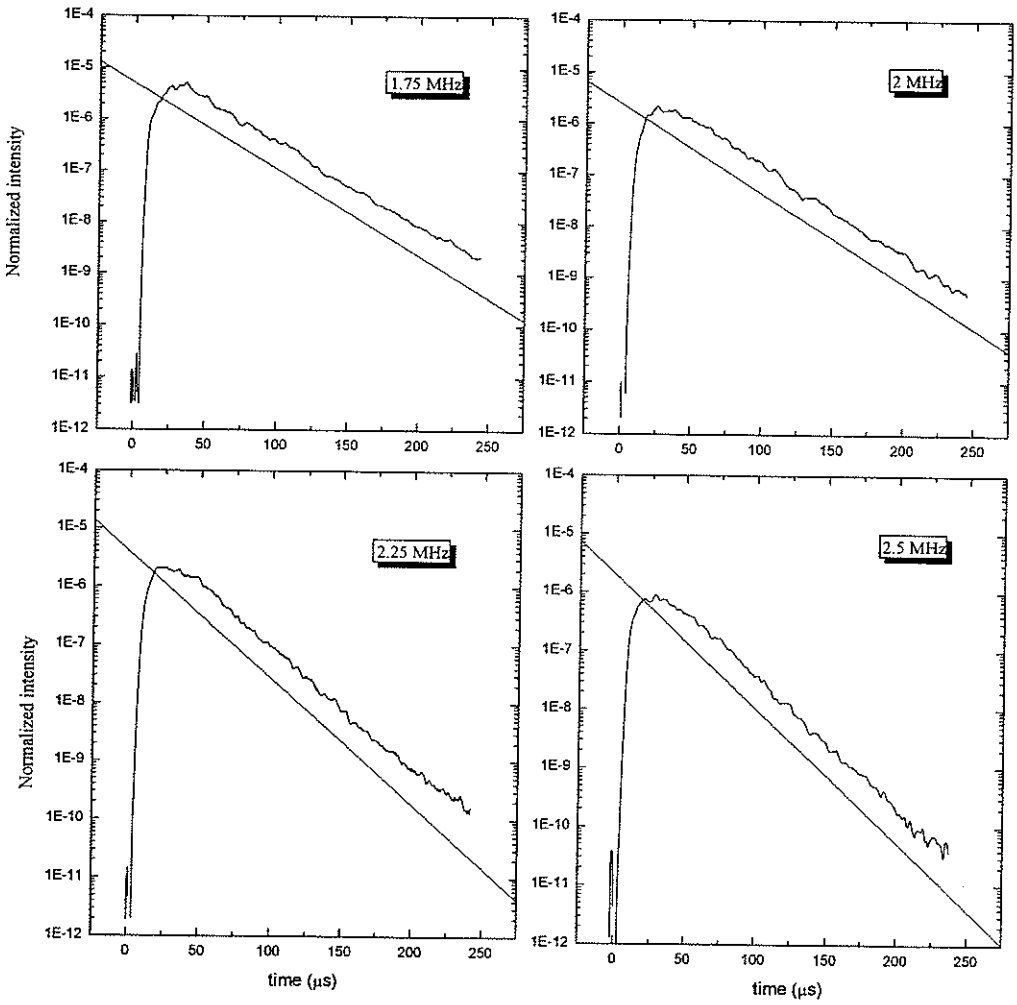

Fig. A.13. Transmitted intensity profile at 1.75 MHz, 2 MHz, 2.25 MHz and 2.5 MHz for sample 4.

A.3.3 Sample 6

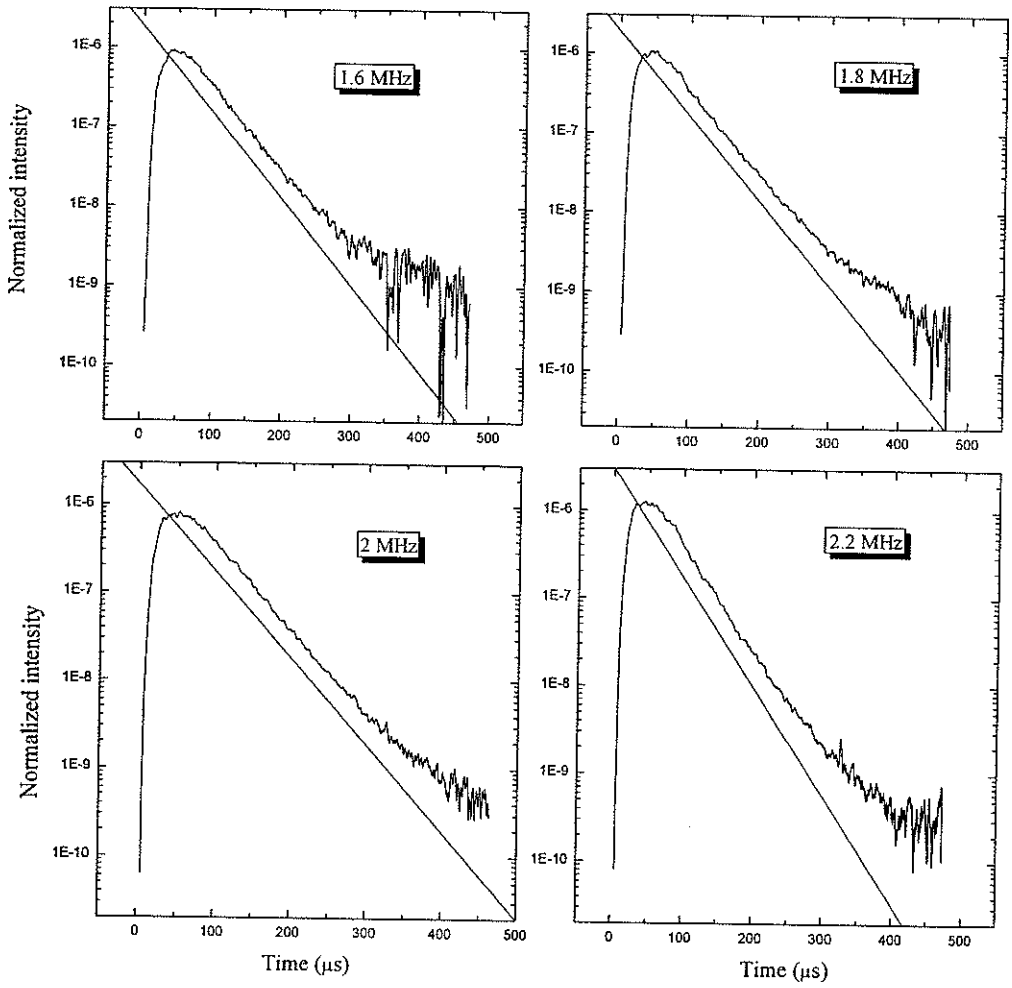

Fig. A.14. Transmitted intensity profile at 1.6 MHz, 1.8 MHz, 2 MHz and 2.2 MHz for sample 6.

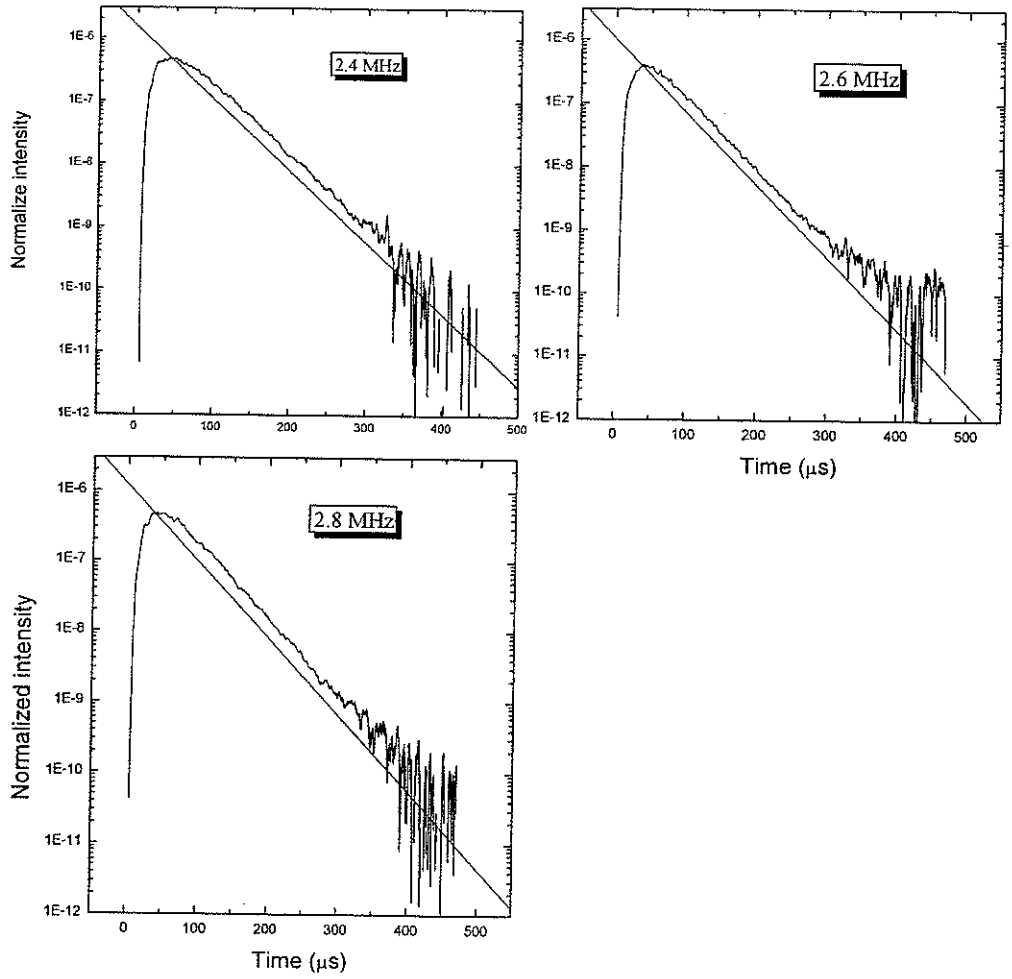

Fig. A.15. Transmitted intensity profile at 2.4 MHz, 2.6 MHz and 2.8 MHz for sample 6.

Appendix B Normalized intensity distributions

B.1 Normalized intensity distributions in the 1 MHz frequency range

289 speckles were acquired in the 1 MHz frequency range for sample 3. As the frequency increased, the deviations in the intensity distributions from the Rayleigh distribution became more pronounced. Since the statistics were not very good, it was difficult to fit equation (2-15) to the tail of the experimental distributions.

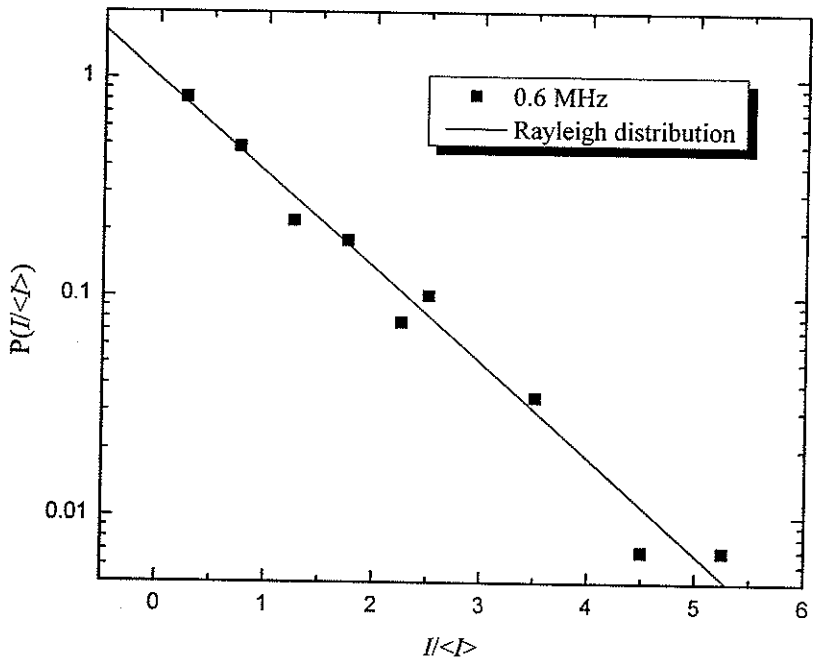

Fig. B.1. Intensity distribution at 0.6 MHz for sample 3.

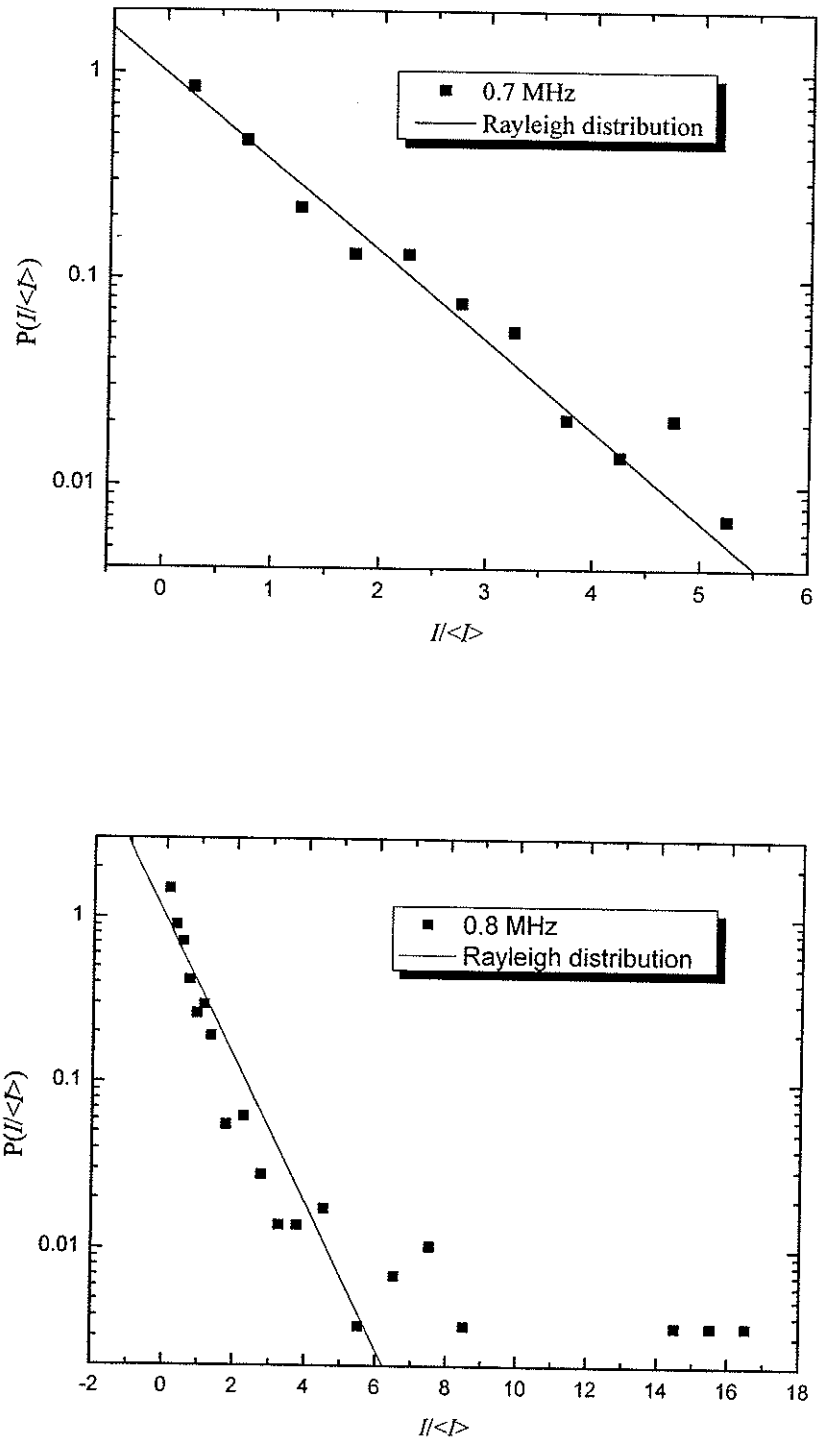

Fig. B.2. Upper figure: intensity distribution at 0.7 MHz for sample 3; Lower figure: intensity distribution at 0.8 MHz for sample 3.

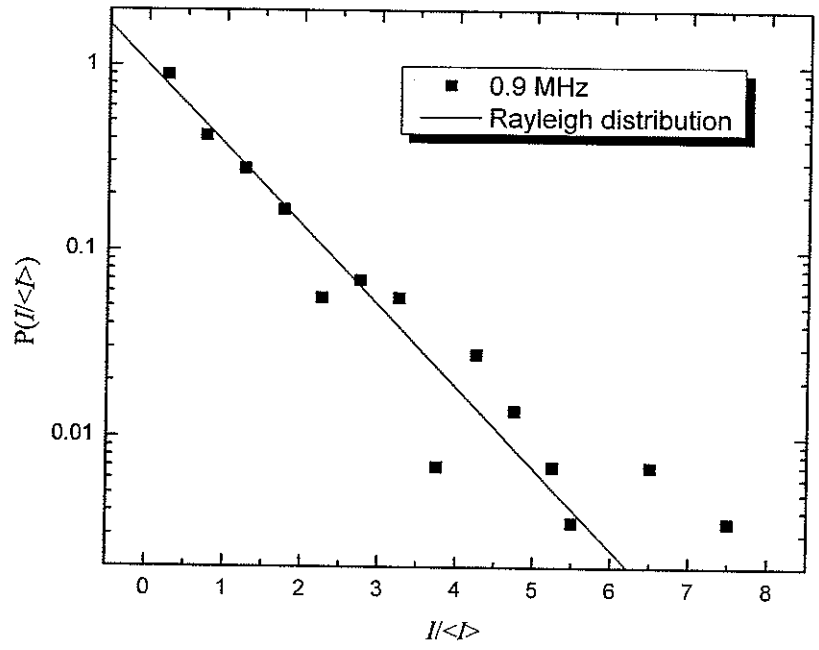

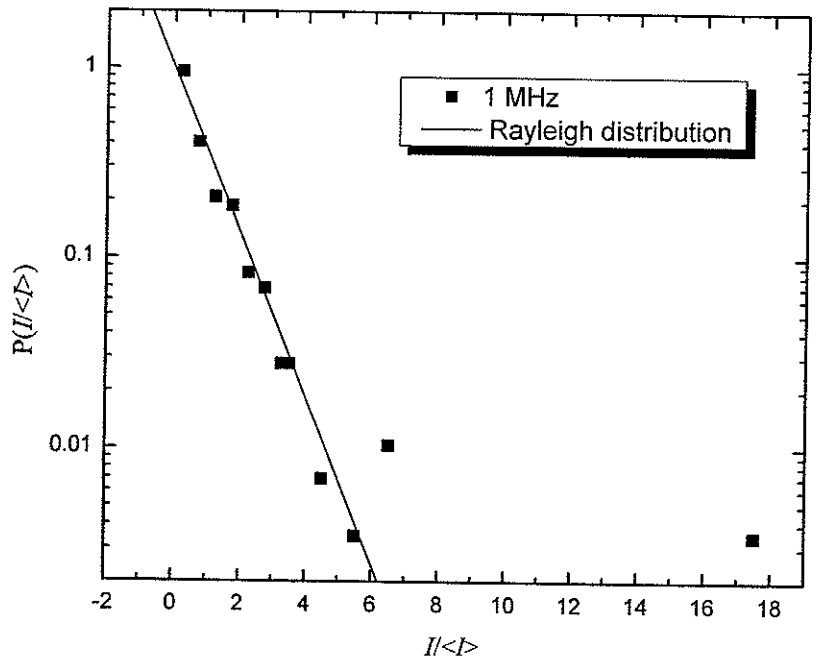

Fig. B.3. Upper figure: intensity distribution at 0.9 MHz for sample 3; Lower figure: intensity distribution at 1 MHz for sample 3.

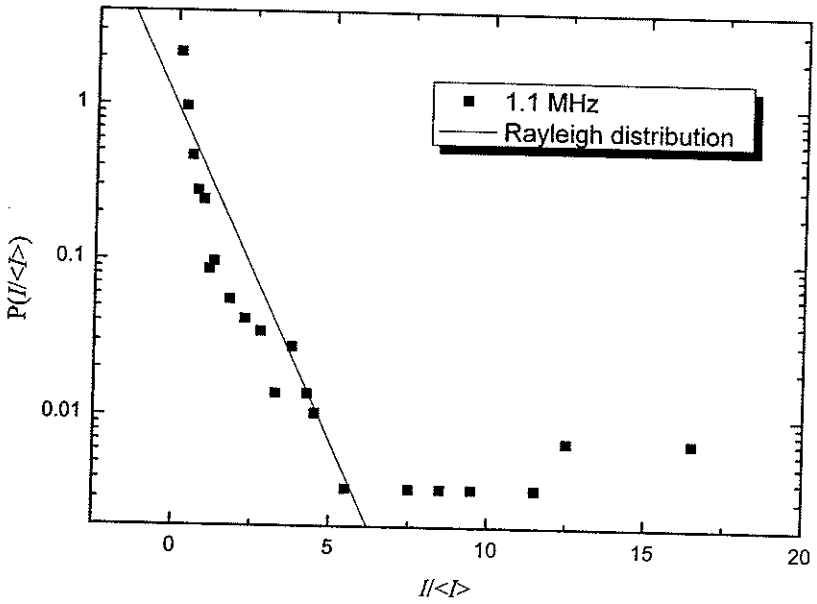

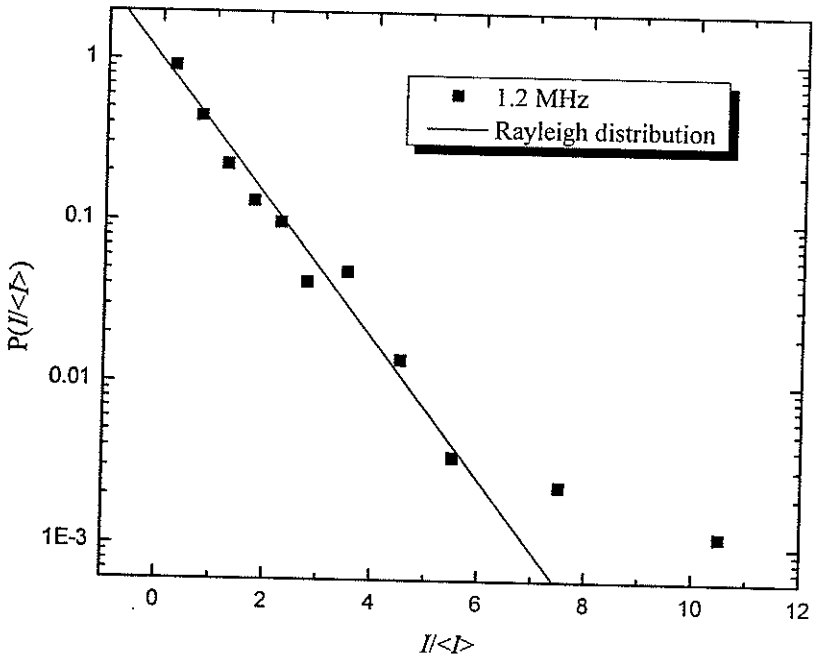

Fig. B.4. Upper figure: intensity distribution at 1.1 MHz for sample 3;
Lower figure: intensity distribution at 1.2 MHz for sample 3.

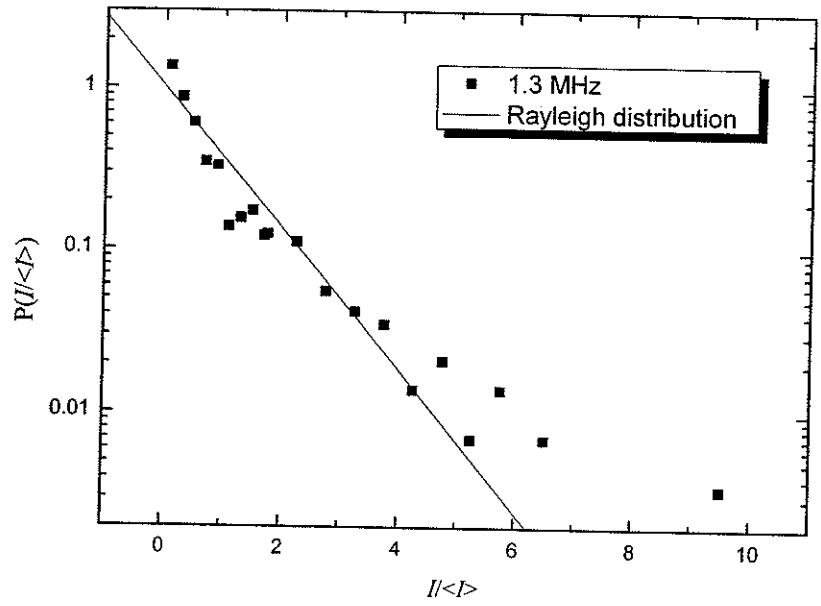

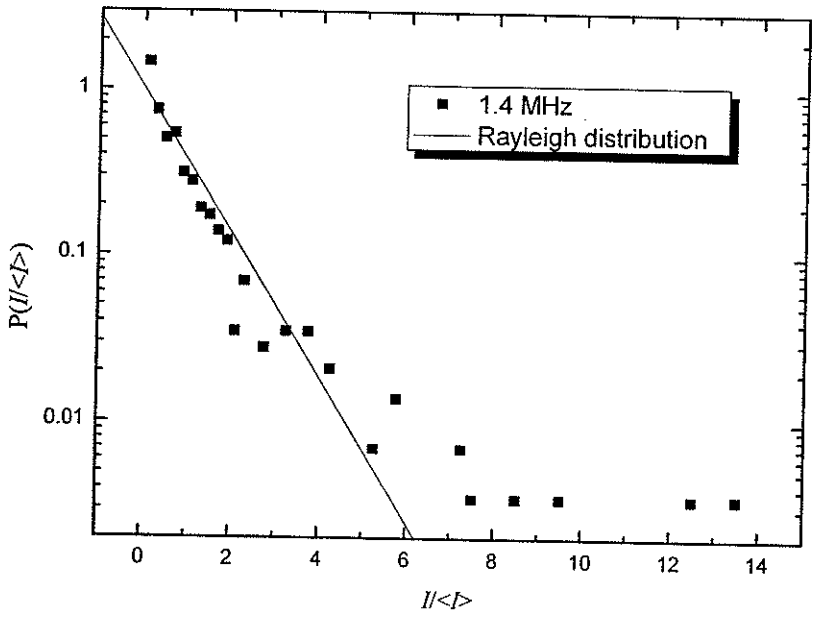

Fig. B.5. Upper figure: intensity distribution at 1.3 MHz for sample 3;
Lower figure: intensity distribution at 1.4 MHz for sample 3.

B.2 Normalized intensity distributions in the 2 MHz frequency range

B.2.1 Sample 3

3025 speckles were acquired in the 2 MHz frequency range for sample 3. The intensity distributions all looked non-Rayleigh-like. However, the statistics for $I/\langle I\rangle > 10$ were not good enough to reliably fit equation (2-15) to the tail. Average of $I/\langle I\rangle$ for some frequencies for different samples will improve the statistics. (section 5.3.3.1)

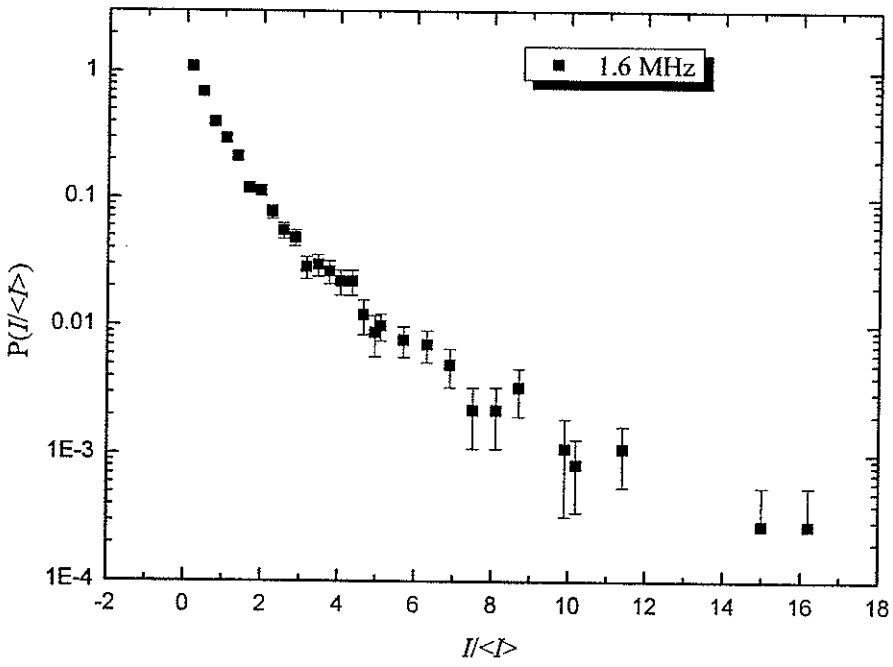

Fig. B.6. Intensity distribution at 1.6 MHz for sample 3.

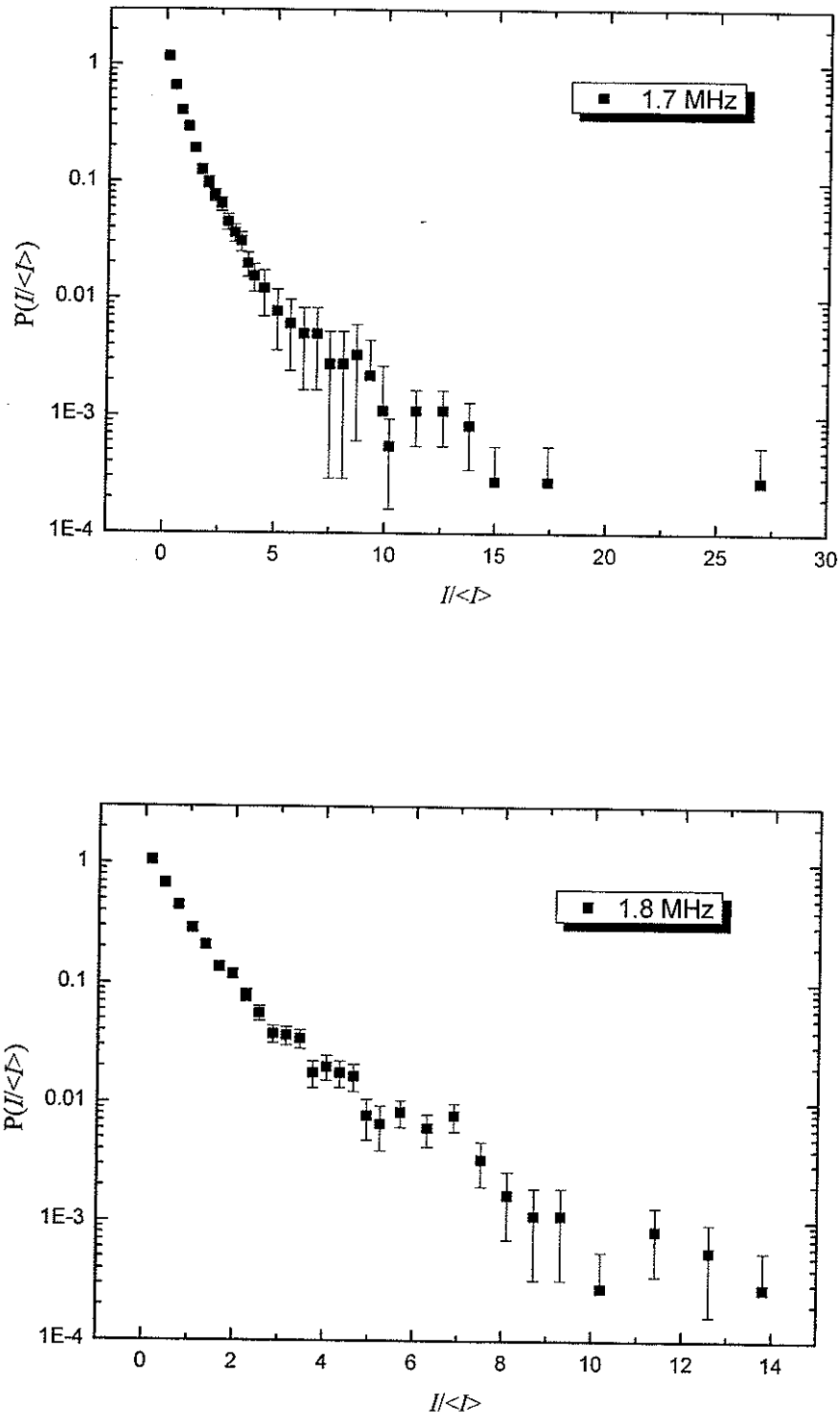

Fig. B.7. Upper figure: intensity distribution at 1.7 MHz for sample 3;
Lower figure: intensity distribution at 1.8 MHz for sample 3.

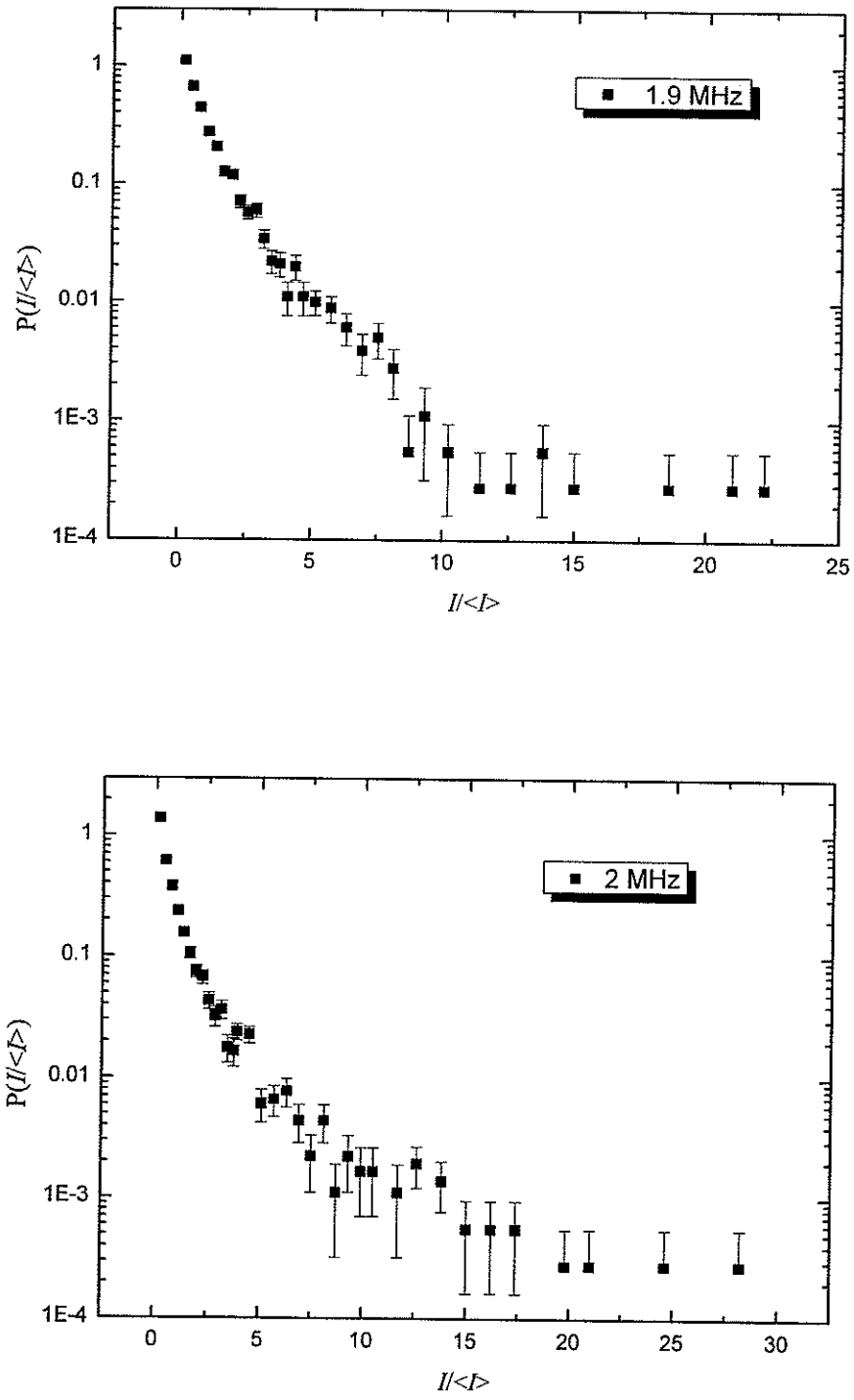

Fig. B.8. Upper figure: intensity distribution at 1.9 MHz for sample 3; Lower figure: intensity distribution at 2 MHz for sample 3.

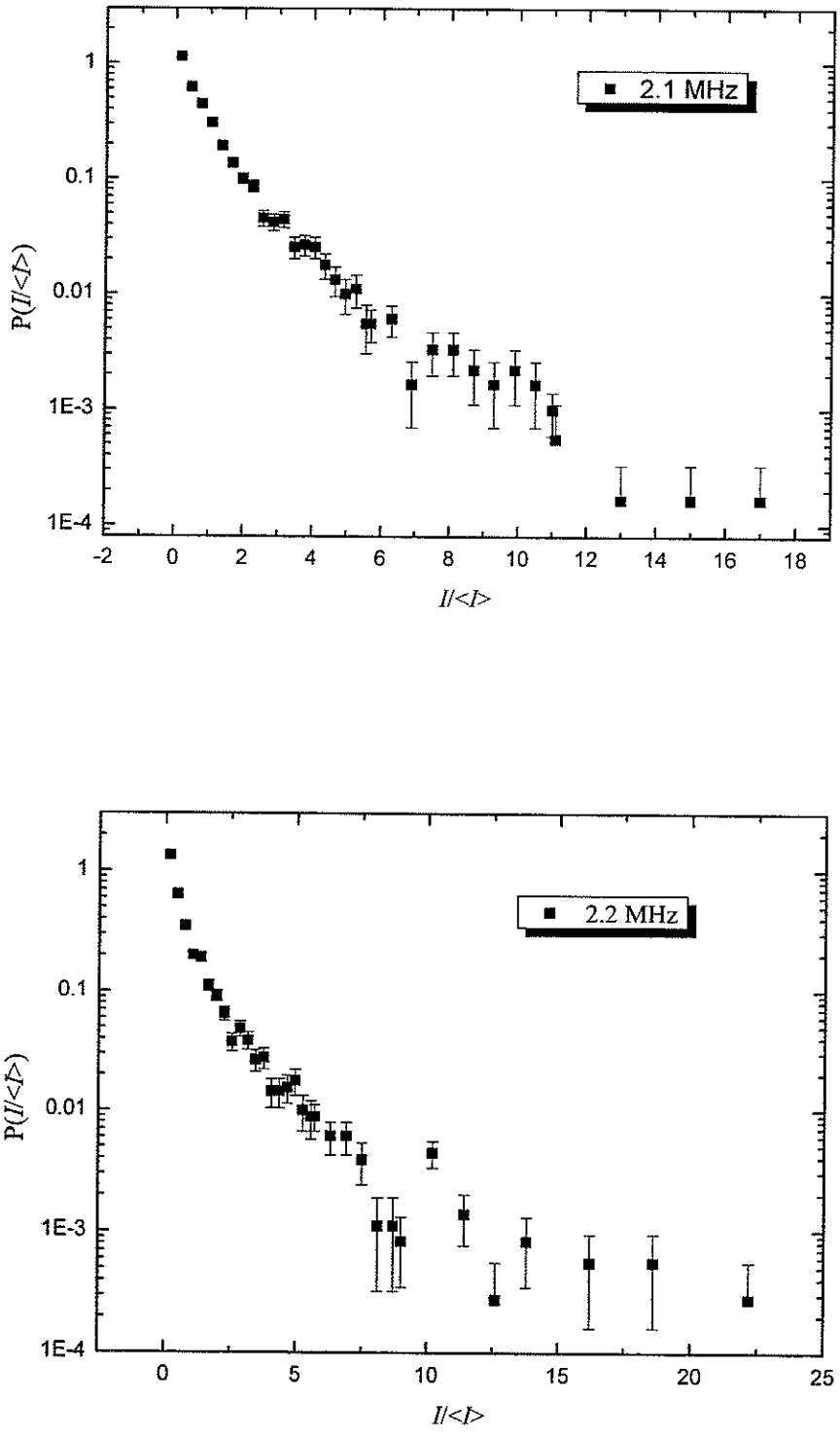

Fig. B.9. Upper figure: intensity distribution at 2.1 MHz for sample 3;
Lower figure: intensity distribution at 2.2 MHz for sample 3.

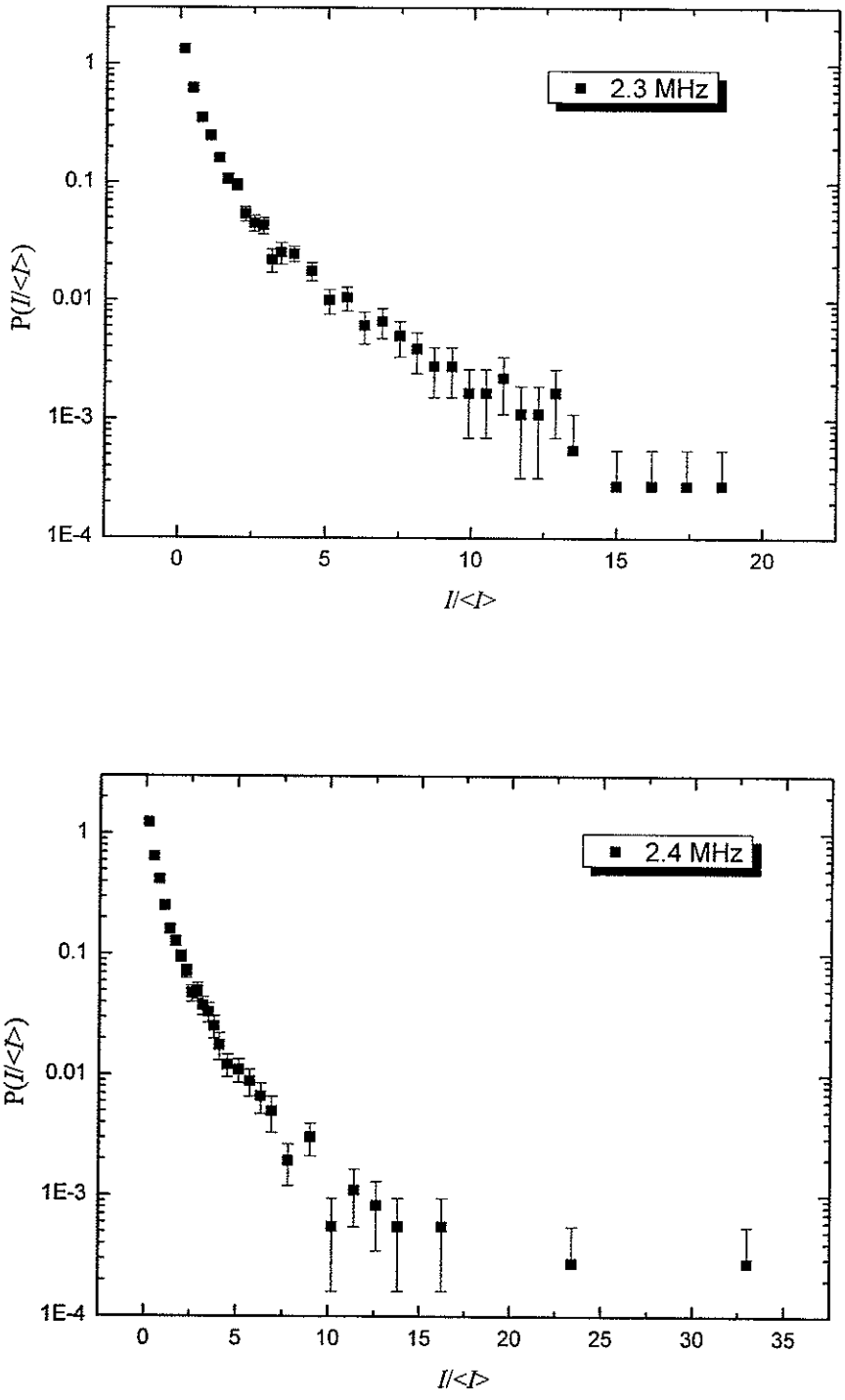

Fig. B.10. Upper figure: intensity distribution at 2.3 MHz for sample 3;
Lower figure: intensity distribution at 2.4 MHz for sample 3.

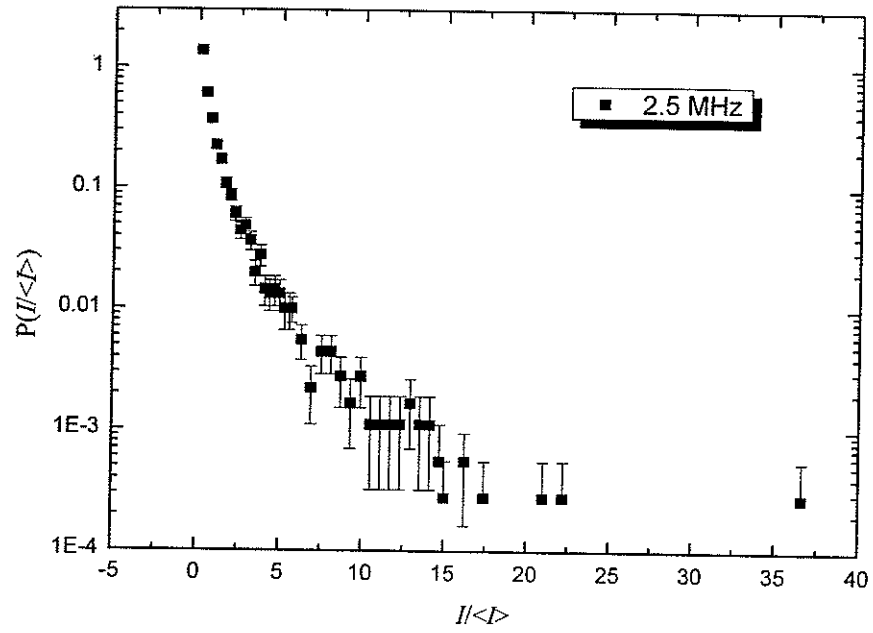

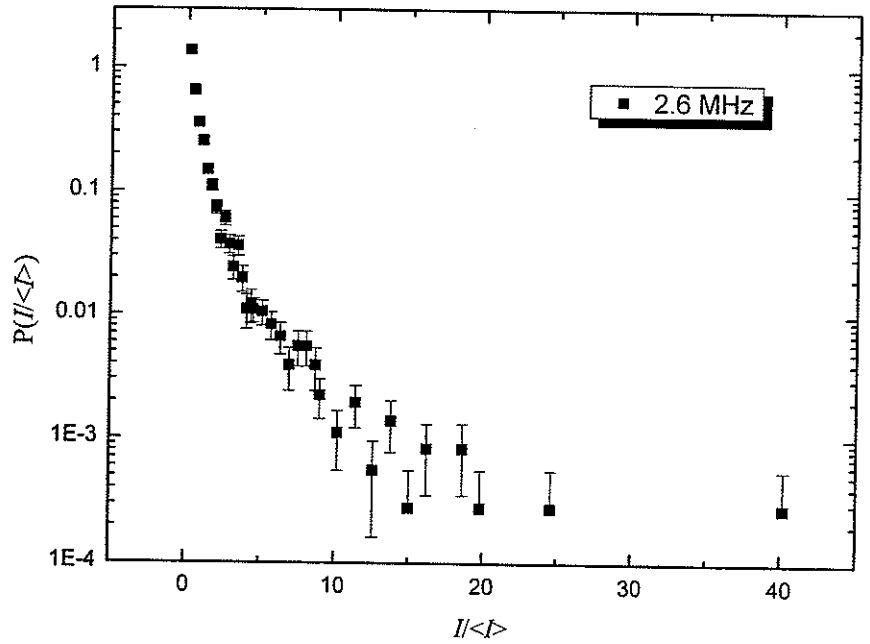

Fig. B.11. Upper figure: intensity distribution at 2.5 MHz for sample 3;
Lower figure: intensity distribution at 2.6 MHz for sample 3.

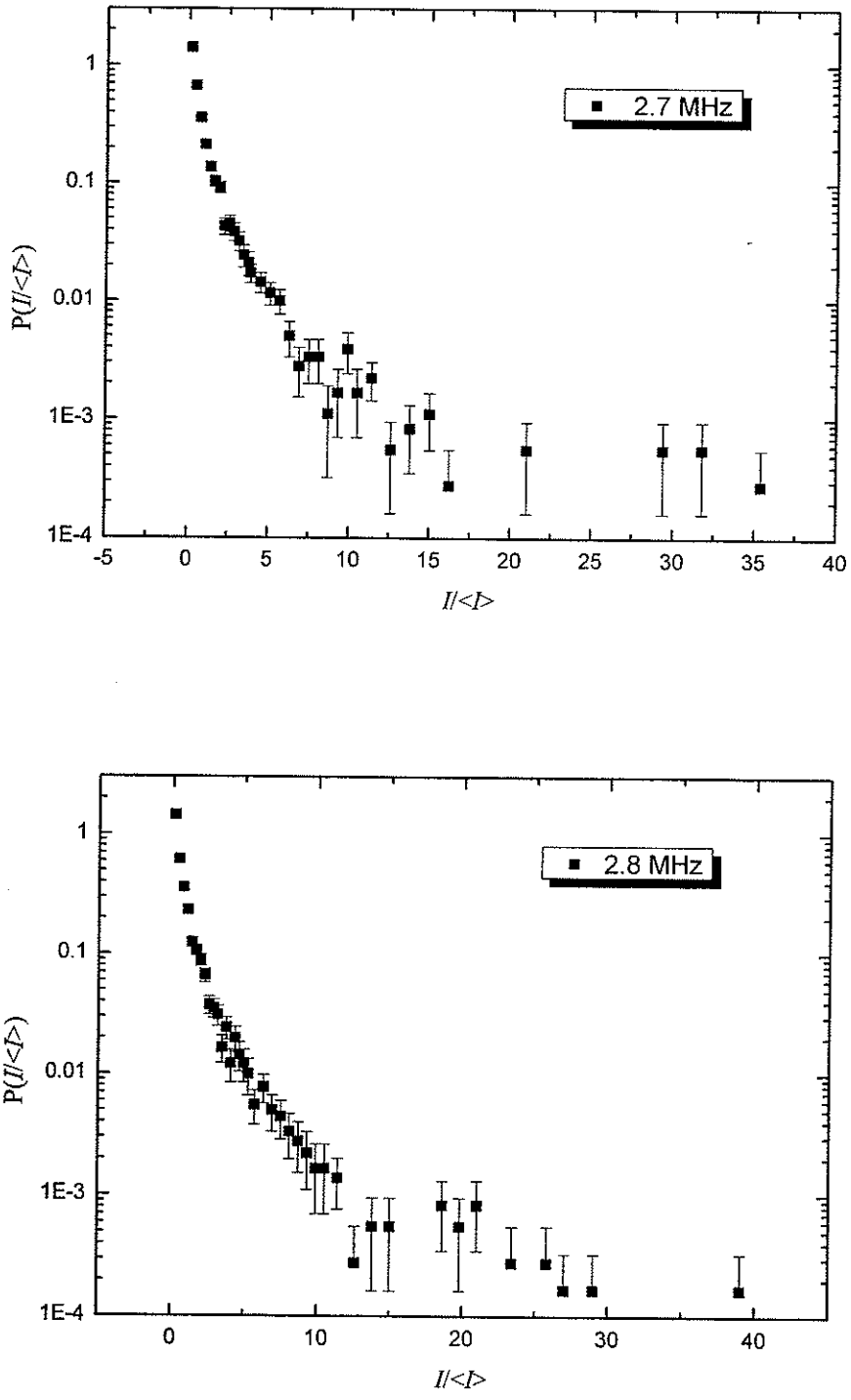

Fig. B.12. Upper figure: intensity distribution at 2.7 MHz for sample 3; Lower figure: intensity distribution at 2.8 MHz for sample 3.

B.2.2 Samples 5, 6 and 7

The intensity distributions for samples 5, 6 and 7 in the 2 MHz frequency range are presented below

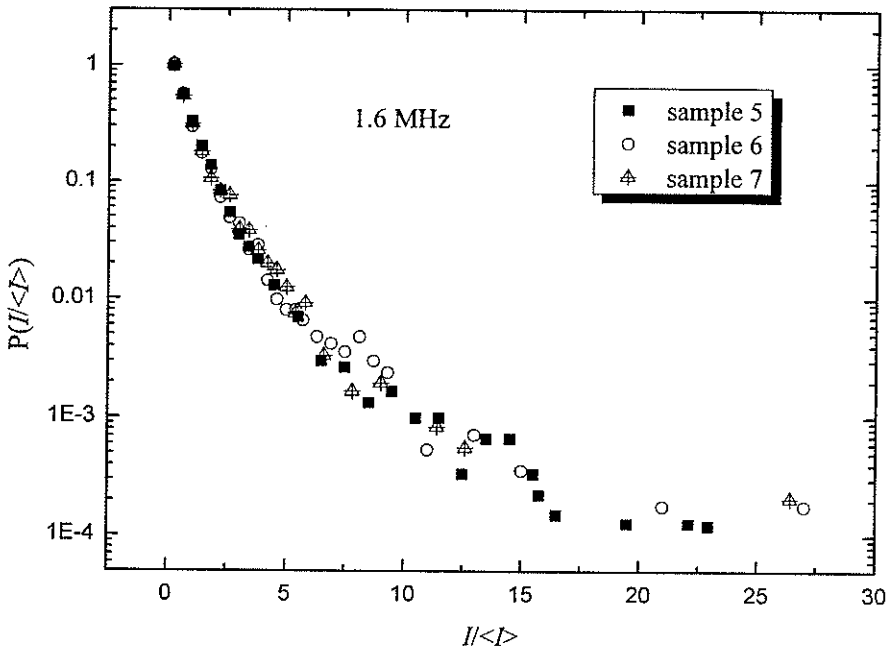

Fig. B.13. Intensity distribution at 1.6 MHz for samples 5, 6 and 7.

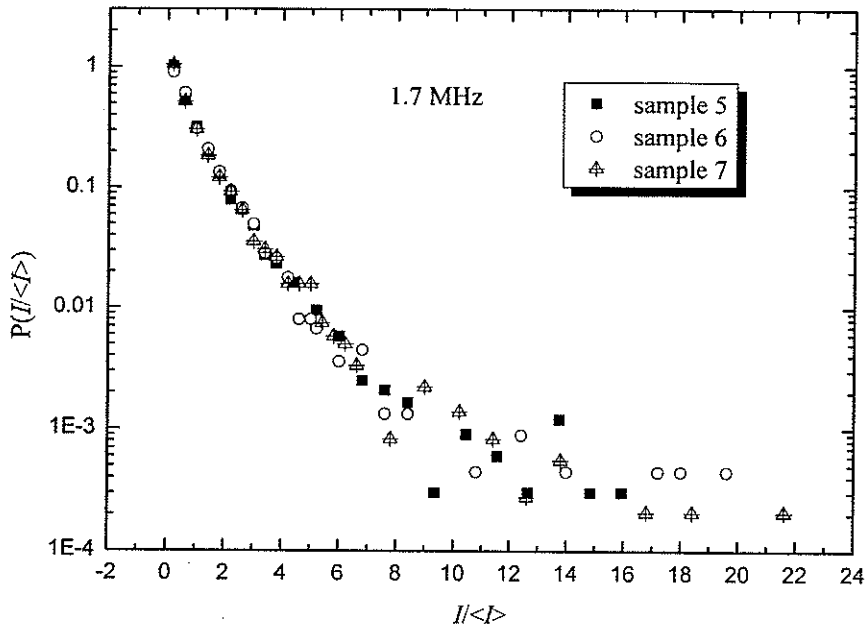

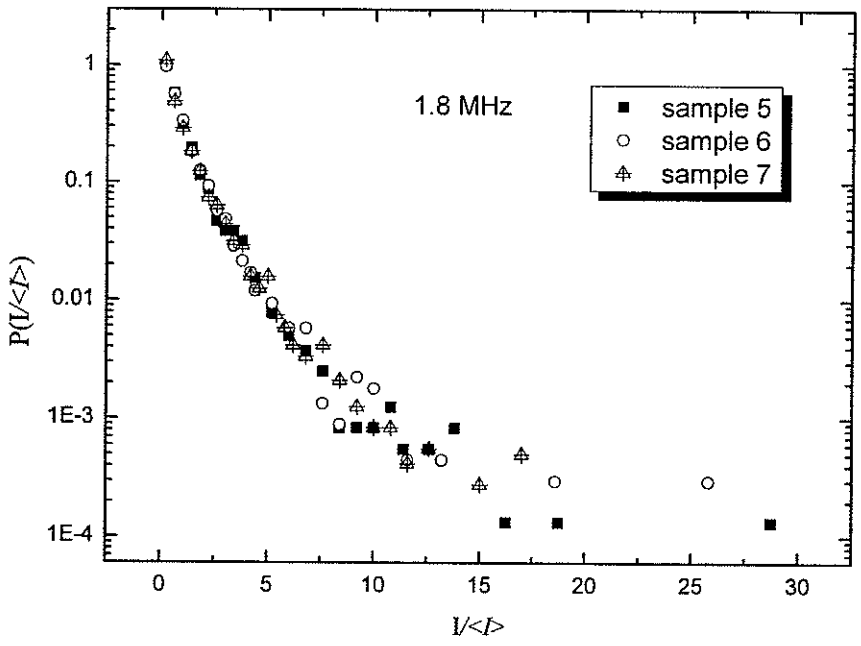

Fig. B.14. Upper figure: intensity distribution at 1.7 MHz for samples 5, 6 and 7; Lower figure: intensity distribution at 1.8 MHz for samples 5, 6 and 7.

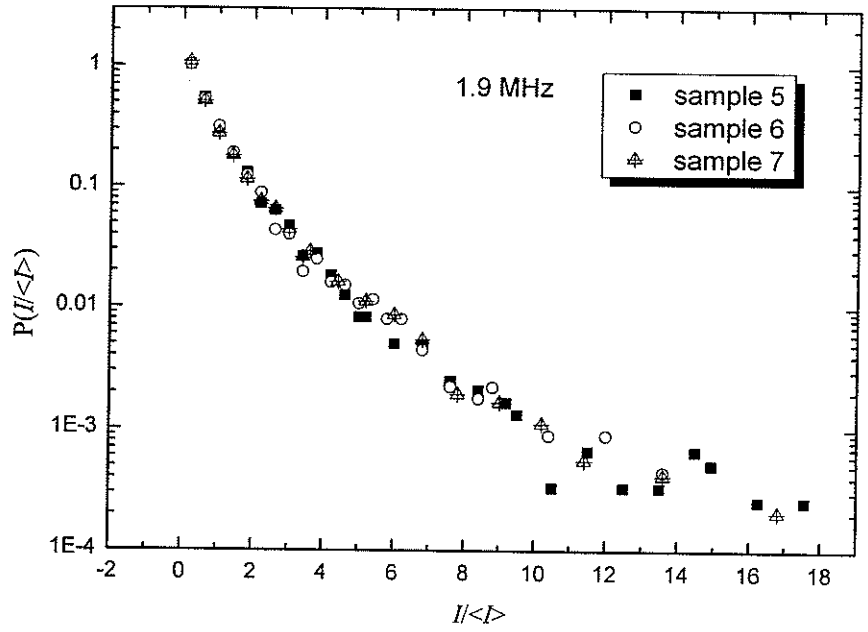

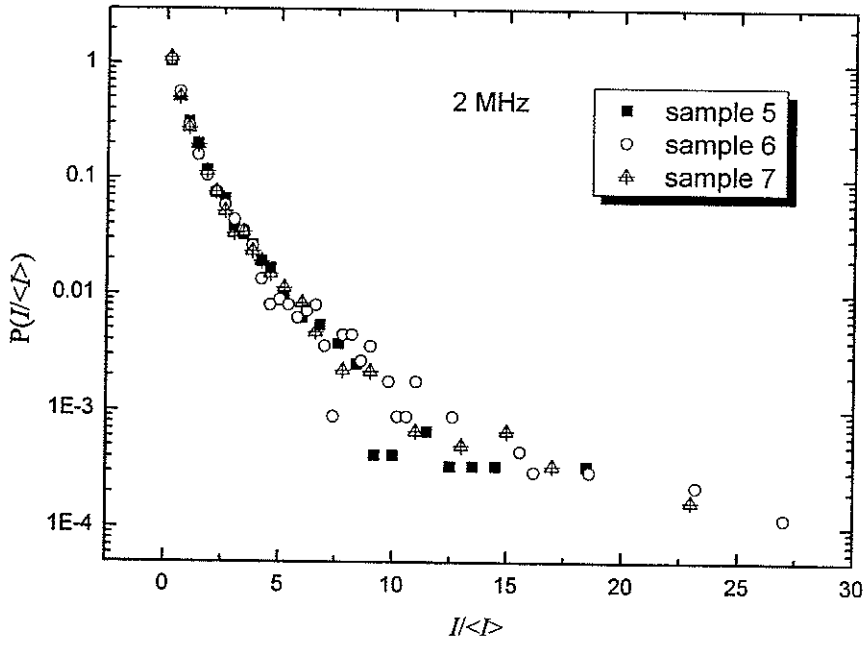

Fig. B.15. Upper figure: intensity distribution at 1.9 MHz for samples 5, 6 and 7; Lower figure: intensity distribution at 2 MHz for samples 5, 6 and 7.

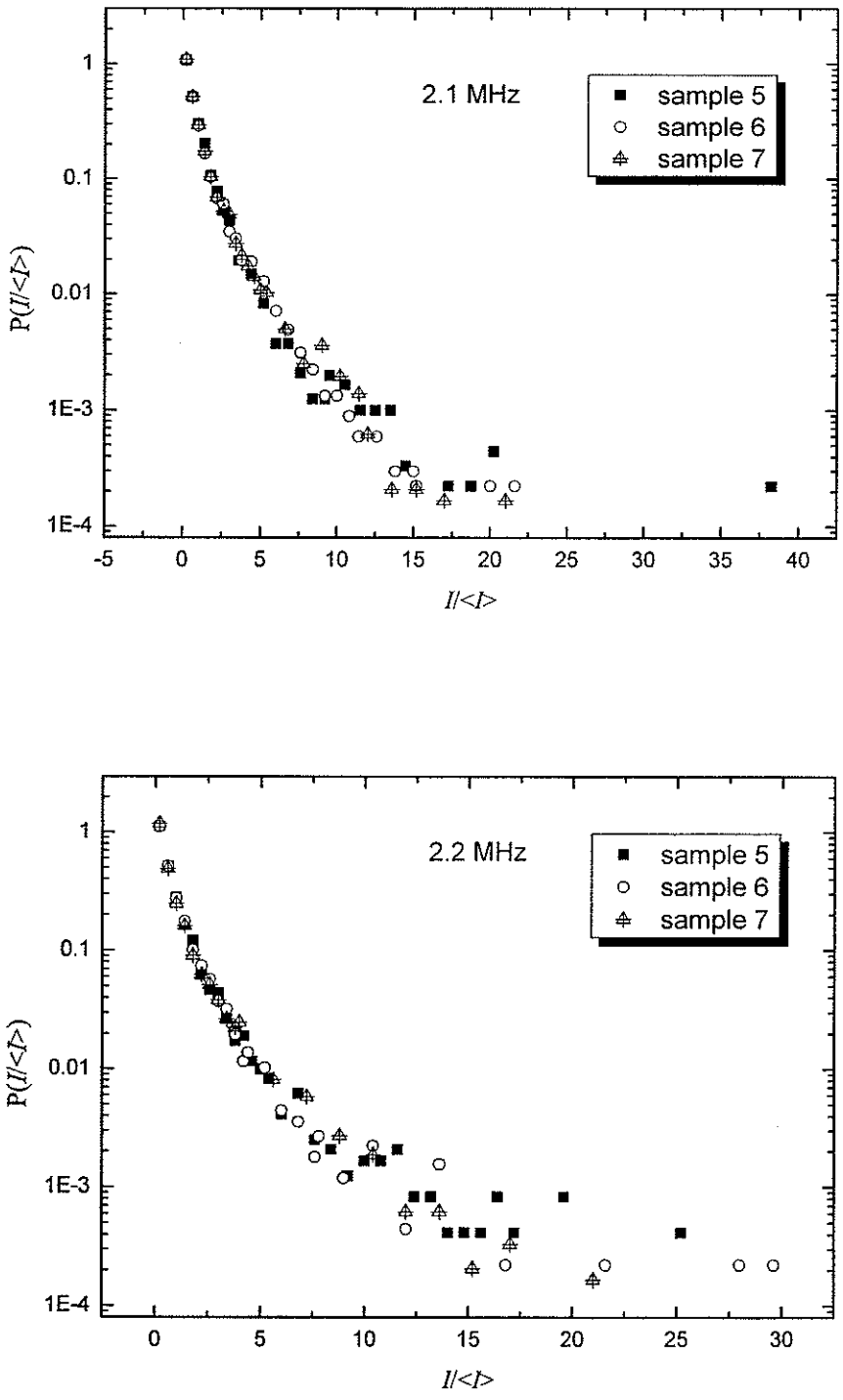

Fig. B.16. Upper figure: intensity distribution at 2.1 MHz for samples 5, 6 and 7; Lower figure: intensity distribution at 2.2 MHz for samples 5, 6 and 7.

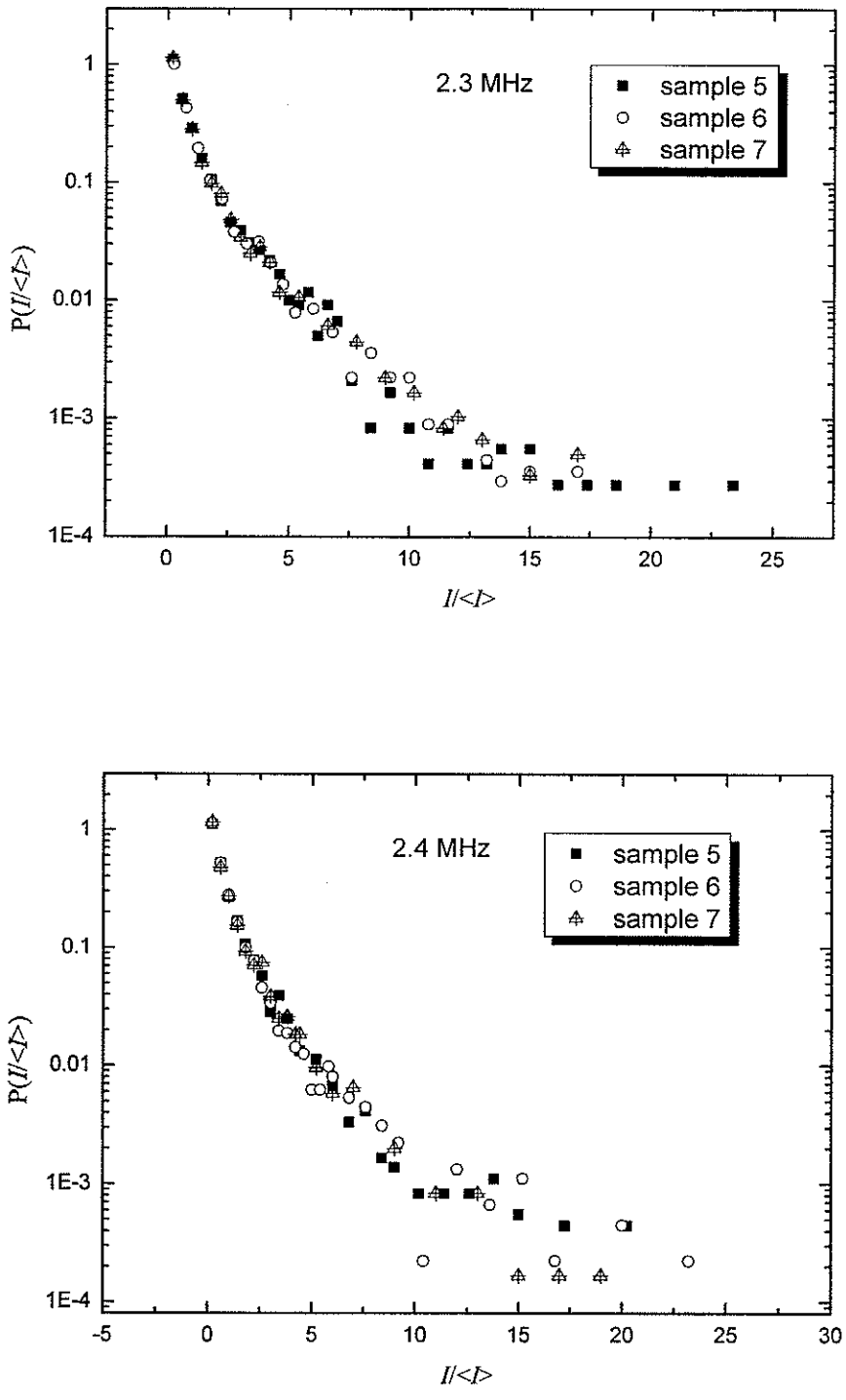

Fig. B.17. Upper figure: intensity distribution at 2.3 MHz for samples 5, 6 and 7; Lower figure: intensity distribution at 2.4 MHz for samples 5, 6 and 7.

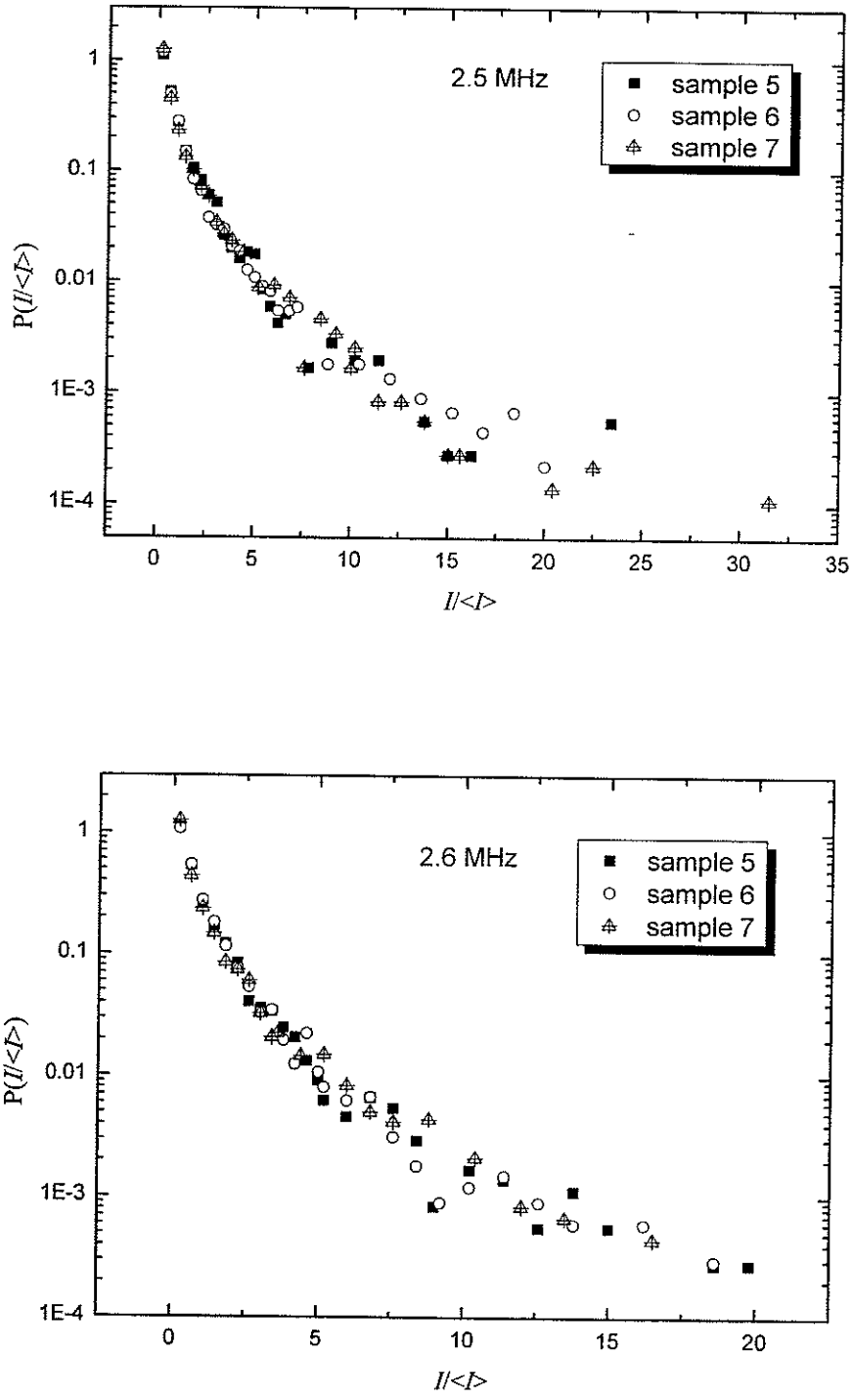

Fig. B.18. Upper figure: intensity distribution at 2.5 MHz for samples 5, 6 and 7; Lower figure: intensity distribution at 2.6 MHz for samples 5, 6 and 7.

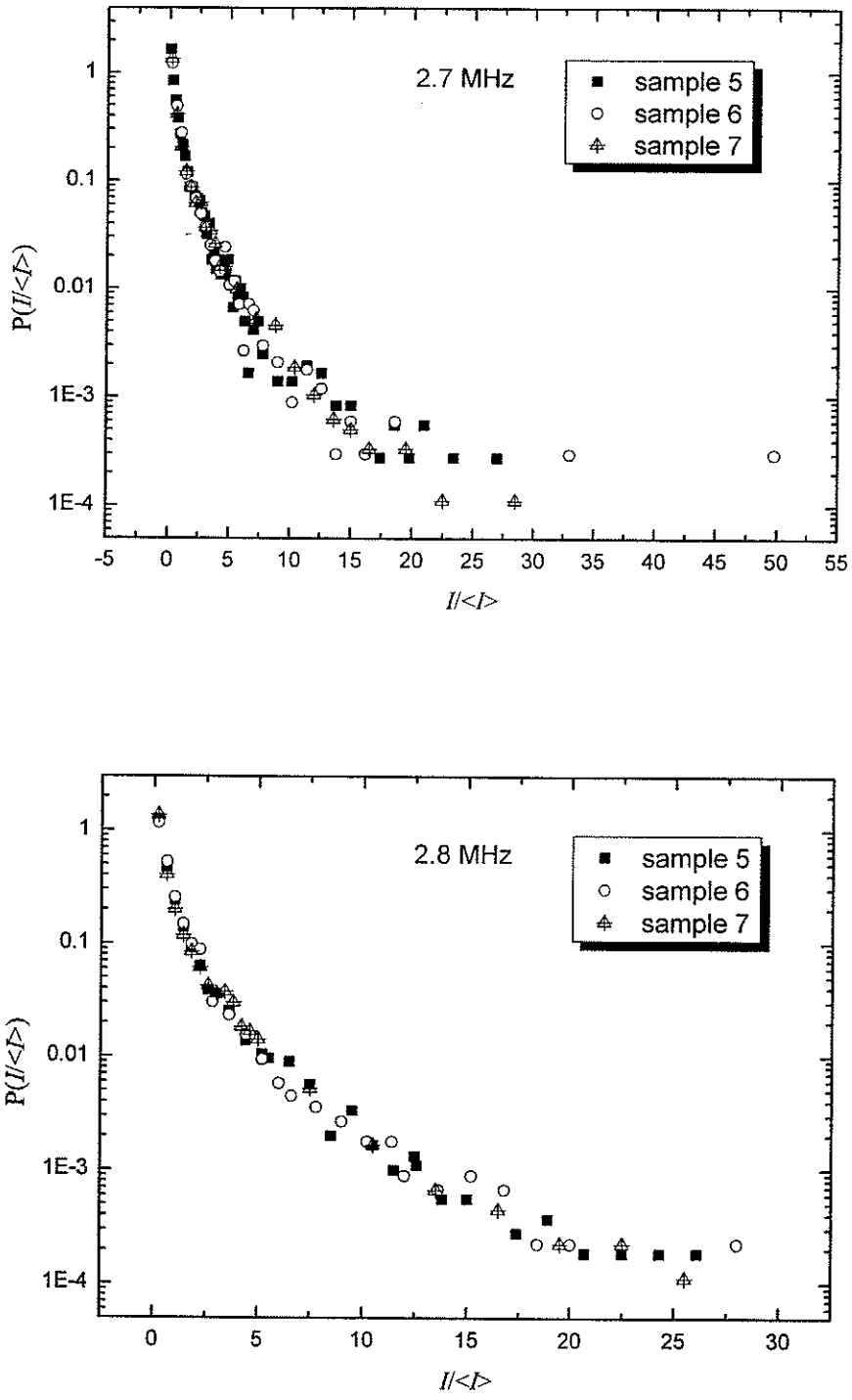

Fig. B.19. Upper figure: intensity distribution at 2.7 MHz for samples 5, 6 and 7; Lower figure: intensity distribution at 2.8 MHz for samples 5, 6 and 7.

References

E. Abrahams, P.W. Anderson, D.C. Licciardello, T.V. Ramakrisnan, "Scaling theory of localization: absence of quantum diffusion in two dimensions", *Phys. Rev. Lett.* **42**, 673-676 (1979).

P.W. Anderson, "Absence of diffusion in certain random lattices", Phys. Rev. **109**, 1492-1505 (1958).

A. Baldantoni, B.J. Janeway, D.C. Lauzon, M.J. Purdon and R.S. Timsit, "NOCOLOK™ Sil Flux – A Novel Approach for Brazing Aluminum", preprint, Alcan Research and Development Co., Kingston, Ont. (2000).

Jake Bobowski, "Summer Student Report for 2000 & 2001", Ultrasonics Research Laborotory Report, University of Manitoba (2001).

H. S. Carslaw and J. C. Jaeger, *Conduction of Heat in Solids*, 2nd ed., Oxford University Press, London (1959).

A.A. Chabanov, M. Stoytchev, and A.Z. Genack, "Statistical signatures of photon localization", *Nature* **404** 850-853 (2000).

A.A. Chabanov, Z.Q. Zhang, and A.Z. Genack, "Breakdown of Diffusion in Dynamics of Extended Waves in Mesoscopic Media", *Phys. Rev. Lett.* **90**, 203903 (2003).

M.L. Cowan, K. Beaty, J.H. Page, Zhengyou Liu and Ping Sheng, "Group velocity of acoustic waves in strongly scattering media: Dependence on the volume fraction of scatterers", *Phys. Rev. E*, **58**, 6626-35 (1998).

S.K. Cheung, X. Zhang, Z.Q. Zhang, A.A. Chabanov, and A.Z. Genack, "Impact of Weak Localization in the Time Domain", *Phys. Rev. Lett.* **92**, 173902 (2004).

J. Crank, *The Mathematics of Diffusion*, 2nd edition (Clarendon Press, Oxford, 1975), pp. 104-5.

J.W. Goodman, *Statistical Optics*, Wiley, New York (1985).

W. Götze, "A theory for the conductivity of a Fermion gas moving in a strong 3D random potential", *J. Phys. C* **12**, 1279 (1979)

A. F. Ioffe and A. R. Regel, "Non-crystalline, amorphous and liquid electronic semiconductors", *Prog. Semicond.* **4**, 237-291 (1960)

S. John, "Electromagnetic absorption in a disordered medium near a photon mobility edge", *Phys. Rev. Lett.* **53**, 2169-2172 (1984)

S. John, "Strong localization of photons in certain disordered dielectric superlattices", *Phys. Rev. Lett.* **58**, 2486 (1987).

E. Kogan and M. Kalveh, "Random-matrix-theory approach to the intensity distributions of waves propagating in a random medium", *Phys. Rev. B* **52**, R3813-5 (1995).

Zhengyou Liu, C.T. Chan, Ping Sheng, A.L. Goertzen and J.H. Page, "Elastic wave scattering by periodic structures of spherical objects: Theory and experiment", *Phys. Rev. B.* **62**, 2446-57 (2000)

P. Markoš and C. M. Soukoulis, "Intensity distribution of scalar waves propagating in random media", *Phys. Rev. B* **71**, 054201 (2005)

J.N. Munday and W.M. Robertson, "Negative group velocity pulse tunneling through a coaxial photonic crystal", *App. Phys. Lett.*, **81**, 2127 (2002).

Th. M. Nieuwenhuizen and M.C.W. van Rossum, "Intensity Distributions of Waves Transmitted through a Multiple Scattering Medium", *Phys. Rev. Lett.* **74**, 2674 (1994).

J.H. Page, H.P. Schriemer, A.E. Bailey and D.A. Weitz, "Experimental Test of the Diffusion Approximation for Multiply Scattered Sound", *Phys. Rev. E*, **52**, 3106-14 (1995).

J.H. Page, Ping Sheng, H.P. Schriemer, I. Jones, Xiaodun Jing and D.A. Weitz, "Group Velocity in Strongly Scattering Media", *Science*, **271**, 634-7 (1996).

J.H. Page, W.K. Hildebrand, J. Beck, R. Holmes, and J. Bobowski, "Phonons in porous media at intermediate frequencies", *Phys. Stat. Sol.* (c), **1**, 2925-2928, (2004)

J.H. Page, Suxia Yang, Zhengyou Liu, M.L. Cowan, C.T. Chan and Ping Sheng, "Tunneling and Dispersion in 3D Phononic Crystals", *Zeitschrift fuer Kristallographie*, **220**, 859-870 (2005).

Panametrics, *Ultrasonic Transducers for Nondestructive Testing*, Panametrics Inc., Waltham, MA (1993).

M.C.W. van Rossum and Th. M. Nieuwenhuizen, "Multiple scattering of classical waves: microscopy, mesoscopy and diffusion", *Rev.Mod. Phys.* **71**, 313-371 (1999).

F. Scheffold, R. Lenke, R. Tweer, and G. Maret, "Localization or classical diffusion of light?", *Nature* **398**, 206 (1999).

H.P. Schriemer, M.L. Cowan, J.H. Page, Ping Sheng, Zhengyou Liu, and D.A. Weitz, "Energy Velocity of Diffusing Waves in Strongly Scattering Media", *Phys. Rev. Lett.*, **79**, 3166-9 (1997).

H.P. Schriemer, N.G. Pachet, and J.H. Page, "Ultrasonic Investigation of the Vibrational Modes of a Sintered Glass-Bead Percolation System", *Waves in Random Media*, **6**, 361-386 (1996).

H.P. Schriemer, *Ballistic and Diffusive Transport of Acoustic Waves in Random Media*, Ph.D thesis, University of Manitoba (1997).

P. Sheng, M. Zhou and Z-Q. Zhang, "Phonon transport in strong-scattering media", *Phys. Rev. Lett.* **72**, 234 (1994).

P. Sheng, *Introduction to Wave Scattering, Localization, and Mesoscopic Phenomena*, Academic Press, San Diego (1995).

S.E. Skipetrov and B.A. van Tiggelen, "Breakdown of Diffusion in Dynamics of Extended Waves in Mesoscopic Media", *Phys. Rev. Lett.* **90**, 203903 (2004).

S.E. Skipetrov and B.A. van Tiggelen, "Dynamics of Anderson Localization in Open 3D Media", *Phys. Rev. Lett.* **96**, 043902 (2006).

M. Stoytchev and A.Z. Genack, "Observations of non-Rayleigh statistics in the approach to photon localization", *Optics Letters* **24**, 262-264 (1999).

M. Störzer, P. Gross, C. M. Aegerter and G. Maret, "Observation of the critical regime near Anderson localization of light", *Phys. Rev. Lett.* **96**, 063904(2006).

A. Sukhovich, J. Page, B. van Tiggelen and Z. Liu, "Resonant Tunneling of Ultrasound in Three-Dimensional Phononic Crystals", *Physics in Canada*, **60(4)**, 245-6 (2004).

A.M. Steinberg, P.G. Kwiat and R.Y. Chiao, "Measurement of the Single-Photon Tunneling Time", *Phys. Rev. Lett.* **71**, 708-711 (1993).

D. J. Thouless, "Electrons in disordered systems and the theory of localization", *Phys. Rep.* **13**, 93 (1974)

B.A. van Tiggelen, "Localization of Waves" in *Diffuse Waves in Complex Media,* ed. by Jean-Pierre Fouque (Kluwer Academic Publishers, Dordrecht, 1999), pp 1-60.

J.A. Turner, M.E. Chambers and R.L. Weaver, "Ultrasonic Band Gaps in Aggregates of Sintered Aluminum Beads", *Acustica* **84**, 628-631 (1998)

François Van Der Biest, Alexei Sukhovich, J.H. Page, Arnaud Tourin, B.A. van Tiggelen, Zhengyou Liu, Mathias Fink, "Resonant tunneling of acoustic waves through a double barrier consisting of two phononic crystals", *Europhys. Lett.* **71**, 63-69 (2005).

D. Vollhardt and P. Wölfle, "Diagrammatic, selfconsistent treatment of the Anderson localization problem in $d \leq 2$ dimensions", *Phys. Rev. B*, **22**, 4666 (1980)

D. Vollhardt and P. Wölfle, "Scaling relations from a selfconsistent theory for Anderson localization", *Phys. Rev. Lett.* **48**, 699 (1982)

D. Vollhardt and P. Wölfle, "Selfconsistent theory of Anderson localization", in: Electronic phase transition (Elsevier Science, Amsterdam, 1992)

D.S. Weirsma, P. Bartolini, A. Lagendijk, and R. Righini, "Localization of light in a disordered medium", *Nature* **390**, 671-673 (1997).

D.S. Weirsma, J.G. Rivas, P. Bartolini, A. Lagendijk, and R. Righini, "Reply: Localization or classical diffusion of light?", *Nature* **398**, 207 (1999).

E. Yablonovitch, "Inhibited Spontaneous Emission in Solid-State Physics and Electronics", *Phys. Rev. Lett.* **58**, 2059 (1987).

Suxia Yang, *Ultrasonic Properties of Phononic Crystals*, Ph.D. thesis, Hong Kong University of Science and Technology (2002).

Suxia Yang, J. H. Page, Zhengyou Liu, M. L. Cowan, C.T. Chan and Ping Sheng, "Ultrasound Tunneling Through 3D Phononic Crystals", *Phys. Rev. Lett.* **88**, 104301 (2002).

J. X. Zhu, D. J. Pine, and D. A. Weitz, "Internal reflection of diffusive light in random media," *Phys. Rev A* **44**, 3948-59 (1991).